Report Title: Optimal Model Complexity in Geological Carbon Sequestration: A Response Surface Uncertainty Analysis

Type of Report: Final research progress report

Reporting Period: 10/1/2012 - 12/31/2016

Author Name: Ye Zhang

Submission Date: 12/29/2016

DOE Award Number: DE-FE-0009238

Recipient Organization:
University of Wyoming
1000 E. University Ave.
Dept 3355
Laramie, WY 82071

Disclaimer

Table of Content 3

Abstract

The critical component of a risk assessment study in evaluating GCS is an analysis of uncertainty in CO_2 modeling. In such analyses, direct numerical simulation of CO_2 flow and leakage requires many time-consuming model runs. Alternatively, analytical methods have been developed which allow fast and efficient estimation of CO_2 storage and leakage, although restrictive assumptions on formation rock and fluid properties are employed. In this study, an intermediate approach is proposed based on the Design of Experiment and Response Surface methodology, which consists of using a limited number of numerical simulations to estimate a prediction outcome as a combination of the most influential uncertain site properties. The methodology can be implemented within a Monte Carlo framework to efficiently assess parameter and prediction uncertainty while honoring the accuracy of numerical simulations. The choice of the uncertain properties is flexible and can include geologic parameters that influence reservoir heterogeneity, engineering parameters that influence gas trapping and migration, and reactive parameters that influence the extent of fluid/rock reactions. The method was tested and verified on modeling long-term CO_2 flow, non-isothermal heat transport, and CO_2 dissolution storage by coupling two-phase flow with explicit miscibility calculation using an accurate equation of state that gives rise to convective mixing of formation brine variably saturated with CO_2. All simulations were performed using three-dimensional high-resolution models including a target deep saline aquifer, overlying caprock, and a shallow aquifer. To evaluate the uncertainty in representing reservoir permeability, sediment hierarchy of a heterogeneous digital stratigraphy was mapped to create multiple irregularly shape stratigraphic models of decreasing geologic resolutions: heterogeneous (reference), lithofacies, depositional environment, and a (homogeneous) geologic formation. To ensure model equivalency, all the stratigraphic models were successfully upscaled from the reference heterogeneous model for bulk flow and transport predictions (Zhang & Zhang, 2015). GCS simulation was then simulated with all models, yielding insights into the level of parameterization complexity that is needed for the accurate simulation of reservoir pore pressure, CO_2 storage, leakage, footprint, and dissolution over both short (i.e., injection) and longer (monitoring) time scales. Important uncertainty parameters that impact these key performance metrics were identified for the stratigraphic models as well as for the heterogeneous model, leading to the development of reduced/simplified models at lower characterization cost that can be used for the reservoir uncertainty analysis. All the CO_2 modeling was conducted using PFLOTRAN – a massively parallel, multiphase, multi-component, and reactive transport simulator developed by a multi-laboratory DOE/SciDAC (Scientific Discovery through Advanced Computing) project (Zhang et al., 2017, in review). Within the uncertainty analysis framework, increasing reservoir depth were investigated to explore its effect on the uncertainty outcomes and the potential for developing gravity-stable injection with increased storage security (Dai et al., 20126; Dai et al., 2017, in review). Finally, to accurately model CO_2 fluid-rock reactions and resulting long-term storage as secondary carbonate minerals, a modified kinetic rate law for general mineral dissolution and precipitation was proposed and verified that is invariant to a scale transformation of the mineral formula weight. This new formulation will lead to more accurate assessment of mineral storage over geologic time scales (Lichtner, 2016).

Project objectives

1. Develop, test, and verify the DoE and RS uncertainty analysis for all the conceptual models, from the high-resolution groundtruth model to increasingly coarsened stratigraphic models;

2. Evaluate an optimal parameterization complexity for predicting a variety of Geological Caron Sequestration (GCS) performance outcomes, e.g., pressure evolution, CO_2 plume footprint, CO_2 storage, brine leakage, distributions of geochemical species, and changes of porosity/*k* in the storage system and their feedback with flow modeling. All performance outcomes will be examined over multiple time scales, including the injection and monitoring phases.

3. Investigate the effect of increasing storage system depth on the uncertainty analysis outcomes; explore the parameterization conditions that can give rise to gravity-stable flow (i.e., CO_2 sink to the bottom of the storage formation), which can lead to enhanced storage efficiency and reduced leakage risk.

Summary of Findings

(1) Developed three-dimensional connectivity-based upscaling methods for porous medium fluid flow and solute transport as required for building alternative, hierarchical conceptual reservoir models for CO_2 storage and leakage simulations. The upscaling methods, their verification, and key findings are described in the following publication:

- Mingkan Zhang, Ye Zhang (2015) Multiscale Dispersivity Upscaling for Three-Dimensional Hierarchical Porous Media, *Water Resources Research*, 51, doi:10.1002/2014WR016202.

(2) For CO_2 fluid-rock reactions and storage, we proposed a modified kinetic rate law for general mineral dissolution and precipitation that is invariant to a scale transformation of the mineral formula weight. In modeling CO_2 sequestration, prior works (e.g., T. Xu, J.A. Apps, and K. Pruess (2003)) used the second form of the oligoclase rate law but did not scale the rate, resulting in a 5 times larger rate constant. This could be the cause for enhanced precipitation of dawsonite observed by the previous investigators but not observed in laboratory and field setting. The modified kinetic rate law will lead to more accurate prediction of CO_2 mineral storage. This research is described in the following publication:

- Lichtner, Peter (2016) Kinetic Rate Laws Invariant to Scaling the Mineral Formula Unit, *American Journal of Science*, vol. 316 no. 5 437-469, doi: 10.2475/05.2016.02.

(3) Conducted a comprehensive uncertainty analysis to evaluate CO_2 storage and CO_2 and brine leakage as modeled by the alternative, hierarchical conceptual reservoir models. Identified conditions at which simpler, low resolution models can provide adequate predictions of CO_2 flow, footprint, pressure profile, dissolution, and CO_2 and brine leakage. This research is described in the following manuscript:

- Mingkan Zhang, Ye Zhang, Peter Litchtner (2017) Uncertainty analysis in modeling CO_2 dissolution in three-dimensional heterogeneous aquifers: effect of multiple conceptual models and explicit fluid flow coupling, *International Journal of Greenhouse Gas Control*, in review.

(4) Conducted a comprehensive uncertainty analysis t to identify the suitable conditions (i.e., water depth, ranges of reservoir intrinsic permeability, and geothermal gradient) under which gravity stable storage can be accomplished for CO_2 storage in GOM offshore sediments. This research is described in the following publication and manuscript:

- Zhenxue Dai, Ye Zhang, Philp Stauffer, Ting Xiao, Mingkan Zhang, William Ampomah, Changbing Yang, Youqin Zhou, Mei Ding, Richard Middleton, Mohamad Soltanian, Jeffery Bielicki (2017) Injectivity evaluation for offshore CO_2 sequestration in marine sediments, *Energy Procedia*, accepted for publication.

- Zhenxue Dai, Ye Zhang, Phil Stauffer, Mingkan Zhang, et al. (2016) Uncertainty analysis of CO2 storage in off-shore Gulf of Mexico, *Natural Communication*, in review.

Appendix

Three journal articles that have been published based on results of this research are attached.

AGU PUBLICATIONS

Water Resources Research

RESEARCH ARTICLE
10.1002/2014WR016202

Multiscale solute transport upscaling for a three-dimensional hierarchical porous medium

Mingkan Zhang[1] and Ye Zhang[1]

[1]Department of Geology and Geophysics, University of Wyoming, Laramie, Wyoming, USA

Key Points:
- Three-dimensional solute transport
- Multiscale solute transport modeling

Correspondence to:
M. Zhang,
mzhang1@uwyo.edu
Y. Zhang,
yzhang9@uwyo.edu

Citation:
Zhang, M., and Y. Zhang (2015), Multiscale solute transport upscaling for a three-dimensional hierarchical porous medium, *Water Resour. Res.*, *51*, 1688–1709, doi:10.1002/2014WR016202.

Received 26 JUL 2014
Accepted 11 FEB 2015
Accepted article online 18 FEB 2015
Published online 23 MAR 2015
Corrected on 7 MAY 2015

This article was corrected on 7 MAY 2015. See the end of the full text for details.

Abstract A laboratory-generated hierarchical, fully heterogeneous aquifer model (FHM) provides a reference for developing and testing an upscaling approach that integrates large-scale connectivity mapping with flow and transport modeling. Based on the FHM, three hydrostratigraphic models (HSMs) that capture lithological (static) connectivity at different resolutions are created, each corresponding to a sedimentary hierarchy. Under increasing system ln$K$ variances (0.1, 1.0, 4.5), flow upscaling is first conducted to calculate equivalent hydraulic conductivity for individual connectivity (or unit) of the HSMs. Given the computed flow fields, an instantaneous, conservative tracer test is simulated by all models. For the HSMs, two upscaling formulations are tested based on the advection-dispersion equation (ADE), implementing space versus time-dependent macrodispersivity. Comparing flow and transport predictions of the HSMs against those of the reference model, HSMs capturing connectivity at increasing resolutions are more accurate, although upscaling errors increase with system variance. Results suggest: (1) by explicitly modeling connectivity, an enhanced degree of freedom in representing dispersion can improve the ADE-based upscaled models by capturing non-Fickian transport of the FHM; (2) when connectivity is sufficiently resolved, the type of data conditioning used to model transport becomes less critical. Data conditioning, however, is influenced by the prediction goal; (3) when aquifer is weakly-to-moderately heterogeneous, the upscaled models adequately capture the transport simulation of the FHM, despite the existence of hierarchical heterogeneity at smaller scales. When aquifer is strongly heterogeneous, the upscaled models become less accurate because lithological connectivity cannot adequately capture preferential flows; (4) three-dimensional transport connectivities of the hierarchical aquifer differ quantitatively from those analyzed for two-dimensional systems.

1. Introduction

As a central topic of subsurface hydrology, solute transport in aquifers has been investigated for several decades. Various theories have been proposed, including the macrodispersion approach based on the advection-dispersion equation (ADE) [e.g., *Gelhar and Axness*, 1983; *Dagan*, 1989] and alternative or nonlocal formulations, e.g., dual and multicontinuum models [*Cushman and Ginn*, 1993; *Neuman*, 1993; *Harvey and Gorelick*, 2000; *Haggerty et al*., 2001], continuous time random walk [*Berkowitz and Scher*, 1998; *Dentz et al*., 2004; *Berkowitz et al*., 2006], moment equation [*Neuman*, 1993, 2003; *Neuman and Tartakovsky*, 2009], projector formalism [*Cushman and Ginn*, 1993; *Cushman et al*., 2002], fractional ADE [*Meerschaert et al*., 1999; *Benson et al*., 2000], and the stochastic-convective approach [*Cvetkovic et al*., 1996; *Cirpka and Kitanidis*, 2000; *Ginn*, 2001]. Simultaneous with theory development, field tracer tests have been conducted at various locations with the explicit goal of testing one or more theories, e.g., Borden, Canada; Mobile, Alabama; Twin Lake, Minnesota; Cape Cod, Massachusetts, Mirror Lake, New Hampshire; and the Macrodispersion Experiment (MADE) at Columbus, Mississippi. At these sites, aquifer hydraulic conductivity (K) ranges from relatively homogeneous, e.g., the Cape Cod site with a σ_f^2 (variance of ln$K$) of 0.24, where K varies by approximately 1 order of magnitude [*Garabedian and Leblanc*, 1991], to highly heterogeneous, e.g., the MADE site has a σ_f^2 ranging from 4.5 [*Rehfeldt et al*., 1992] to 6.0 [*Bohling et al*., 2012], where K varies from 4 to 6 orders of magnitude depending on the measurement methods. As shown by the MADE tracer experiments, when σ_f^2 is high, solute transport exhibits anomalous behavior such as non-Fickian breakthrough curves (i.e., asymmetry and heavy tails) and scale dependence in the observed dispersivity.

In nearly 3 decades, several tracer experiments at the MADE site have been interpreted with theories. Although nonlocal theories can often provide a better match [*Zheng et al*., 2011], ADE was found to capture

the main solute plume characteristics if site heterogeneity is adequately resolved [*Barlebo et al*., 2004; *Salamon et al*., 2007]. When dispersivity was modeled as time-dependent [*Liu et al*., 2008], tritium plume predicted with ADE improves over that of an earlier study simulating the same experiment using a constant dispersivity [*Feehley et al*., 2000]. Assuming low-*K* inclusion within a high-*K* matrix, *Fiori et al*. [2013] capture both the arrival and tailing of the tracer tests with an ADE-based formulation. In these cases, the ability of ADE to capture transport likely improved because of the enhanced degrees of freedom in representing dispersion, as it is well known in regression that models with increased parameterization can provide improved fits to observations. In simulating transport in a synthetic aquifer, ADE was also found to capture bulk transport statistics when dispersivity was modeled as spatially or temporally variable [*Zhang and Gable*, 2008]. Field studies at Lauswiesen, Germany, further suggest that when multiple facies are explicitly accounted for, ADE can provide predictions similar to a mass-transfer model [*Riva et al*., 2008, 2010]. By comparison, nonlocal theories (including the above cited mass-transfer model) often invoke additional transport parameters besides dispersivity, while physical meaning of these parameters and their interpretation using field data can become difficult to reconcile. As an example, among the nonlocal theories, those with more parameters in their formulations can usually provide better fits, e.g., a space fractional ADE with spatially variable dispersivity improves over a constant-dispersivity variant of the same model [*Zhang et al*., 2007]. The above observations suggest that all theories with increased parameterization can potentially provide improved fits to data, although ADE is the most parsimonious model.

The previous paragraph highlights an ongoing debate over the issue of transport formulation for describing tracer movement in heterogeneous aquifers. What makes this issue challenging is the complexity and uncertainty of subsurface heterogeneity, as field and laboratory studies can suffer from data scarcity, measurement support effects, and sampling or scale limitation. (There is also the issue of process uncertainty, as transient flows due to aquifer recharge can impact dispersion—this topic will be left to another treatment.) In sedimentary aquifers, heterogeneity of hydrological properties (notably, *K*) forms in response to dynamic processes, e.g., sea level changes, basement subsidence, sediment supply variation, etc. As a result, conductivity heterogeneity exists at multiple scales, exhibiting nested structures within a lithological hierarchy, i.e., sediment laminas nested within larger scale beds that are further organized into facies or facies assemblages [e.g., *Fogg*, 1990; *Scheibe and Freyberg*, 1995; *Webb and Anderson*, 1996; *Anderson*, 1997; *Scheibe and Yabusaki*, 1998; *Labolle and Fogg*, 2001; *Klise et al*., 2008; *Milliken et al*., 2008; *Comunian et al*., 2011]. At even greater scales, facies assemblages can give rise to aquifers and aquitards that are frequent targets in field-scale contamination studies. At a given problem scale (often containing one or more sediment hierarchy), heterogeneity can also exhibit long-range correlation or "connectivity," which can give rise to preferential flows or barriers that lead to early arrival and long tail in the solute breakthrough curve [*Wen and Gómez-Hernández*, 1998; *Zinn*, 2003; *Knudby and Carrera*, 2005]. At the MADE site, sedimentological and geophysical mapping confirm the existence of long-range facies connectivity that extends beyond the tracer test domain [*Bianchi et al*., 2011; *Meerschaert et al*., 2013]. Thus, on the one hand, hierarchical deposits have been explicitly modeled by combining large-scale lithological variations with the analysis of smaller scale heterogeneities [e.g., on the other hand, by explicitly modeling connectivities at a given problem scale, factors influencing preferential flow and transport can be evaluated [*Zheng and Gorelick*, 2003; *Salamon et al*., 2007; *Bianchi et al*., 2011]. Various connectivity definitions have been proposed by prior workers [*Renard and Allard*, 2013]. In this work, we define connectivities as static (i.e., those related to lithological variation) and dynamic (i.e., those related to flow and transport characteristics).

Despite the advances made in developing theory and field characterization techniques, practical problem solutions require efficient transport simulators. Because resolving heterogeneity down to the smallest resolvable continuum scale is impractical, when problem scale is large and site data are limited, flow and transport simulators must necessarily ignore heterogeneity at one or more smaller scales (or hierarchies). This necessity motivates the development of upscaling theories of flow and transport that develop deterministic or stochastic solutions of the governing equations to derive formulations with effective or equivalent parameters in order to capture bulk flow and transport behaviors arising out of the underlying heterogeneity [*Dagan*, 1989; *Gelhar*, 1993; *Dagan and Neuman*, 1997; *Cushman et al*., 2002; *Vogel and Roth*, 2003; *Frippiat and Holeyman*, 2008; *Fiori et al*., 2013]. Two parameterizations are common in upscaling: (1) heterogeneity is populated throughout the problem domain by assigning to each grid cell a grid-effective conductivity and dispersivity that can account for flow and transport behaviors arising out of the subgrid

heterogeneities [e.g., *Efendiev et al*., 2000; *Rubin*, 2003; *Fernàndez-Garcia and Gómez-Hernández*, 2007]; (2) heterogeneity is represented by a series of homogeneous facies or aquifers/aquitards units, ignoring subunit variation (hydrostratigraphic models, or HSMs). The first parameterization is frequently associated with geostatistical modeling, e.g., creating conditional realizations that are then coarsened to create a simulation model. The second parameterization, frequently invoked in larger scale studies lacking detailed field data, is more amenable to developing hierarchical models [*Monsen et al*., 2005; *Milliken et al*., 2008; *Ramanathan et al*., 2010; *Li et al*., 2011]. Upscaling for HSMs is the focus of this work.

Based on a three-dimensional (3-D) experimental stratigraphy exhibiting heterogeneity and connectivity at different scales, this study evaluates the ADE-based macrodispersion theory for upscaling transport with a suite of HSMs that captures lithological (static) connectivity at different sedimentary hierarchy. Equivalent conductivities are first computed for individual connectivity (or unit) of the HSMs. Transport upscaling is then carried out: in the heterogeneous reference model (i.e., experimental stratigraphy), ADE is assumed applicable; in the HSMs, ADE is parameterized with macrodispersivities to represent solute spreading due to unresolved, subunit-scale heterogeneity. The macrodispersion theory is chosen because it is the most widely studied, has shown utility for capturing field transport, and has matured to an extent that its underlying assumptions are generally understood [*Rubin*, 2003]. By comparison, upscaling theory for nonlocal formulations is in its infancy, while practical applicability of many nonlocal methods still remains to be demonstrated.Because the experimental stratigraphy was a unique outcome of a physical sedimentation experiment, it is not amenable to a geostatistical (i.e., multiple-realization) treatment. Flow and transport upscaling of this study is thus deterministic and adoption of the macrodispersion theory necessitates the working assumption that ensemble predictions can be applied to evaluating single or unique experiment. The ergodicity assumption has been adopted by prior workers when addressing issues with connectivity, i.e., a large problem domain many times the ln$K$ correlation range cannot be established [*Desbarats and Srivastava*, 1991; *Adams and Gelhar*, 1992; *Fernàndez-Garcia et al*., 2004, 2005; *Zhang and Gable*, 2008]. This assumption is necessary where long-range correlation exists in the field or in the laboratory, as the nature of the transport condition cannot be changed to suit theory. In evaluating the experimental stratigraphy, this study thus follows prior research in model conceptualization while focusing on the influence of connectivity resolution on upscaling at increasing system ln$K$ variances (0.1, 1.0, 4.5; K varies over 1, 3, and 6 orders of magnitude, respectively). The effect of explicit connectivity modeling on predicting non-Fickian transport by the ADE-based upscaled models is examined, yielding insights into why ADE can capture transport in some situations (e.g., site heterogeneity is moderate and/or modeled at high resolution capturing dominant connectivity), but not in others (e.g., sites with strong variability and/or models ignore or incorporate insufficient connectivity resolution). Because few hierarchical aquifer data have been analyzed for transport, this study also examines several dynamic connectivity measures in comparison to prior values reported in the literature.

In the remainder of this article, the heterogeneous reference model is introduced first, followed by a description of the procedure used to construct the HSMs. Flow and transport upscaling methods are presented next, followed by the results section which consists of: (1) flow upscaling and verification; (2) transport upscaling and verification; (3) dynamic connectivities. Insights of this study are summarized before conclusion and future research is indicated.

2. Methods

2.1. Model Creation

This study is based on stratigraphic data of an experimental deposit that exhibits hierarchical heterogeneity corresponding to physical sedimentation, i.e., fine-scale variations unique to local depositional processes are nested within larger scale, sand/clay transitions that formed in response to global forcings [*Sheets et al*., 2002; *Zhang et al*., 2010]. Compared to geostatistically generated models that are often devoid of connectivity [*Zinn*, 2003], the experimental data exhibit hierarchical structure not dissimilar to that observed at the MADE site [*Zheng et al*., 2011], e.g., sand-rich channel-like features embedded in floodplain clay, facies proportion and sizes exhibit spatial persistence, i.e., static connectivity. By scanning the sediment at high resolution and aligning the images in 3-D, a fully heterogeneous reference model (FHM) is created. This model is scaled to field dimensions ($L_x \times L_y \times L_z = 2500$ m $\times$ 2500 m $\times$ 100 m, of $N_x = 100$, $N_y = 100$, $N_z = 40$) to

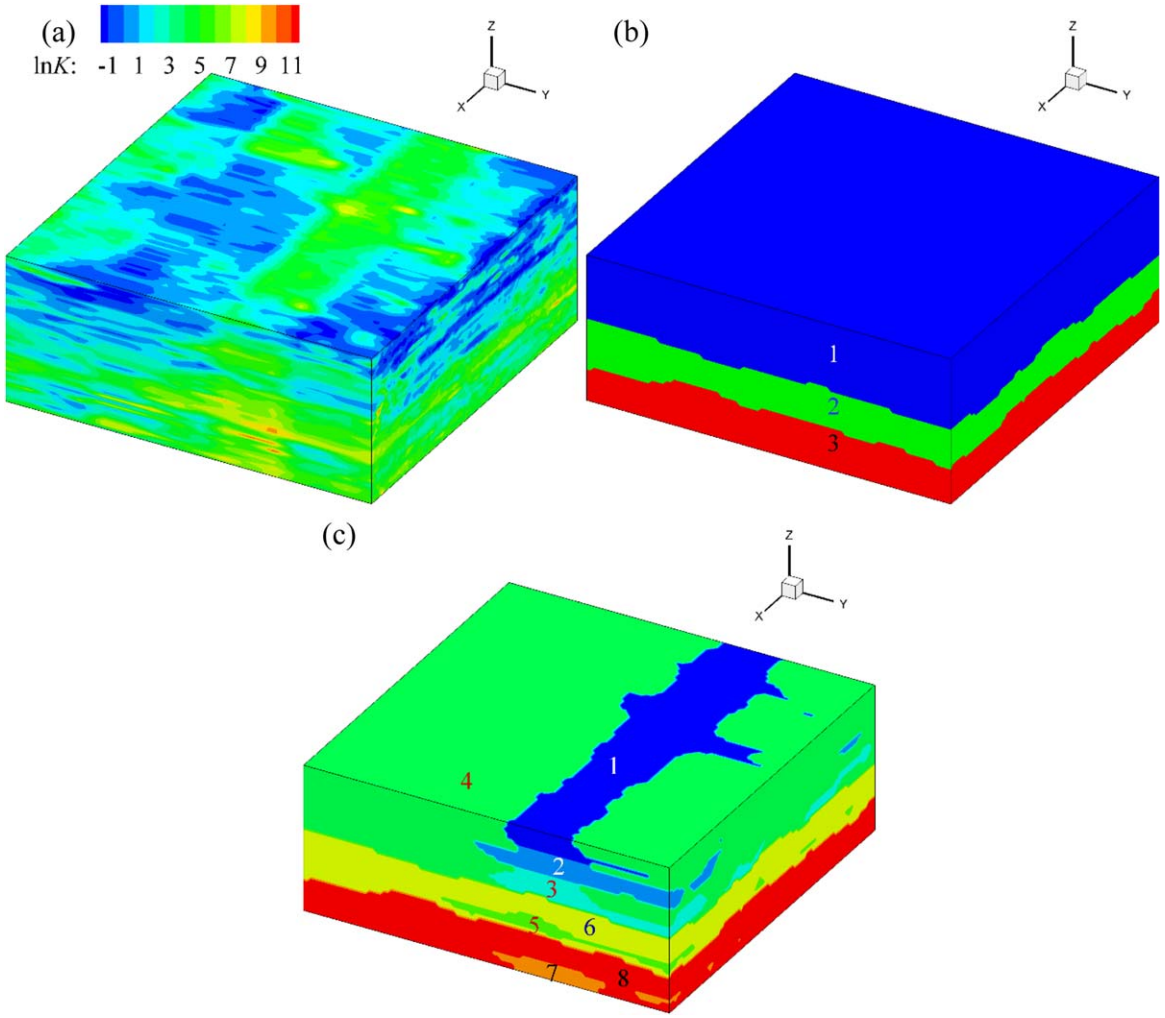

Figure 1. (a) The reference fully heterogeneous model withlocal *K* variation in natural log scale (system σ_f^2 is 4.5). *K* varies over 6 orders of magnitude in this model. Connectivity mapping at two scales: (b) 3-unit model, and (c) 8-unit model, while units of the latter model are nested within units of the former model.

create a synthetic aquifer with *K* variation mirroring sedimentation (Figure 1a). Each local *K* is assumed isotropic to facilitate transport upscaling with a well-known theory (see section 2.4).

To create the HSMs, lithology of the FHM was mapped to capture distinct facies (8-unit model; Figure 1c) before the facies were grouped into depositional environments (3-unit model; Figure 1b), which were further grouped into a single aquifer unit (1-unit model) (see detail in *Zhang et al.* [2011]). Because this procedure was carried out honoring lithological principles, the mapped connectivity is static. In practice, such models can be built using logging or geophysical data that are sensitive to formation lithology. The static connectivity is captured at different resolutions, in effect reflecting different levels of field characterization that can be carried out in practice. For each connectivity (or unit) of the HSMs, a geostatistical analysis estimated subunit ln*K* mean, σ_f^2, and integral scales (Table 1). This analysis was then repeated after increasing system ln*K* variance while fixing the mean ln*K*. At a given system variance, as connectivity resolution increases, subunit σ_f^2 becomes

Table 1. Integral Scales of ln*K* (m) for the HSM Units

Models	ID	λ_x	λ_y	λ_z
1-unit		155.0	690.0	5.0
3-unit	1	155.0	610.0	3.8
	2	140.0	900.0	12.0
	3	200.0	900.0	12.0
8-unit	1	155.0	610.0	3.5
	2	135.0	320.0	3.0
	3	135.0	700.0	3.4
	4	155.0	250.0	3.0
	5	155.0	275.0	7.5
	6	155.0	720.0	15.0
	7	230.0	300.0	3.0
	8	330.0	350.0	16.0

Table 2. Equivalent Hydraulic Conductivity Principal Components (m/yr) Computed With Flow-Based Upscaling[a]

		$\sigma_f^2 = 0.1$					$\sigma_f^2 = 1.0$					$\sigma_f^2 = 4.5$				
Models	ID	Var(lnK)	K_{xx}	K_{yy}	K_{zz}	α_L^M	Var(lnK)	K_{xx}	K_{yy}	K_{zz}	α_L^M	Var(lnK)	K_{xx}	K_{yy}	K_{zz}	α_L^M
1-unit		0.1	40.97	40.10	38.15	15.5	1.0	60.74	50.32	33.43	155.00	4.5	230.41	113.82	30.64	697.50
3-unit	1	0.078	34.13	33.30	32.63	12.09	0.784	32.56	26.03	22.54	121.52	3.528	58.63	24.81	17.35	546.84
	2	0.066	48.97	47.89	46.47	9.24	0.662	96.54	78.90	66.40	92.68	2.979	475.42	216.91	172.62	417.06
	3	0.063	46.26	45.46	44.83	12.60	0.629	80.15	68.17	60.43	125.80	2.831	330.03	178.35	121.00	566.06
8-unit	1	0.046	42.10	41.85	40.90	7.13	0.458	55.66	18.81	24.57	70.99	2.061	123.78	102.95	53.39	319.46
	2	0.048	43.65	43.20	42.63	6.48	0.482	63.88	26.22	47.88	65.07	2.169	179.05	129.85	72.34	292.82
	3	0.037	44.04	43.63	42.63	5.00	0.373	62.67	28.86	61.92	50.36	1.679	148.15	116.01	72.97	226.62
	4	0.046	29.59	29.55	28.48	7.13	0.464	18.66	26.33	46.51	71.92	2.088	13.46	14.17	3.78	323.64
	5	0.027	65.34	64.97	61.98	4.19	0.266	212.08	96.26	19.76	41.23	1.197	1715.69	1401.05	676.38	185.54
	6	0.050	45.55	44.91	43.64	7.75	0.504	72.99	71.82	23.40	78.12	2.268	227.64	141.98	84.52	351.54
	7	0.044	59.96	60.12	56.89	10.12	0.437	171.45	80.88	17.99	100.51	1.967	1288.16	1530.46	304.19	452.30
	8	0.055	44.49	43.96	43.35	18.15	0.546	68.33	69.90	18.32	180.18	1.967	208.41	135.81	95.29	810.81

[a]For all HSM units, system variance (σ_f^2) and unit-specific α_L^M (m) predicted by a first-order theory are also listed.

progressively smaller (Table 1). Finally, besides lithology, other static measures can also be used to map connectivity, e.g., percolation thresholds [*Hunt*, 2001; *Zhang et al*., 2010] and geostatistics-based ranking metrics [*Deutsch*, 1998].

2.2. Flow Upscaling

Flow upscaling was conducted to compute equivalent conductivity (**K***) for each unit of the HSMs [*Zhang et al*., 2011]: (1) the FHM was simulated solving the steady state incompressible flow equation under different global flow boundary conditions (BC), (2) for each unit, mean flux and hydraulic gradient were computed for each BC; (3) by imposing Darcy's Law using mean fluxes and gradients from all BC, **K*** was computed with a least-squares method. Given the system variances investigated ($\sigma_f^2 = 0.1, 1.0, 4.5$), three sets of upscaled **K*** were obtained for each HSM (Table 2). To eliminate numerical errors associated with grid coarsening, the HSMs employ the same grid as the FHM. Accuracy of the upscaled **K*** can be assessed by comparing flow predictions of the HSMs against those of the reference model under the same global flow BC (see 3.1).

2.3. Transport Modeling

One steady state flow experiment imposing a lateral hydraulic gradient along the *x* axis is selected for the transport analysis. Hydraulic heads of the left and right sides of the model are assigned constant values of 100 m and 10 m, respectively, and all other boundaries are no-flow. Flow is driven from the inflow boundary (x=0 m) to the outflow boundary (x=2500 m). Within the flow field, the release of a dilute, conservative tracer is simulated by all models (the computational domain and simulation grid are the same as the flow model). Given the *K* range (which changes with system variance), the simulated lateral transport is advection-dominated, and diffusion is ignored. In all models, advective-dispersive transport is simulated: local dispersion is assumed for the FHM; macrodispersion for the HSMs. Longitudinal macrodispersivity is estimated for the latter, as this parameter can be linked to geostatistical parameters of the underlying heterogeneity and because, for flow parallel to stratification, longitudinal spreading is significant compared to transverse spreading. Below, the transport formulation is briefly explained.

The continuum-scale ADE that describes transport of a dilute, conservative solute in groundwater is:

$$\frac{\partial c}{\partial t} = \nabla \cdot (\mathbf{D}\nabla c) - \nabla \cdot \left(\frac{\mathbf{q}}{\theta} c\right) \tag{1}$$

where c is solute concentration, **D** is dispersion tensor, **q** is Darcy flux, and θ is effective porosity. Groundwater velocity (**v**) is calculated as $\mathbf{q}/\theta$. In this work, θ is given a uniform value of 0.25, typical for sand-clay systems [*Freeze and Cherry*, 1979]. **D** is expressed as [*Bear*, 1988]:

$$\mathbf{D} = (\alpha_T V + D_d)\mathbf{I} + (\alpha_L - \alpha_T)\mathbf{vv}/V \tag{2}$$

where D_d is effective porous medium diffusion coefficient ($D_d = 0$ in this work), **I** is the identity matrix, α_L and α_T are longitudinal and transverse dispersivities, respectively, and V is magnitude of the groundwater velocity.

Equation (1) can be discretized to create a random walk particle tracking (RWPT) equation of the form [*Tompson and Gelhar*, 1990; *Kitanidis*, 1994]:

$$\mathbf{x}_p(t_n)=\mathbf{x}_p(t_{n-1})+\left[\mathbf{v}(\mathbf{x}_p(t_{n-1}),t_{n-1})+\nabla\cdot\mathbf{D}(\mathbf{x}_p(t_{n-1}),t_{n-1})\right]\Delta t+\mathbf{B}(\mathbf{x}_p(t_{n-1}),t_{n-1})\cdot\mathbf{z}_n\sqrt{\Delta t} \tag{3}$$

where $\mathbf{x}_p(t_n)$ is particle position at time t_n, $\mathbf{v}(\mathbf{x}_p(t_n), t_n)$ is groundwater velocity at $\mathbf{x}_p(t_n)$ and t_n, $\mathbf{D}(\mathbf{x}_p(t_n), t_n)$ is the dispersion tensor at $\mathbf{x}_p(t_n)$ and t_n, Δt is time step, and $\mathbf{z}_n$ is a vector of independent random variables of standard normal distribution. $\mathbf{B}(\mathbf{x}(t_n), t_n)$ is related to $\mathbf{D}(\mathbf{x}_p(t_n), t_n)$ as follows:

$$\mathbf{D}(\mathbf{x}(t_n),t_n)=\frac{1}{2}\mathbf{B}(\mathbf{x}_p(t_n),t_n)\cdot\mathbf{B}^{\mathrm{T}}(\mathbf{x}_p(t_n),t_n) \tag{4}$$

At the subgrid level, $\mathbf{v}(\mathbf{x}_p(t_n), t_n)$ is sampled from a set of semi-analytic functions that accurately delineate streamlines using bilinear interpolation of the interface Darcy fluxes [*Pollock*, 1988]. Under higher ln$K$ variances, divergence of dispersion could be significant in regions with high velocity gradients, equation (3) is thus solved for all models with $\nabla\cdot\mathbf{D}$ evaluated at every time step using finite differences.

For a given system variance, at the start of a RWPT simulation, 100,000 particles are released at $x = 300$ m, their positions uniformly distributed within a 60×775 m^2 area ($z \in [25, 85]$ m and $y \in [900, 1675]$ m). To compare results of the FHM and the upscaled models (where groundwater velocity is increasingly smoothed as connectivity resolution is reduced), the same tracer test is simulated by all models. To conserve mass in computing the tracer moments (next), particle tracking is terminated when the fastest particle reaches the outflow boundary. The remaining no-flow boundaries are set to reflect the particles back if any attempts to cross them. The time step size is chosen following this rule: at least 10 time steps are required for a particle to move through the fastest-flowing cell, thus particle motion is resolved at high temporal resolution throughout the simulation time [*Prickett et al.*, 1981; *Tompson et al.*, 1987]. Because of the explicit need to compute $\nabla\cdot\mathbf{D}$ at every time step and the fact that a large number of particles is needed to avoid artificial fluctuations in the computed breakthrough curve [*Salamon et al.*, 2006], a parallel RWPT code based on Message Passing Interface is developed, significantly reducing computation time. For a 3-D test problem simulating 100,000 particles, for example, the parallel code achieves 14× speedup using 32 processors. All simulations were run on the Yellowstone Supercomputer at the National Center for Atmospheric Research (Computational & Information Systems Lab).

For each tracer simulation, moment analysis is conducted to investigate the time evolution of solute mass centroid, average plume velocity, and spreading of the solute around its mass centroid. These moments are defined as:

$$M=\iiint_{\Omega}(\theta c)dxdydz \tag{5}$$

$$\mathbf{I}_p=\frac{1}{M}\iiint_{\Omega}(\mathbf{x}_p\theta c)dxdydz \tag{6}$$

$$\mathbf{s}^2=\frac{1}{M}\iiint_{\Omega}(\mathbf{x}_p-\mathbf{I}_p)(\mathbf{x}_p-\mathbf{I}_p)\theta c dxdydz \tag{7}$$

where Ω is the computational domain, M is total solute mass, $\mathbf{I}_p$ is mean displacement of solute mass centroid, and $\mathbf{s}^2$ is spatial covariance describing spreading of the solute about its centroid. The mean velocity of the plume ($\mathbf{v}_p$) is computed as [*Burr et al.*, 1994]:

$$\mathbf{v}_p=\frac{d\mathbf{I}_p}{dt} \tag{8}$$

The above central moments cannot reveal plume's higher moments such as skewness and early and late-time behavior. Solute breakthrough curve (BTC) is thus calculated at two downstream control planes at $x = 500$ m and $x = 1000$ m. Over time, the number of particles crossing each plane is counted to create a set of vertically integrated BTC.

2.4. Transport Upscaling

For the reference heterogeneous model, hydrodynamic dispersivities are assigned to equation (3) to represent local dispersion. As α_T is usually much less than α_L [*Bear*, 1988], α_L is set to 10^{-2} m and α_T is

ignored. Alternatively, local dispersion can be ignored entirely because its effect on large-scale solute spreading is usually negligible [*Rubin*, 2003; *Zhang and Gable*, 2008; *Fiori et al*., 2013]. To simulate transport in the HSMs, two upscaling formulations are tested: (1) unit-specific macrodispersivity: α_L^M is estimated for each unit of the HSMs to represent solute spreading due to unresolved, subunit-scale velocity variation, (2) time-dependent macrodispersivity: α_L^M is obtained from moment analysis of the tracer plume simulated by the FHM. For the upscaled models, because α_L^M is spatially or temporally variable, an enhanced degree of freedom in representing dispersion (i.e., as compared to using a single dispersivity) is employed. Moreover, because classic theories predict that macrodispersion scales with ln$K$ variance, transport upscaling is carried out at each system variance. Below, both approaches are briefly described.

In the first approach, a first-order stochastic theory is implemented to estimate spatially varying macrodispersivity [*Gelhar and Axness*, 1983; *Rubin*, 2003; *Fiori et al*., 2013]:

$$\alpha_L^M = \sigma_f^2 \lambda \tag{9}$$

$$\alpha_T^M = 0 \tag{10}$$

where λ is ln$K$ integral scale along mean flow direction (i.e., x axis), σ_f^2 is local ln$K$ variance describing subunit variability. As shown in Table 1, most HSM units are weakly to moderately heterogeneous, and, as connectivity resolution is increased (i.e., from 1 to 3 to the 8-unit models), *local* ln$K$ variances decrease. In equation (9), ln$K$ integral scales transverse to flow are not used, as statistical anisotropy is found to have minor effects on predicting BTC under similar transport conditions [*Zarlenga et al*., 2012; *Fiori et al*., 2013]. Tracer's initial vertical dimension (60 m) is large compared to vertical ln$K$ integral scales of the various connectivities (3∼16 m), satisfying theory requirement of a large plume in direction orthogonal to flow [*Dagan*, 1989; *Rubin*, 2003]. Additional simulations were carried out in the FHM using a larger initial plume size (70×1025 m^2), with results suggesting that tracer moments are not significantly affected. However, it must be pointed out that ergodicity as a working assumption cannot be strictly proven. Moreover, for the lateral transport regimes analyzed, transverse macrodispersivity is assigned zero. At all system variances, transverse expansion of the plume, as simulated by the FHM, is found negligible over time (not shown).

In the second approach, an apparent longitudinal macrodispersivity is obtained by analyzing tracer simulation in the FHM [*Dagan*, 1989], which can be traced to Einstein's original time-dependent dispersion concept [*Einstein*, 1905]:

$$\alpha_L^M(t) = \frac{1}{2}\frac{s_{xx}^2(t) - s_{xx}^2(0)}{\mathbf{I}_p(t) - \mathbf{I}_p(0)} \tag{11}$$

With equation (11), a time-dependent α_L^M can be obtained by fitting a function to the apparent α_L^M of the FHM experiment (the apparent α_T^M is again set to zero). This approach is analogous to situations where solute plume is monitored at high resolution with detailed measurements. Instead of evaluating α_L^M for every particle at every time step (as is done with the unit-specific approach, where α_L^M is evaluated depending on the position of each particle), the apparent α_L^M is assigned to all particles regardless of their positions. For a given system variance, the apparent α_L^M obtained from analyzing the FHM tracer test is assigned to all HSMs, regardless of their differences in connectivity resolution.

Because velocity simulated by the FHM becomes more strongly variable under increasing system variance, tracer experiment is simulated for 200 years, 40 years, and 4 years by all models, corresponding to system $\sigma_f^2 = 0.1$, 1.0 and 4.5, respectively.

2.5. Flow and Transport Connectivity

At each system variance, select flow and transport connectivity measures are computed for the FHM and each of the upscaled models. Unlike the static connectivity (i.e., lithology mapping) that defines the HSMs, dynamic connectivities can be strongly influenced by σ_f^2 and thus the variability of the velocity field. For fluid flow connectivity, the definition of *Knudby and Carrera* [2005] is chosen because it can potentially represent preferential flows:

$$CI = \frac{K_{xx}^{eff}}{K_G} \tag{12}$$

where CI is a flow connectivity index, K_G is geometric mean of the local conductivity, and K_{xx}^{eff} is an *effective* conductivity of the bulk flow field:

$$K_{xx}^{eff} = \frac{QL_x}{(h_1 - h_2)A} \tag{13}$$

where Q is bulk flow rate across the outflow boundary over $L_y \times L_z$, and h_1 and h_2 are the hydraulic heads applied at the inflow and outflow boundaries, respectively. For all models, K_{xx}^{eff} is computed from the reference or the upscaled flow field. For example, for the 8-unit model, only one K_{xx}^{eff} is computed, reflecting a global effective flow parameter.

For every model, two transport connectivity metrics are computed. The first metric is the power-law slope fitted to the BTC's tail in the log-log space [*Willmann et al*., 2008; *Renard and Allard*, 2013]. The second metric is defined by *Knudby and Carrera* [2005] as:

$$CT = \frac{t_{\text{peak,hom}}}{t_{\text{peak,het}}} \tag{14}$$

where $t_{\text{peak,het}}$ is peak breakthrough arrival time predicted by a heterogeneous model (i.e., FHM, 8-unit, and 3-unit models) at a given capture plane, and $t_{\text{peak,hom}}$ is peak breakthrough arrival time predicted by a homogeneous model (i.e., 1-unit model) at the same capture plane.

3. Results

3.1. Hydraulic Conductivity Upscaling and Flow Verification

For a given system variance, steady state flow is simulated in the FHM under different global BC [*Zhang et al*., 2011]. For each HSM unit, average hydraulic gradients and Darcy fluxes can be computed with which an equivalent **K*** can be estimated. For all units, equivalent **K***passed the Cholesky decomposition test [*Bhatia*, 2007], and is diagonally dominant because model coordinate is either parallel or orthogonal to stratification (Table 1 lists the principal components of **K***). To evaluate the accuracy of the equivalent **K***, the same flow experiments conducted for upscaling are repeated in the HSMs. Using the FHM as a reference, deviations in the average outflow rate and hydraulic head can be computed, which are found to vary with flow direction and system variance [*Zhang et al*., 2011]. Upscaling result of the lateral flow experiment is analyzed here with two error metrics of prediction, i.e., relative error in flow rate (*err*) and mean relative error (*MRE*) in hydraulic head:

$$\text{err} = \frac{|q_{\text{HSM}} - q_{\text{ref}}|}{q_{\text{ref}}} \times 100\%, \tag{15}$$

$$MRE = \frac{1}{I}\sum_{i=1}^{I} \frac{|h_{i,\text{HSM}} - h_{i,\text{ref}}|}{h_{\text{i,ref}}} \times 100\% \tag{16}$$

where q_{HSM} and q_{ref} represent average Darcy flux at the outflow boundary computed by the HSM and the FHM, respectively, I is number of grid cells within a HSM unit, and $h_{i,\text{HSM}}$ and $h_{i,\text{ref}}$ represent head computed by HSM and FHM at each cell location, respectively.

Figure 2a presents the *err* of the HSMs. For a given HSM, higher system ln$K$ variance leads to less accurate flow rate prediction. When variance is fixed, *err* of the 8-unit model is consistently the smallest, that of the 1-unit model consistently the largest. Clearly, along with variance, connectivity resolution plays a significant role: models with higher connectivity resolutions can better capture flow. Figure 2b compares the *MRE* of hydraulic head among the HSMs. Again, *MRE* increases with system variance: when $\sigma_f^2 = 0.1$, *MRE* is less than 2% for all models, but increases to 3.5–4.4% and 4.9–6.5% when $\sigma_f^2 = 1.0$ and 4.5, respectively. Hydraulic head prediction becomes less accurate with increasing σ_f^2. For a given system variance, *MRE* of the 8-unit model is the smallest, that of the 3-unit model the highest. To summarize, both system variance and connectivity resolution influence the accuracy of the upscaled flow fields. Increasing variance is also found to

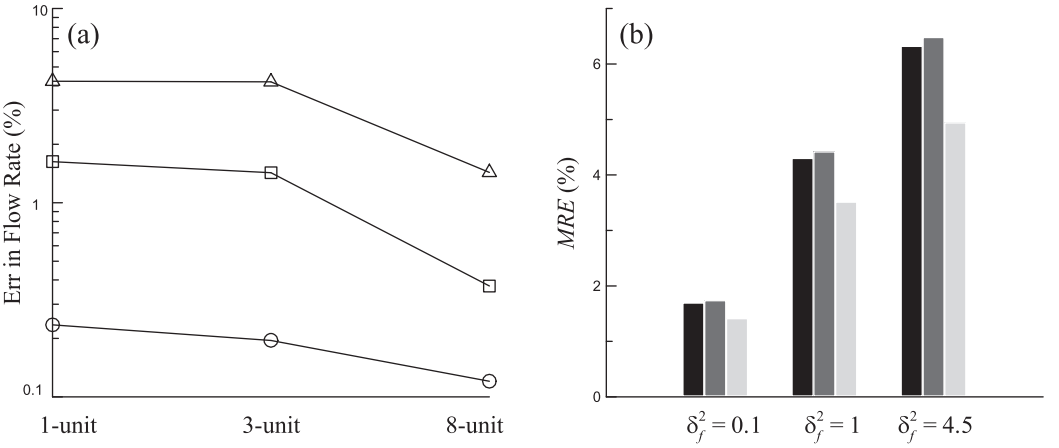

Figure 2. (a) Error in flow rate prediction by the HSMs at increasing system variances: $\sigma_f^2 = 0.1$ (circles), 1 (squares),and 4.5 (triangles). (b) *MRE* in hydraulic head prediction: 1-unit model (black), 3-unit model (dark gray), and 8-unit model (gray).

result in increasing horizontal-to-vertical anisotropy ratio (K_{xx}/K_{zz} or K_{xx}/K_{zz}) of **K***, as preferential flows start to form in the reference model [*Zhang et al*., 2010]. Figure 3 presents lateral Darcy flux computed by all models when system variance is 4.5. As connectivity resolution is reduced, velocity becomes increasingly smoothed, although the HSMs generally capture the mean velocity of the reference flow field.

3.2. Transport Simulations and Upscaling

Assuming identical initial concentration distribution, a conservative tracer is released into the flow fields of all models. The upscaled K_{xx}, computed for each HSM unit using flow properties (see above), are compared against an apparent K_{xx} inferred from the mean solute plume velocity (i.e., v_{Px}) when solute is traveling through the same unit: $K_{xx} = \theta v_{Px}/(\partial h/\partial x)$. To calculate the apparent K_{xx}, tracer initial dimensions were reduced to fit into each unit, so velocities from the other units are not sampled by solute particles. Apparent K_{xx} should approach the upscaled K_{xx} if solute has sampled most of the subunit velocities. (Using tracer moment to infer equivalent conductivity is a common practice, although it is not used here to replace flow upscaling because of the general difficulty of tracking a large number of particles inside each irregularly shaped HSM unit, and because such an approach can only lead to equivalent parameters along the mean flow direction). Table 3 presents this comparison for the 3-unit model. For all units, the two conductivities agree well with each other when $\sigma_f^2 = 0.1$ and 1.0, thus static connectivity mapping corresponds to dynamic flow connectivity. When $\sigma_f^2 = 4.5$, however, K_{xx} derived from v_{Px} overestimates the upscaled K_{xx} by 17% to 42%, which is attributed to the appearance of lateral preferential flows: particles channel through fast-flowing streamtubes within a HSM unit without sampling the slower velocities in the same unit, which leads to an overestimated K_{xx} compared to the upscaled K_{xx}. The latter is computed using *all* velocities within the unit, thus the effect of fast channeling is averaged out. At higher system variance, only a portion of the mapped static connectivity is dynamically connected.

3.2.1. Transport Simulation in the FHM

Time evolution of the mass centroid and longitudinal plume covariance (s_{xx}^2) of the reference model is first examined. At all variances, mass centroids over time are near straight lines (solid curves in Figures 4a–4c), suggesting that plume centroids move at constant speeds, consistent with the observation of *Dagan* [1989]. The centroid velocity (i.e., slope of a line fit) increases with variance, e.g., $v_{Px} = 7.5$, 16, and 138 m/yr for $\sigma_f^2 = 0.1$, 1.0, and 4.5, respectively. As preferential flows are developed under higher variance, mean lateral groundwater velocity is increasing, as is the equivalent K_{xx} (Table 1). At a fixed variance, s_{xx}^2 increases with time parabolically (solid curves in Figures 4d–4f), thus tracer not only expands continuously along mean flow, but rate of this expansion (i.e., the apparent α_L^M) increases with time. The apparent α_L^M, obtained with equation (11), also increases with σ_f^2 (Figure 5): when $\sigma_f^2 = 0.1$, it grows from 0 to 35 m over 200 years, but reaches as high as 150 m (in 48 years) and 250 m (in 4 years) when $\sigma_f^2 = 1.0$ and 4.5, respectively. At each variance, a third-order polynomial function of time is fitted, with a goodness-of-fit (R^2) greater than 99%. These functions will be used by the HSMs employing time-dependent macrodispersion.

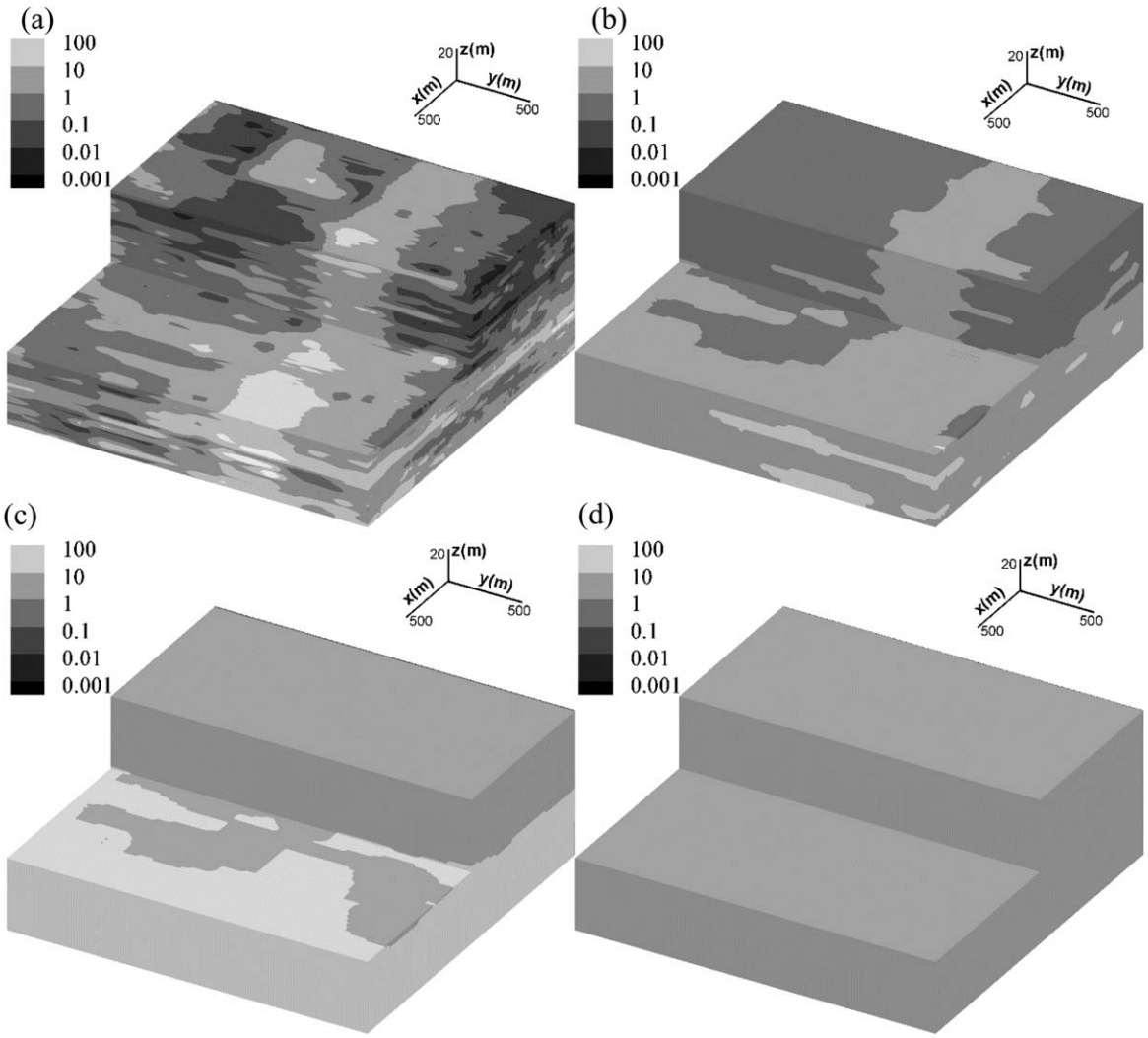

Figure 3. Dracy flux(qx) distribution for system variance of 4.5, with (a) FHM, (b) 8-unit model, (c) 3-unit model and, (d) 1-unit model. Note that $qx$of the FHM varies about 6 orders of magnitude.

Tracer simulated by the FHM is visualized next (Figure 6, first column). Of the total 100,000 particles, a random subset of 1,000 particles, capable of capturing the full extent of the plume, is plotted. When $\sigma_f^2 = 0.1$, the flow field is weakly heterogeneous and tracer expands slowly (Figure 5a). When $\sigma_f^2 = 1.0$, due to increased flow variability, tracer at 38.4 years is more laterally extensive than it is at 180 years under $\sigma_f^2 = 0.1$. When $\sigma_f^2 = 4.5$, tracer is the most laterally expansive: at 3.84 years, while tracer's leading edge nearly reaches the outflow boundary, most of the solute mass is still found near the source release plane. This phenomenon was observed at the MADE site with a similar level of K variability, although both downstream and upstream plume spreading was observed there at early times, possibly due to injection artifacts and transient flow effects [*Boggs et al*., 1992].

Breakthrough curve (BTC) can reveal tracer's higher moments including arrival, tailing, and symmetry. When $\sigma_f^2 = 0.1$, BTC at the first control plane ($x = 500$ m) is narrow and reaches a peak particle count (proxy for concentration) at $t = 30$ years (Figure 7a, solid curve). Due to the relatively homogeneous flow field and short travel distance, tracer lateral spreading is limited and BTC exhibits a slight asymmetry. At $x = 1000$ m, a stronger asymmetry is observed (Figure 7d, solid curve): over the longer travel distance, tracer has experienced more variable flow, resulting in a lower peak concentration (at $t = 110$ years) and more lateral spreading. This is similar to the behavior observed in *Fiori et al*. [2013]. When $\sigma_f^2 = 1.0$, due to increased flow variability, BTC at $x = 500$ m is more laterally spread out with a stronger asymmetry (Figure 7b, solid curve)

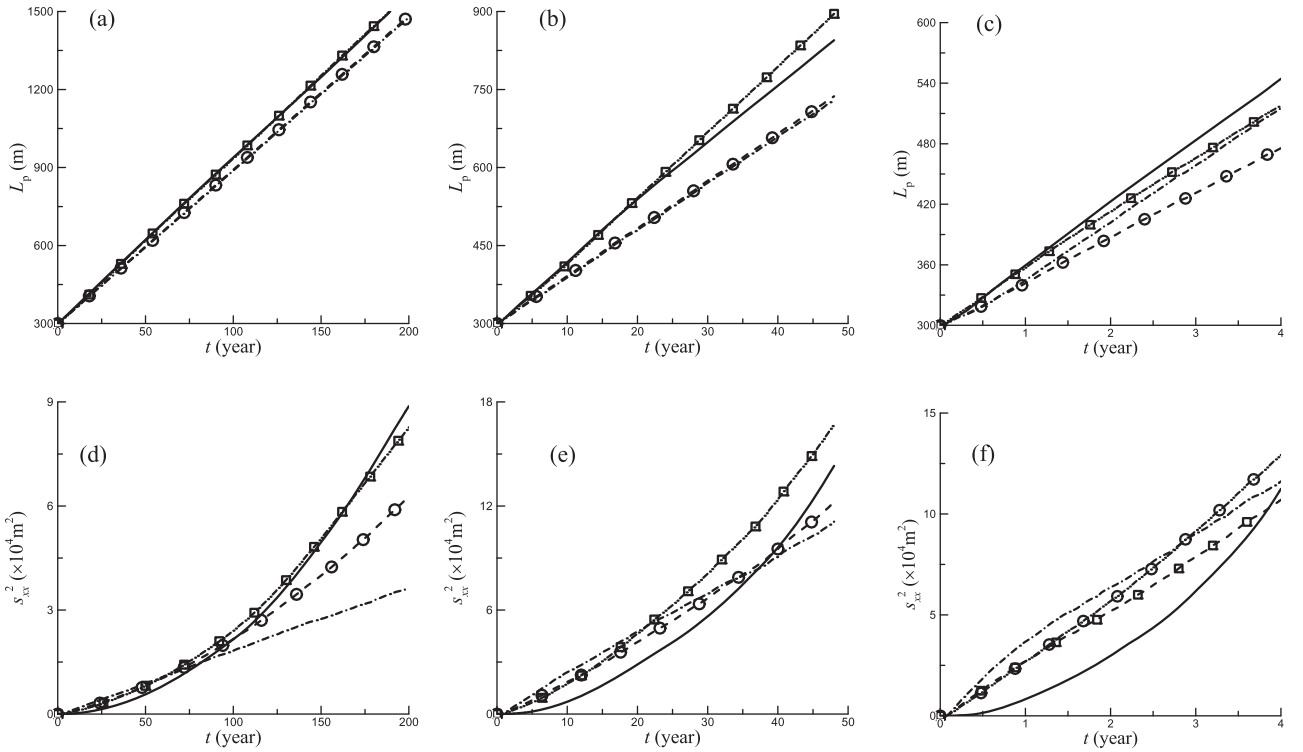

Figure 4. Time evolution of tracer moments using unit-specific macrodispersivity: mean plume displacement for $\sigma_f^2 =$ (a) 0.1, (b) 1.0, and (c) 4.5, respectively; longitudinal plume covariance for $\sigma_f^2 =$ (d) 0.1, (e) 1.0, and (f) 4.5, respectively. The solid, dash-dot, dashed-circle, and dash-square curves represent FHM, 1-unit, 3-unit,and 8-unit models, respectively.

compared to that observed when $\sigma_f^2 = 0.1$. As the result of a higher mean velocity, breakthrough peak also occurs earlier at $t = 15$ years. At $x = 1000$ m, BTC peaks at $t = 30$ years (Figure 7e, solid curve), while tracer has also expanded significantly compared to that observed at $x = 500$ m. When the leading edge of the plume reaches the outflow boundary, a large number of particles have not yet reached the second control plane. When $\sigma_f^2 = 4.5$, velocity variability is the strongest, i.e., q_x varies close to 6 orders of magnitude (Figure 3). BTC at $x = 500$ m is even more spread out (Figure 7c, solid curve) compared to those observed at lower system variances. BTC at $x = 1000$ m (Figure 7f, solid curve) reaches a peak concentration at 2.5 years, decreases briefly, before increasing again. While a significant number of particles have reached this control plane via fast-flowing pathways (i.e., the first peak), the remaining particles lag behind and are advecting slowly in the lower velocity zones.

3.2.2. Transport Upscaling (Unit-Specific Macrodispersion)

Using unit-specific macrodispersivities, tracer moments of the HSMs, computed with the same grid, initial particle distribution, and number of particles, are compared to the FHM (Figure 4). In visualizing the plumes, the same random subset of particles is used. At all system variances, plume centroid displacement is nearly linear with time, while that simulated by the 8-unit model is closest to that of the FHM. Because centroid displacement is determined by mean velocity, the 8-unit model yields the best bulk velocity field, allowing it to accurately capture the reference plume's position over time for all system variances. The 1 and 3-unit models, because their flow errors do not differ significantly, exhibit similar deviations in predicting the centroid velocity (Figure 2). Moreover, at all variances, s_{xx}^2 of the HSMs increases with time, indicating plume expansion. At all the times examined, because macrodispersion enhances mixing *within* individual units, the HSM plumes are better mixed compared to the reference plume. Below, tracer moments predicted by all models are compared in greater detail.

When $\sigma_f^2 = 0.1$, s_{xx}^2 of the FHM, 8-unit, and 3-unit models are parabolic (rate of plume expansion increases with time), while that of the 1-unit model is linear (constant rate). At t=60 years, all models display a similar plume size (Figure 6a, first row), corresponding to a similar s_{xx}^2 value at the same time (Figure 4d). At t=180 years (Figure 6a, second row), the 8-unit model accurately captures the lateral extent of the reference

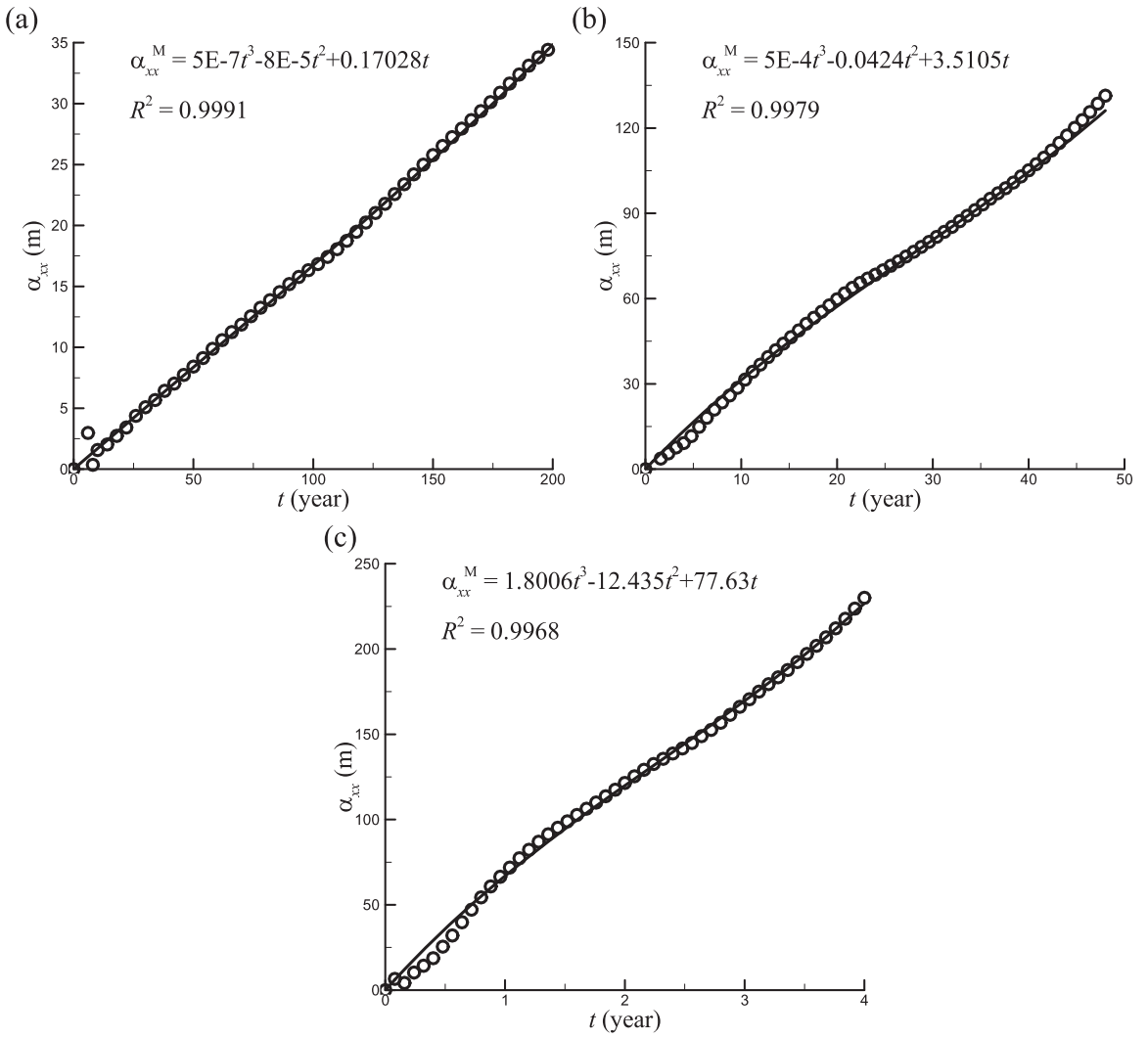

Figure 5. Apparent longitudinal macrodispersivity (circles) of the tracer simulated by the FHM under (a) $\sigma_f^2 = 0.1$, (b) $\sigma_f^2 = 1.0$, and (c) $\sigma_f^2 = 4.5$. A polynomial function (solid curve) is fitted with the goodness-of-fit shown.

plume, thus a HSM with high connectivity resolution can capture longitudinal spreading. When $\sigma_f^2 = 1.0$, s_{xx}^2 of the 8-unit model is (correctly) parabolic, while those of the 3 and 1-unit models are nearly linear (Figure 4e). At a fixed time, comparing s_{xx}^2 of a HSM with that of the same model under $\sigma_f^2 = 0.1$, lateral plume dimension is greater. For all except the 1-unit model, when lateral flow field is more variable, advection-controlled longitudinal spreading is enhanced. Because macrodispersivities increase with variance (Table 1), dispersion-controlled longitudinal spreading is also enhanced. All HSMs predict upstream dispersion, which is absent in the FHM. When $\sigma_f^2 = 4.5$, HSMs are not able to capture the parabolic behavior of the FHM (Figure 4f), although the 8-unit model is the least inaccurate. At higher system variance, upstream dispersion is also significant in the HSMs due to the greatly increased macrodispersivities.

BTCs of the HSMs at the control planes reveal that (Figure 7): (1) when variance is low, HSMs provide fairly accurate predictions of solute arrival, tailing, and overall breakthrough asymmetry. The observed tailing in these models can be attributed to the explicit modeling of connectivity, as groups of particles move at different mean velocities. Again, the 8-unit model is the most accurate at capturing the BTC. (2) when variance is higher, HSMs predict earlier arrival times, but capture the overall asymmetry at $x = 500$ m; at $x = 1000$ m, HSMs correctly predict the arrival time but cannot capture the BTC. The earlier ($x = 500$ m) underestimation of the arrival time is due to the fact that macrodispersivities predicted by theory reflect asymptotic values, which are usually achieved after solute has migrated over significant distances sampling a number of

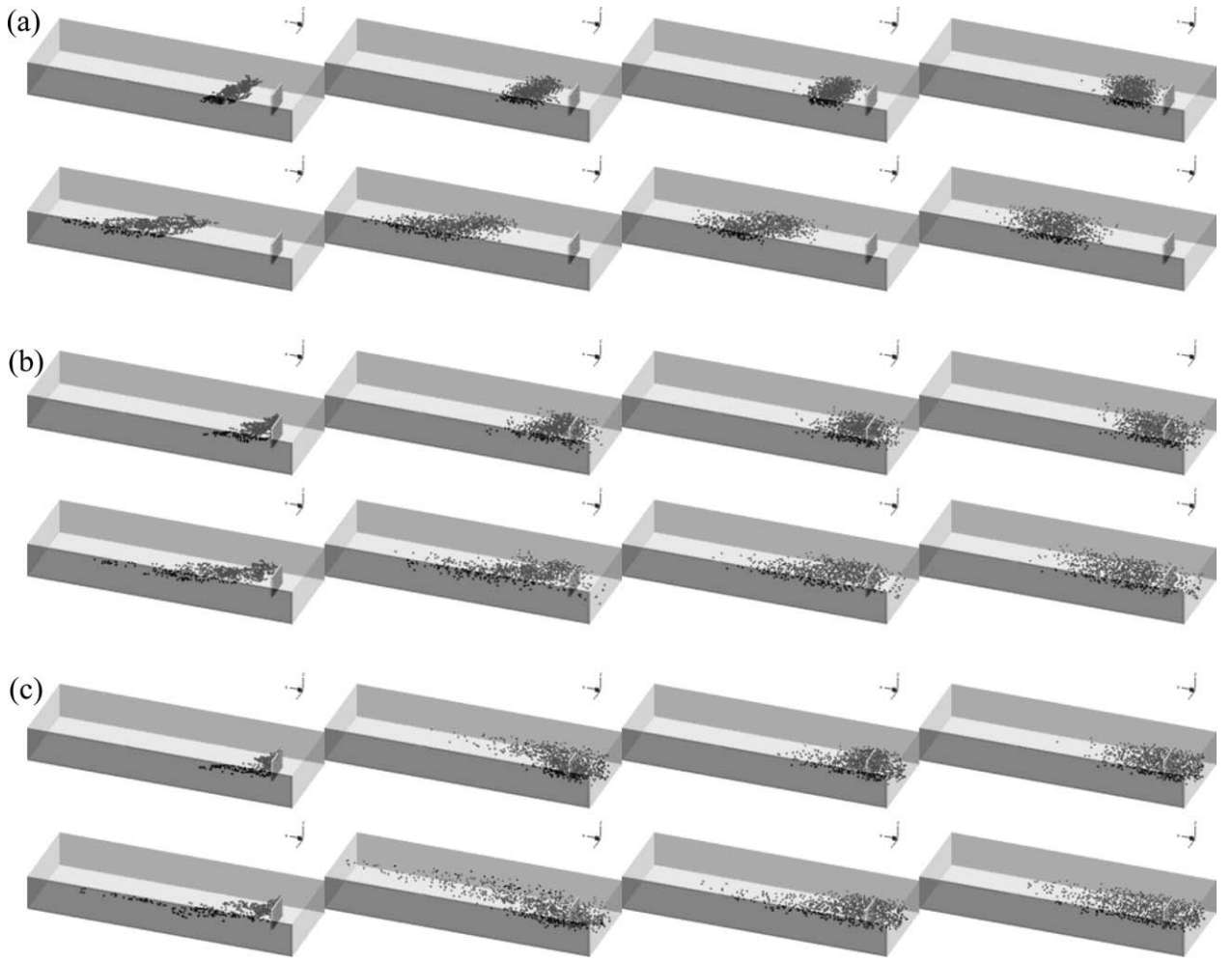

Figure 6. Particle locations simulated under (a) $\sigma_f^2 = 0.1$,(b) $\sigma_f^2 = 1.0$, and (c) $\sigma_f^2 = 4.5$. The first, second, third, and fourth columns represent tracer plumes simulated by the FHM, 8-unit, 3-unit, and 1-unit models, respectively. All HSMs employ unit-specific macrodispersion. The first row of each plot represents particle positions at (a) $t = 60$ years, (b) 12.8 years, and (c)1.28 years. The second row of each plot represents particle positions at (a)$t = 180$ years, (b)38.4 years, and (c) 3.84 years. Only a selectedsubset of 1000 particles is shown in each plot. Particle initial positions (light gray) are also shown.

heterogeneities. The later ($x = 1000$ m), more accurate, arrival prediction can be attributed to the fact that tracer has migrated over several lateral ln$K$ correlation scales (Table 2). (3) when variance is the highest, all HSMs predict poor BTC. Lithological mapping, though sufficient to capture flow and transport connectivity when variance is low, fails to do so when variance is high. This confirms the earlier observation when the apparent Kxx inferred from tracer velocity is higher than the upscaled Kxx.

3.2.3. Transport Upscaling (Time-Dependent Macrodispersion)

Time-dependent macrodispersion, when assigned to the HSMs, mimics the observed spreading in the FHM (Figure 5). When plume centroids are examined first (Figures 4 and 8), time-dependent macrodispersivity provides almost identical results at low-to-medium variances as those simulated previously with unit-specific macrodispersivities. When variance is higher, greater differences are observed, but mainly in results of the 8-unit model. Plume centroid averages the positions of all particles and appears less influenced by how macrodispersion is formulated. When plume size (i.e., s_{xx}^2) is examined next, results of the HSMs are no longer similar to those using unit-specific α_L^M. At all variances, s_{xx}^2 of the HSMs exhibits the characteristic parabolic behavior of the reference plume (Figure 8), thus the increasing rate of tracer expansion is captured. The time-dependent functions assigned to them (i.e., approximately linear growth of the apparent α_L^M with time) ensure this. At a given variance, the 8-unit model is the most accurate, despite the fact that the same time-dependent α_L^M is assigned to all HSMs. When variance increases, prediction of the HSMs degrades: at

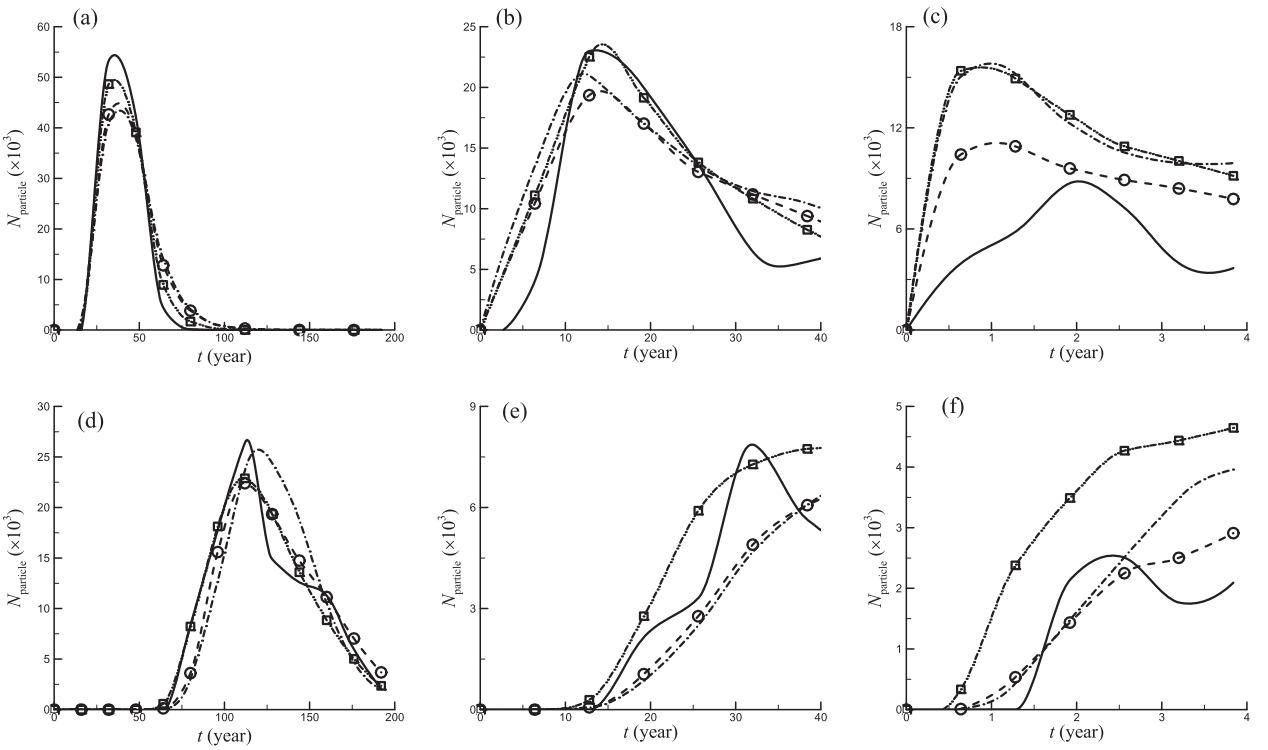

Figure 7. Breakthrough curves predicted by all models, with the HSMs using unit-specific macrodispersivity: at $x = 500$ m for $\sigma_f^2 =$ (a) 0.1, (b) 1.0, and (c) 4.5, respectively; at $x = 1000$ m for $\sigma_f^2 =$ (d) 0.1, (e) 1.0, and (f) 4.5, respectively. The solid, dash-dot, dash-circle,and dash-square curves represent FHM, 1-unit, 3-unit,and 8-unit models, respectively.

σ_f^2 of 4.5, all HSM predictions are quite poor (Figure 8f). Plumes visualized in Figure 9 reveal that the 8-unit model is still the best, as it approximately captures the leading edge of the reference plume even when variance is high. The time-dependent formulation also leads to reduced upstream dispersion near the tracer release plane (Figure 9). The apparent α_L^M is zero at $t = 0$, regardless of system variance (Figure 5).

BTCs of the HSMs at the control planes reveal that (Figure 10): (1) when variance is low, all HSMs except the 1-unit model predict the BTC well, and their predictions are similar to those of the unit-specific models (Figures 7a and 7d). (2) when variance is higher, HSMs become less accurate, although compared to the unit-specific models (Figure 7b), better arrival time is predicted at $x = 500$ m. This is likely a result of more accurately capturing the initially small plume with the apparent α_L^M. At $x = 1000$ m, however, compared to Figure 7e, there is no significant arrival time improvement. Due to the longer travel distance, asymptotic α_L^M adopted by the unit-specific models are not significantly inferior. (3) when variance is the highest, performance of the HSMs degrades further, although the 8-unit model can still capture the arrival times of the FHM at both control planes. The arrival time is significantly influenced by the existence of preferential flows in the FHM, which can be captured to some degree by the 8-unit model, but not by the others.

3.2.4. Sensitivity Analysis

Tracer simulations in the upscaled models generally yield a poor fit when system variance is high. Could these be numerical artifacts from insufficient discretization? Because a more refined flow grid can lead to more resolved (but not necessarily more accurate) subgrid as well as global streamlines, for $\sigma_f^2 = 4.5$, velocity field of the 8-unit model is recalculated with an 8× refinement, doubling each of *Nx, Ny*, and *Nz*. With the refined flow field, tracer simulation is repeated with unit-specific macrodispersivities. As shown in Figure 11, both mean plume displacement and longitudinal plume covariance are very close to those obtained with the original flow field. Moreover, increasing number of particles in the RWPT experiments can potentially improve the smoothness and accuracy of the computed tracer moments as well as BTC. However, results of the 8-unit model using 1,000,000 particles nearly coincide with the original results (Figure 11), thus the original number of particles are sufficient for the transport analysis of this study. Finally, for all system variances, when local dispersion is ignored, breakthrough curves computed by the FHM are virtually

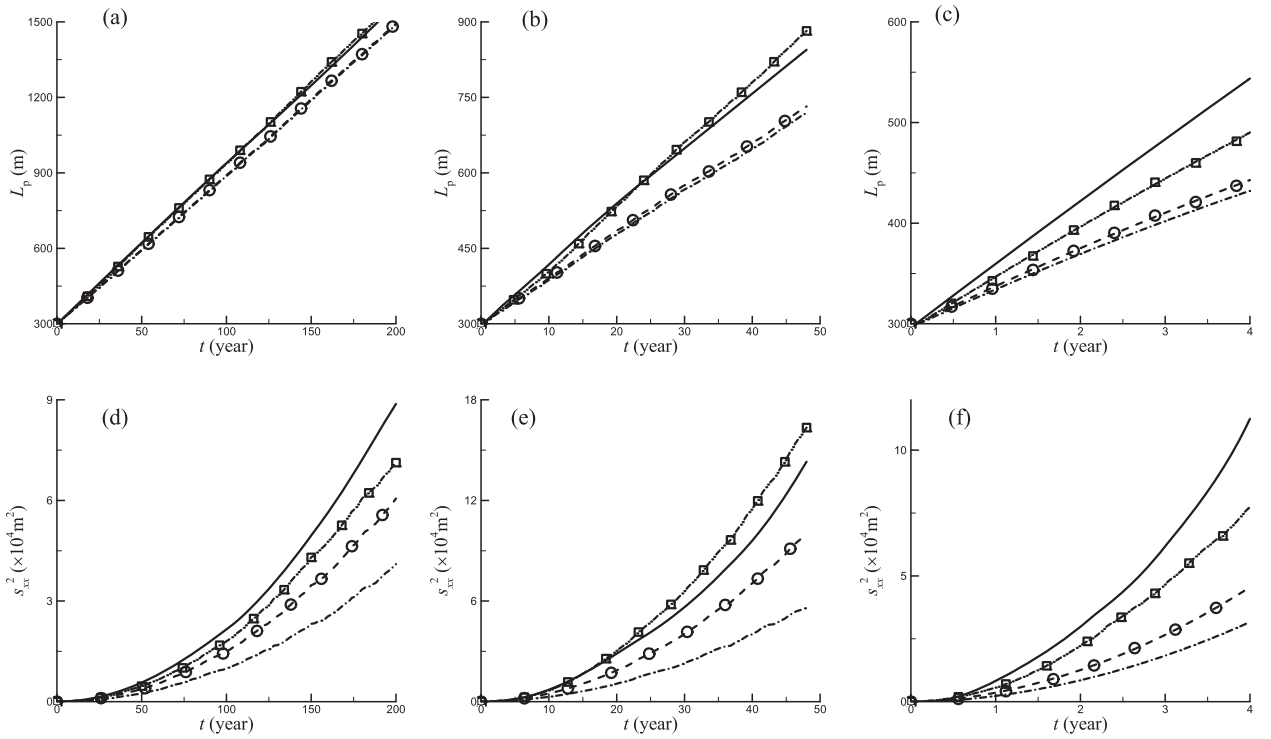

Figure 8. Evolution of plume moments predicted by all models, with the HSMs using time-dependent macrodispersivity: mean plume displacement for $\sigma_f^2 =$ (a) 0.1, (b) 1.0, and (c) 4.5, respectively; longitudinal plume covariance for $\sigma_f^2 =$ (d) 0.1, (e) 1.0,and (f) 4.5, respectively. The solid, dash-dot, dash-circle,and dash-square curves represent the FHM, 1-unit, 3-unit,and 8-unit models, respectively.

identical (not shown) to those presented earlier with nonnegligible local dispersion. For anisotropic heterogeneity where transport is advection-dominated, local dispersion generally has no discernable impact on large-scale solute spreading [*Fiori*, 1996].

3.3. Analysis of Flow and Transport Connectivity

For all models, K_{xx}^{eff} computed by equation (13) is greater than K_G, with a *CI* value ranging from 2.6 to 15.2 (Table 4). *CI* of the FHM is consistent with stratification, which amplifies horizontal flow. It also increases with system variance because of emerging preferential flow [*Zhang et al*., 2010]. For the HSMs, their *CI* values reflect the combination of explicit connectivity mapping and upscaling (i.e., equivalent ***K**** of each connectivity is generally anisotropic), both contributing to horizontal flows. When variance is low, all HSMs have a similar *CI* as that of the FHM. When variance is higher, greater differences emerge. For the 1-unit model, *CI* does not change with system variance. This suggests that when connectivity is not accounted for, *CI* is not a useful index of flow connectivity, because the emergence of preferential flow under high variance cannot be established. For the other HSMs, *CI* increases with σ_f^2 because connectivity is captured. When variance is high, the 8-unit model is best able to represent the flow connectivity of the FHM, as expected.

When comparing transport, HSMs under lower system variance and/or with higher connectivity resolution are better able to capture transport connectivities of the FHM. For the BTCs at the first control plane (x=500 m), results of power-law fitting and *CT* are shown in Table 5 and 6, respectively. For all variances, *CT* computed for the 3 and 8-unit models are close to each other, suggesting that this metric cannot accurately distinguish the difference in their transport connectivity. On the other hand, power-law slope can provide better quantification: at a given variance, with a few exceptions, it tends to increase with connectivity resolution (Table 5). Figure 12 compares *CT* versus power-law slope between this study (at the first control plane) and 2-D results from *Willmann et al*. [2008] for their "Type 2" (two heterogeneity scales but no preferential flow) and "Type 5" (one scale of heterogeneity but high-*K* cells are strongly connected) fields. When transport is 3-D, *CT* falls into a narrow range from 1.0 to 1.6, while in 2-D it ranges from 1.3 to 4.0. In 2-D, power law slope appears to decrease with *CT*; in 3-D, it varies independently of *CT*. Transport connectivity

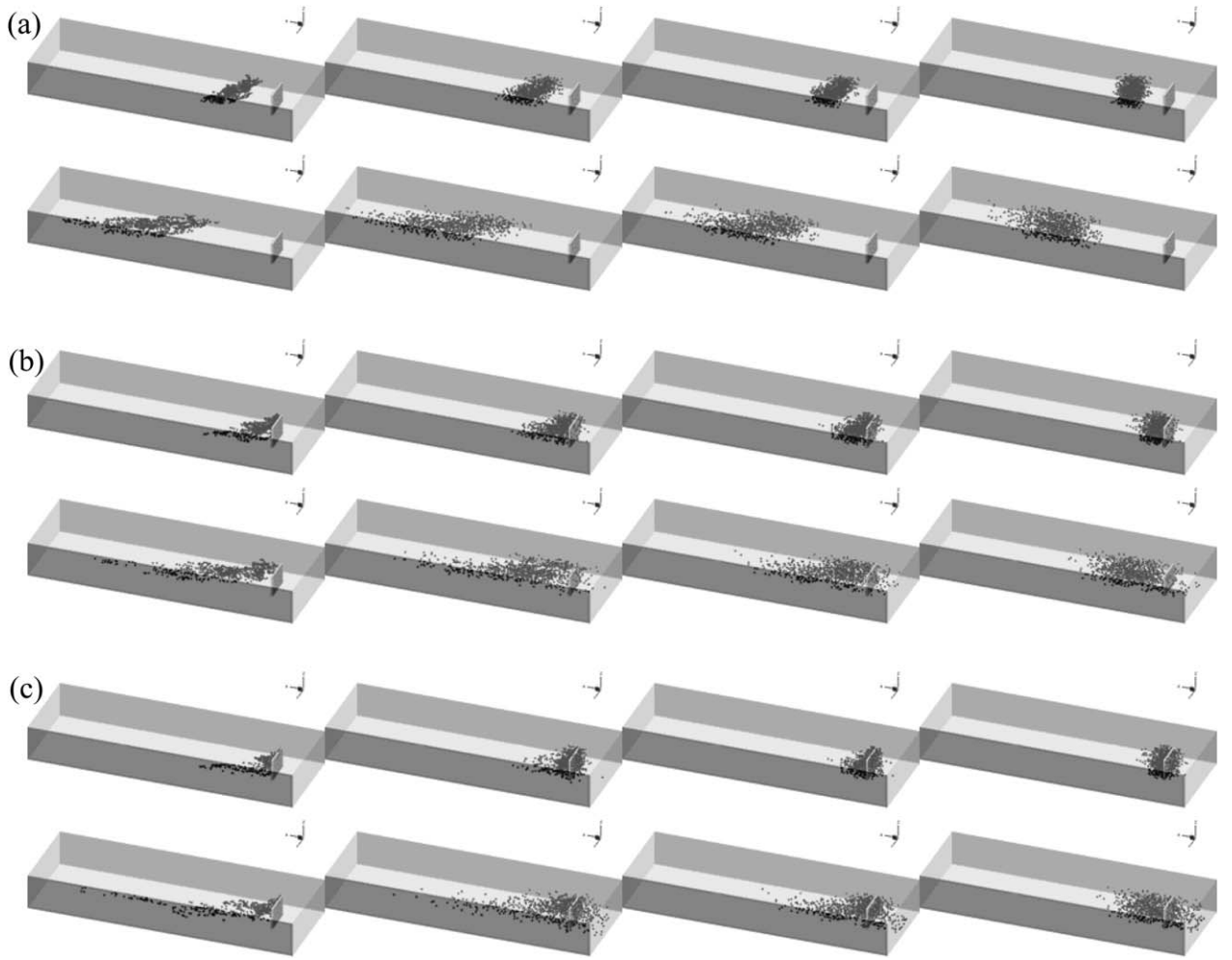

Figure 9. Particle locations simulated under(a) $\sigma_f^2 = 0.1$, (b) $\sigma_f^2 = 1.0$, and (c) $\sigma_f^2 = 4.5$. The first, second, third, and fourth columns represent tracer plumes simulated by the FHM, 8-unit, 3-unit and 1-unit models, respectively. All HSMs employ time-dependent macrodispersion. The first row of each plot represents particle positions at (a) $t = 60$ years, (b) 12.8 years, (c) 1.28 years. The second row of each plot represents particle positions at (a) $t = 180$ years,(b) 38.4 years, and (c) 3.84 years. Only a selected subset of 1000 particles is shown in each plot. Particle initial positions (light gray) are also shown.

behaves differently in 3-D because solute can more easily migrate around low-*K* features[*Fiori and Jankovic*, 2012].

4. Discussion

For a hierarchical aquifer model, ADE is assumed applicable to describing transport at the continuum scale: local dispersion is assigned to the FHM and macrodispersion to the HSMs. A 1-unit model ignoring all scales of heterogeneity provides a fair representation of the transport behavior of the FHM when system variance is low. When variance is higher, it becomes a poor choice: transport predictions using time-dependent α_L^M do not improve significantly over those using a constant α_L^M, despite the enhanced degree of freedom in representing dispersion. This is consistent with the interpretation of MADE tracer tests using a homogenous model [*Zheng et al*., 2011]. In comparison, the 3 and 8-unit models provide better predictions at all variances, thus an enhanced degree of freedom in representing dispersion can improve transport upscaling. Between them, the 8-unit model is more accurate, thus a higher connectivity resolution can further improve upscaling. Because solute travels through both high and low velocity zones due to the explicit modeling of connectivities, these models can capture non-Fickian transport such as breakthrough tailing and asymmetry. This effect is also illustrated in *Fiori et al*. [2013] who used statistically populated inclusions to represent

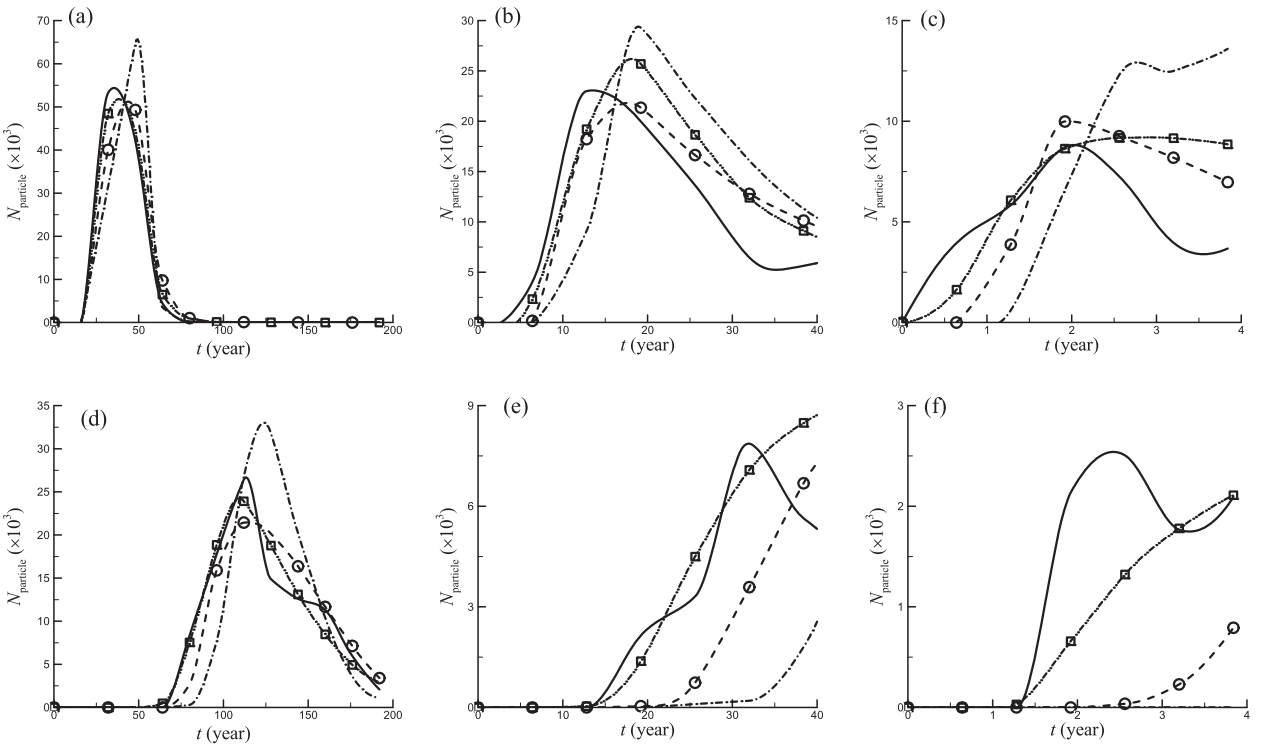

Figure 10. Breakthrough curves predicted by all models, with the HSMs using time-dependent macrodispersivity: at x= 500 m for σ_f^2= (a) 0.1, (b) 1.0, and (c) 4.5, respectively; at x= 1000 m for σ_f^2= (d) 0.1, (e) 1.0, and (f) 4.5, respectively. The solid, dash-dot, dash-circle, and dash-square curves represent the FHM, 1-unit, 3-unit, and 8-unit models, respectively.

low-velocity zones within a high-velocity matrix. At the Lauswiesen site in Germany where system ln$K$ variance is around 3.0, when heterogeneity was modeled at two scales (stochastic facies and subfacies correlated K distributions) that were conditioned to site static data, ADE as well as a purely advective model can capture depth-averaged BTC that exhibits heavy tails [*Riva et al.*, 2008]. In this case, inclusion of subgrid mass-transfer processes using a dual-porosity formulation did not lead to significant improvement. Together, the above studies suggest that ADE with an enhanced degree of freedom in representing dispersion can capture non-Gaussian transport due to the underlying (hierarchical) heterogeneity.

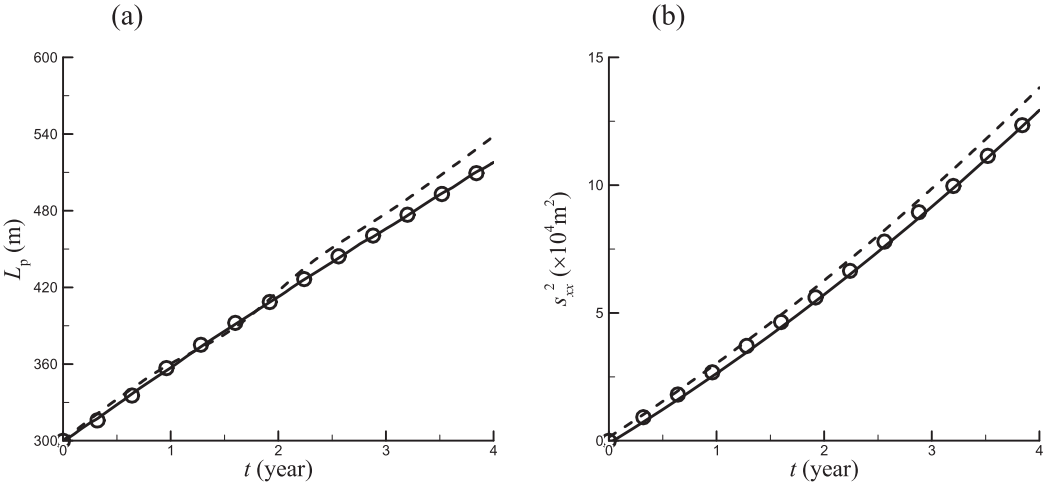

Figure 11. Time evolution of (a) mean plume displacement and (b) longitudinal plume covariance under σ_f^2= 4.5. The solid curve, dashed curve, and circle represent the simulation results with the 8-unit model using the original flow and tracer discretization, using a refined flow grid, and using a refined RWPT simulation with 1,000,000 particles, respectively.

Table 3. Upscaled K_{xx} (m/yr) for Units of the 3-Unit Model Compared to K_{xx} of the Same Units Inferred From Mean Plume Velocity

	Unit 1		Unit 2		Unit 3	
System Variance	Upscaled K_{xx}	K_{xx} From Mean Plume Velocity	Upscaled K_{xx}	K_{xx} From Mean Plume Velocity	Upscaled K_{xx}	K_{xx} From Mean Plume Velocity
$\sigma_f^2 = 0.1$	34.24	34.13	49.11	48.97	46.20	46.26
$\sigma_f^2 = 1.0$	32.56	32.80	96.54	96.92	80.15	81.21
$\sigma_f^2 = 4.5$	58.63	68.05	475.42	588.54	330.03	467.51

For the transport problems tested, predictive ability of the alternative macrodispersion formulations does not differ significantly. Both approaches are fairly accurate when implemented with the 8-unit model and/or when system variance is low. With the 3 and 1-unit models, both perform fairly well in capturing breakthrough tailing and asymmetry at low-to-medium σ_f^2. Differences between the two do exist. For example, time-dependent α_L^M is able to capture the rate of lateral plume expansion over time, even with the 1-unit model. Such an effect is not well captured with the unit-specific α_L^M. During early migration, time-dependent α_L^M predicts more accurate solute arrival time while reducing upstream dispersion, althoughthis approach requires detailed tracer measurements while unit-specific models only need static (geostatistical) parameters. For all variances, the 8-unit model is the best predictor, regardless of the formulation used: when connectivity is sufficiently resolved, the type of data conditioning for modeling transport appears less critical. However, what resolution is "sufficient" is likely problem dependent, and future work needs to test more heterogeneities. Furthermore, how upscaled models should be conditioned by data is influenced by prediction goal. If the location/speed of plume centroid is of interest, data type used to condition transport does not matter significantly, especially when system variance is low to moderate. If early prediction is of interest, detailed measurements as required by the time-dependent models are more appropriate. If late-time behavior is of interest, the type of data again becomes less important.

When aquifer variability is weak (e.g., $\sigma_f^2 \leq 1$), all upscaled models are fairly robust and increased accuracy can be achieved with higher connectivity resolutions. This is consistent with the observations at the Cape Cod and Borden sites, where aquifers are weakly heterogeneous and longitudinal spreading of the measured tracers is in fair agreement with theory. When system exhibits strong variability, however, all macrodispersion models perform poorly, which is attributed to their general failure to capture preferential flows in the FHM. In these cases, lithological variation cannot accurately capture dynamic connectivity. In this study, connectivity was delineated by kriging [*Zhang et al*., 2011] which is a smooth interpolator that can lead to classification errors that then contribute to upscaling errors, e.g., high-*K* cells assigned to low-*K* facies or connected thin lenses become separated. Such issues cannot be remedied easily using macrodispersion, although a finer connectivity resolution (i.e., further division of the 8-unit model) may improve prediction. However, techniques that can distinguish dynamic connectivity are needed, while for problems where such connectivity cannot be practically identified, pre-asymptotic or higher order theories, or one or more nonlocal formulations, should be explored. Upscaling will again aim to map dynamic transport behaviors to parameters of these models.

Models of this study reveal insights into flow and transport behavior in hierarchical media, based on which we propose an upscaling strategy with 3 steps: (1) large-scale connectivity, preferably corresponding to dominant transport pathways, is first identified [*Monsen et al*., 2005]. (2) after capturing such connectivity, effective conductivity can be estimated *without* conducting flow upscaling using, e.g., (a) tracer test; (b) analytic-stochastic techniques subject to similar variability constraints [*Zhang et al*., 2007]; (c) parameter estimation techniques that can infer effective parameters from the observed state variables [*Irsa and Zhang*, 2012; *Zhang*, 2014]. (3) after the flow field has been upscaled, transport upscaling is conducted by conditioning to either spatial statistics assuming that a local stationary variogram is applicable, or to tracer moments using time-dependent formulation. Note that a similar approach was suggested by *Anderson* [1997], as explicit modeling of connected features is believed to exert a stronger control on predicting transport than smaller scale heterogeneities within such features [e.g., *Fogg*, 1986; *Jussel and Stauffer*, 1994; *Poeter and Townsend*, 1994]. This study suggests that accuracy of such an approach will

Table 4. Flow Connectivity (*CI*) Computed for All Models Under Increasing System Variances

System Variance	1-Unit Model	3-Unit Model	8-Unit Model	FHM
$\sigma_f^2 = 0.1$	2.59	2.62	2.65	2.71
$\sigma_f^2 = 1.0$	2.59	2.91	3.25	4.01
$\sigma_f^2 = 4.5$	2.59	3.96	6.00	15.16

Table 5. Power-Law Slopes Fitted to Breakthrough Tailing at $x=500$ m for All Models at Increasing System Variances

σ_f^2	0.1	1.0	4.5
1-unit	1.57	0.72	0.60
3-unit	1.57	0.90	0.33
8-unit	2.08	1.33	0.46
FHM	2.91	2.73	3.06

depend on whether dynamic connectivity is captured at sufficient detail as well as the underlying system variability, i.e., higher variability will likely require a finer resolution. However, these insights may change when a different heterogeneity is evaluated depending on, e.g., how realistic it is to assume that a local stationary variogram can describe heterogeneity within individual connectivities. To verify this, not only will we need to seek a different connectivity mapping scheme robust to variance, we also need to address the local stationarity assumption. For a given problem, when connectivity resolution (i.e., spatial division) is increased, local variances of the individual connectivities will decrease. Can a threshold be reached such that potential local nonstationarity can be ignored? In studies that tested upscaling theories on nonstationary media with bimodal, channeled, and hierarchical heterogeneities [*Desbarats*, 1990; *Desbarats and Srivastava*, 1991; *Zhang and Gable*, 2008], theory provides reasonable predictions when (local) ln$K$ variances are relatively low.

5. Conclusion

Solute transport in hierarchical porous media is examined by developing hydrostratigraphic models (HSMs) integrating large-scale connectivity mapping with flow and transport upscaling. A laboratory-based synthetic aquifer, which exhibits hierarchical heterogeneity (FHM), provides a reference hydraulic conductivity model. Within the sedimentary hierarchy, HSMs with different lithological (static) connectivity resolutions are created: an 8-unit facies model, a 3-unit depositional model, and a 1-unit homogeneous model. For each connectivity (or unit) of the HSMs, equivalent hydraulic conductivity is first calculated using flow-based upscaling. In the computed flow field that is parallel to stratification, an instantaneous, conservative tracer is simulated by all models. While local dispersion is modeled in the FHM, transport is upscaled for the HSMs using alternative approaches: (1) macrodispersivities, conditioned to geostatistical parameters of subunit heterogeneity, are assigned to the HSMs using a first-order theory; (2) time-dependent macrodispersivities, conditioned to detailed tracer measurements from the FHM, are assigned to the same models. In both flow and transport upscaling, increasing system ln$K$ variance (0.1, 1.0, 4.5) reflecting field-scale variability is tested.

For all variances tested, HSMs provide fair to good bulk flow predictions, with relative errors in flow rate and hydraulic head less than 5% and 7%, respectively. For a given model, upscaling errors of flow increase with variance. When variance is fixed, HSMs with increased connectivity resolution are more accurate. Among them, the 8-unit model provides the best flow predictions at all variances. In transport modeling, tracer migration (i.e., mass centroid, longitudinal plume covariance, breakthrough curve, peak concentration) of the FHM can be captured well by the HSMs with higher connectivity resolutions, but upscaling errors of transport increase with variance as well. Importantly, when connectivity is explicitly resolved, an enhanced degree of freedom in representing dispersion can improve the ADE-based models by capturing non-Fickian transport of the FHM. This suggests that nonlocal theories which use more parameters than dispersivity may have similarly benefited. When connectivity is sufficiently resolved, the type of data used to condition transport also becomes less critical. Data conditioning, however, is influenced by the prediction goal. Moreover, 3-D transport connectivities of the hierarchical aquifer analyzed in this work differ quantitatively from those analyzed for 2-D systems, consistent with prior observations.

When aquifer is weak-to-moderately heterogeneous ($\sigma_f^2 \leq 1$), upscaled ADE can adequately capture transport, despite the existence of hierarchical heterogeneity at smaller scales. For such media, accurate transport upscaling can be accomplished with low connectivity resolutions. At the weakly heterogeneous Cape Cod and Borden sites, spreading of the observed plumes is in fair agreement with theories. When aquifer exhibits stronger variability, the upscaled models perform poorly, which is attributed to the failure of static connectivity to capture preferential flows (i.e., dynamic connectivity) in the FHM. This observation is consistent with

Table 6. Transport Connectivity Computed for All Models at Increasing System Variances Using Peak Times in the Simulated BTC at $x=500$ m

σ_f^2	0.1	1.0	4.5
3-unit	1.03	1.06	1.10
8-unit	1.05	1.06	1.10
FHM	1.16	1.23	1.59

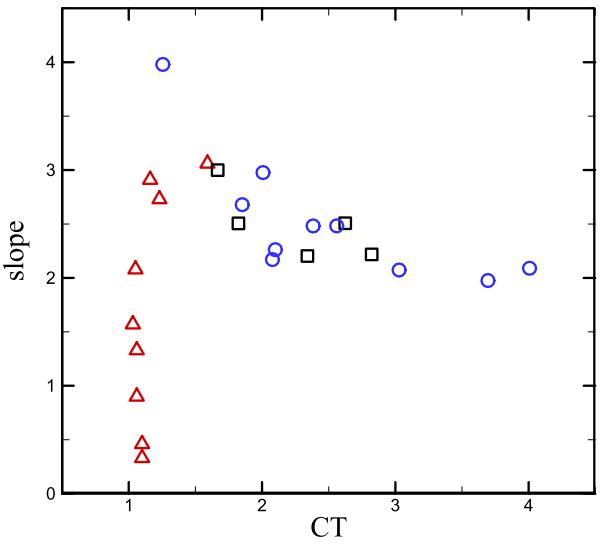

Figure 12. *CT* versuspower-law fitted slope. Triangles, squares, and circles represent result from the present study (FHM, 8 and 3-unit models), "Type 2"fields data [*Willmann et al*., 2008], and "Type 5" fields data [*Willmann et al*., 2008], respectively.

tracer interpretations at the MADE site. *Renard and Allard* [2013] provide a review of flow and transport connectivities, which will be examined along with a new inversion approach to develop improved connectivity mapping schemes that are robust to system variance.

The experimental stratigraphy offers one example of a hierarchical heterogeneity. Results and insights of this study thus pertain to this one heterogeneity and cannot yet be generalized to other systems. Because aquifer heterogeneity tends to be site specific, additional studies analyzing different heterogeneities are needed to help reveal insights that are more universal in nature. However, the upscaling method of this study is general and the equivalent conductivities are tensor properties that can be used to capture bulk flow for complex geometries. The study method can thus be applied to analyzing problems with any connectivity features. Future work can further assess the ergodicity condition as a working assumption, for which a stochastic approach is likely needed, i.e., instead of using one reference FHM for upscaling, an ensemble of such reference models will be created and analyzed. Such an approach will increase the computational burden but is straightforward to implement.

Acknowledgments

The data for this paper are available at Community Surface Dynamics Modeling System (Data set: Hydrography; Data set name: 3-D ADE simulation). The research is supported by the U.S. Department of Energy, Office of Fossil Energy, grant DE-FE-0009238. We would like to acknowledge the use of computational resources (ark:/85065/d7wd3xhc) at the NCAR-Wyoming Supercomputing Center, which are provided by the National Science Foundation and the State of Wyoming and are supported by NCAR's Computational and Information Systems Laboratory.

References

Adams, E. E., and L. W. Gelhar (1992), Field study of dispersion in a heterogeneous aquifer: 2. Spatial moments analysis, *Water Resour. Res.*, *28*(12), 3293–3307, doi:10.1029/92WR01757.

Anderson, M. P. (1997), Characterization of geological heterogeneity, in *Subsurface Flow and Transport: A Stochastic Approach*, edited by G. Dagan, and P. Neuman, pp 23–43, Cambridge Univ. Press, Cambridge, U. K.

Barlebo, H. C., M. C. Hill, and D. Rosbjerg (2004), Investigating the Macrodispersion Experiment (MADE) site in Columbus, Mississippi, using a three-dimensional inverse flow and transport model, *Water Resour. Res.*, *40*, W04211, doi:10.1029/2002WR001935.

Bear, J. (1988), *Dynamics of Fluids in Porous Media*, Dover Civ. Mech. Eng. Ser., Dover, Mineola, N. Y.

Benson, D. A., S. W. Wheatcraft, and M. M. Meerschaert (2000), Application of a fractional advection-dispersion equation, *Water Resour. Res.*, *36*(6), 1403–1412, doi:10.1029/2000WR900031.

Berkowitz, B., and H. Scher (1998), Theory of anomalous chemical transport in random fracture networks, *Phys. Rev. E*, *57*(5), 5858–5869, doi:10.1103/PhysRevE.57.5858.

Berkowitz, B., A. Cortis, M. Dentz, and H. Scher (2006), Modeling non-Fickian transport in geological formations as a continuous time random walk, *Rev. Geophys.*, *44*, RG2003, doi:10.1029/2005RG000178.

Bhatia, R. (2007), *Positive Definite Matrices*, Princeton Univ. Press, Princeton, N. J.

Bianchi, M., C. Zheng, C. Wilson, G. R. Tick, G. Liu, and S. M. Gorelick (2011), Spatial connectivity in a highly heterogeneous aquifer: From cores to preferential flow paths, *Water Resour. Res.*, *47*, W05524, doi:10.1029/2009WR008966.

Boggs, J. M., S. C. Young, L. M. Beard, L. W. Gelhar, K. R. Rehfeldt, and E. E. Adams (1992), Field study of dispersion in a heterogeneous aquifer, 1. Overview and site description, *Water Resour. Res.*, *28*(12), 3281–3291, doi:10.1029/92WR01756.

Bohling, G. C., G. Liu, S. J. Knobbe, E. C. Reboulet, D. W. Hyndman, P. Dietrich, and J. J. Butler (2012), Geostatistical analysis of centimeter-scale hydraulic conductivity variations at the MADE site, *Water Resour. Res.*, *48*, W02525, doi:10.1029/2011WR010791.

Burr, D. T., E. A. Sudicky, and R. L. Naff (1994), Nonreactive and reactive solute transport in three-dimensional heterogeneous porous media: Mean displacement, plume spreading, and uncertainty, *Water Resour. Res.*, *30*(3), 791–815, doi:10.1029/93WR02946.

Cirpka, O. A., and P. K. Kitanidis (2000), An advective-dispersive stream tube approach for the transfer of conservative-tracer data to reactive transport, *Water Resour. Res.*, *36*(5), 1209–1220, doi:10.1029/1999WR900355.

Comunian, A., P. Renard, J. Straubhaar, and P. Bayer (2011), Three-dimensional high resolution fluvio-glacial aquifer analog—Part 2: Geostatistical modeling, *J. Hydrol.*, *405*(1-2), 10–23, doi:10.1016/j.jhydrol.2011.03.037.

Cushman, J. H., and T. R. Ginn (1993), Nonlocal dispersion in media with continuously evolving scales of heterogeneity, *Transp. Porous Media*, *13*(1), 123–138.

Cushman, J. H., L. S. Bennethum, and B. X. Hu (2002), A primer on upscaling tools for porous media, *Adv. Water Resour.*, *25*(8-12), 1043–1067, doi:10.1016/S0309-1708(02)00047-7.

Cvetkovic, V., H. Cheng, and X. Wen (1996), Analysis of nonlinear effects on tracer migration in heterogeneous aquifers using Lagrangian travel time statistics, *Water Resour. Res.*, *32*(6), 1671–1680.

Dagan, G. (1989), *Flow and Transport in Porous Formations*, Springer, Berlin.

Dagan, G., and S. P. Neuman (1997), *Subsurface Flow and Transport: A Stochastic Approach*, Cambridge Univ. Press, N. Y.

Dentz, M., A. Cortis, H. Scher, and B. Berkowitz (2004), Time behavior of solute transport in heterogeneous media: Transition from anomalous to normal transport, *Adv. Water Resour.*, *27*(2), 155–173, doi:10.1016/j.advwatres.2003.11.002.
Desbarats, J. (1990), Macrodispersion in sand-shale sequences, *Water Resour. Res.*, *26*(l), 153–163.
Desbarats, J., and R. M. Srivastava (1991), Geostatistical characterization of groundwater flow parameters in a simulated aquifer, *Water Resour. Res.*, *27*(5), 687–698, doi:10.1029/90WR02705.
Deutsch, C. V. (1998), Fortran programs for calculating connectivity of three-dimensional numerical models and for ranking multiple realizations, *Comput. Geosci.*, *24*(1), 69–76, doi:10.1016/S0098–3004(97)00085-X.
Efendiev, Y., L. J. Durlofsky, and S. H. Lee (2000), Modeling of subgrid effects in coarse-scale simulations of transport in heterogeneous porous media, *Water Resour. Res.*, *36*(8), 2031–2041, doi:10.1029/2000WR900141.
Einstein, A. (1905), Über die von der molekularkinetischen Theorie der Wärme geforderte Bewegung von in ruhenden Flüssigkeiten suspendierten Teilchen, *Ann. Phys.*, *322*(8), 549–560.
Feehley, C. E., C. Zheng, F. J. Molz, S. Carolina, and A. Abstract (2000), A dual-domain mass transfer approach for modeling solute transport in heterogeneous aquifers: Application to the Macrodispersion Experiment (MADE) site, *Water Resour. Res.*, *36*(9), 2501–2515.
Fernàndez-Garcia, D., and J. J. Gómez-Hernández (2007), Impact of upscaling on solute transport: Traveltimes, scale dependence of dispersivity, and propagation of uncertainty, *Water Resour. Res.*, *43*, W02423, doi:10.1029/2005WR004727.
Fernàndez-Garcia, D., T. H. Illangasekare, and H. Rajaram (2004), Conservative and sorptive forced-gradient and uniform flow tracer tests in a three-dimensional laboratory test aquifer, *Water Resour. Res.*, *40*, W10103, doi:10.1029/2004WR003112.
Fernàndez-Garcia, D., T. H. Illangasekare, and H. Rajaram (2005), Differences in the scale dependence of dispersivity and retardation factors estimated from forced-gradient and uniform flow tracer tests in three-dimensional physically and chemically heterogeneous porous media, *Water Resour. Res.*, *41*, W03012, doi:10.1029/2004WR003125.
Fiori, A. (1996), Finite Peclet extensions of Dagan's solutions to transport in anisotropic heterogeneous formations, *Water Resour. Res.*, *32*(1), 193–198.
Fiori, A., and I. Jankovic (2012), On preferential flow, channeling and connectivity in heterogeneous porous formations, *Math. Geosci.*, *44*, 133–145, doi:10.1007/s11004-011-9365-2.
Fiori, A., G. Dagan, I. Jankovic, and A. Zarlenga (2013), The plume spreading in the MADE transport experiment: Could it be predicted by stochastic models?, *Water Resour. Res.*, *49*, 2497–2507, doi:10.1002/wrcr.20128.
Fogg, G. E. (1986), Groundwater flow and sand body interconnectedness in a thick, multiple-aquifer system, *Water Resour. Res.*, *22*(5), 679–694, doi:10.1029/WR022i005p00679.
Fogg, G. E. (1990), Architecture and interconnectedness of geologic media: Role of the low permeability facies in flow and transpo, in *Hydro-Geology of Low Permeability Environments*, edited by S. P. Neuman and I. Neretnieks, pp. 19–40, Heinz Heis, Hannover, Germany.
Freeze, R. A., and J. A. Cherry (1979), *Groundwater*, Prentice Hall, Englewood Cliffs, N. J.
Frippiat, C. C., and A. E. Holeyman (2008), A comparative review of upscaling methods for solute transport in heterogeneous porous media, *J. Hydrol.*, *362*(1-2), 150–176, doi:10.1016/j.jhydrol.2008.08.015.
Garabedian, S. P., and D. R. Leblanc (1991), Large-scale natural gradient tracer test in sand and gravel, Cape Cod, Massachusetts 2. Analysis of spatial moments for a nonreactive tracer, *Water Resour. Res.*, *27*(5), 911–924.
Gelhar, L. W. (1993), *Stochastic Subsurface Hydrology*, Prentice Hall, Upper Saddle River, N. J.
Gelhar, L. W., and C. L. Axness (1983), Three-dimensional stochastic analysis of macrodispersion in aquifers, *Water Resour. Res.*, *19*(1), 161–180.
Ginn, T. R. (2001), Stochastic–convective transport with nonlinear reactions and mixing: Finite streamtube ensemble formulation for multicomponent reaction systems with intra-streamtube dispersion, *J. Contam. Hydrol.*, *47*(1), 1–28, doi:10.1016/S0169-7722(00)00167-4.
Haggerty, R., S. A. Mckenna, and L. C. Meigs (2001), On the late-time behavior of tracer test breakthrough curves, *Water Resour. Res.*, *36*(12), 3467–3479.
Harvey, C., and S. M. Gorelick (2000), Rate-limited mass transfer or macrodispersion: Which dominates plume evolution at the macrodispersion experiment (MADE) site?, *Water Resour. Res.*, *36*(3), 637–650.
Hunt, A. G. (2001), Applications of percolation theory to porous media with distributed local conductances, *Adv. Water Resour.*, *24*(3-4), 279–307, doi:10.1016/S0309-1708(00)00058-0.
Irsa, J., and Y. Zhang (2012), A direct method of parameter estimation for steady state flow in heterogeneous aquifers with unknown boundary conditions, *Water Resour. Res.*, *48*, W09526, doi:10.1029/2011WR011756.
Jussel, P., and F. Stauffer (1994), Transport modeling in heterogeneous aquifers : 1. Statistical description and numerical generation of gravel deposits of the aquifer, *Water Resour. Res.*, *30*(6), 1803–1817.
Kitanidis, P. K. (1994), Particle-tracking equations for the solution of the advection-dispersion equation with variable coefficients, *Water Resour. Res.*, *30*(11), 3225–3227.
Klise, K. A., V. C. Tidwell, and S. A. McKenna (2008), Comparison of laboratory-scale solute transport visualization experiments with numerical simulation using cross-bedded sandstone, *Adv. Water Resour.*, *31*(12), 1731–1741, doi:10.1016/j.advwatres.2008.08.013.
Knudby, C., and J. Carrera (2005), On the relationship between indicators of geostatistical, flow and transport connectivity, *Adv. Water Resour.*, *28*(4), 405–421, doi:10.1016/j.advwatres.2004.09.001.
Labolle, E. M., and G. E. Fogg (2001), Role of molecular diffusion in contaminant migration and recovery in an alluvial aquifer system, *Transp. Porous Media*, *42*(1-2), 155–179.
Li, S., Y. Zhang, and X. Zhang (2011), A study of conceptual model uncertainty in large-scale CO2 storage simulation, *Water Resour. Res.*, *47*, W05534, doi:10.1029/2010WR009707.
Liu, G., Y. Chen, and D. Zhang (2008), Investigation of flow and transport processes at the MADE site using ensemble Kalman filter, *Adv. Water Resour.*, *31*(7), 975–986, doi:10.1016/j.advwatres.2008.03.006.
Meerschaert, M. M., D. A. Benson, and B. Ba (1999), Multidimensional advection and fractional dispersion, *Phys. Rev. E*, *59*(5), 5026–5028.
Meerschaert, M. M., M. Dogan, R. L. Van Dam, D. W. Hyndman, and D. A. Benson (2013), Hydraulic conductivity fields: Gaussian or not?, *Water Resour. Res.*, *49*, 4730–4737, doi:10.1002/wrcr.20376.
Milliken, W. J., M. Levy, S. Strebelle, C. Energy, T. Company, and Y. Zhang (2008), The effect of geologic parameters and uncertainties on subsurface flow: Deepwater depositional systems, in *SPE Western Regional and Pacific Section AAPG Joint Meeting, SPE 114099*, Society of Petroleum Engineers, pp. 1–16.
Monsen, E., T. Randen, L. Sonneland, and J. E. Odegard (2005), Geological model building: A hierarchical segmentation approach, in *Mathematical Methods and Modeling in Hydrocarbon Exploration and Production*, edited by A. Iske and T. Randen, pp. 213–245, Springer, N. Y.
Neuman, S. P. (1993), Eulerian-Lagrangian Theory of transport in space-time nonstationary velocity fields: Exact nonlocal formalism by conditional moments and weak approximation, *Water Resour. Res.*, *29*(3), 633–645.
Neuman, S. P. (2003), Multifaceted nature of hydrogeologic scaling and its interpretation, *Rev. Geophys.*, *41*(3), 1014, doi:10.1029/2003RG000130.

Neuman, S. P., and D. M. Tartakovsky (2009), Perspective on theories of non-Fickian transport in heterogeneous media, *Adv. Water Resour.*, *32*(5), 670–680, doi:10.1016/j.advwatres.2008.08.005.
Poeter, E., and P. Townsend (1994), Assessment of critical flow path for improved remediation management, *Ground Water*, *32*(3), 439–447.
Pollock, D. W. (1988), Semianalytical computation of path lines for finite-difference models, *Ground Water*, *26*(6), 743–750, doi:10.1111/j.1745–6584.1988.tb00425.x.
Prickett, T. A., T. G. Naymik, and C. G. Longquist (1981), *A "Random-Walk" Solute Transport Model for Selected Groundwater Quality Evaluations*, Ill. State Water Surv., Champaign.
Ramanathan, R., A. Guin, R. W. Ritzi, D. F. Dominic, V. L. Freedman, T. D. Scheibe, and I. Lunt (2010), Simulating the heterogeneity in braided channel belt deposits: 1. A geometric-based methodology and code, *Water Resour. Res.*, *46*, W04515, doi:10.1029/2009WR008111.
Rehfeldt, K. R., J. M. Boggs, and L. W. Gelhar (1992), Field study of dispersion in a heterogeneous aquifer 3. Geostatistical analysis of hydraulic conductivity, *Water Resour. Res.*, *28*(12), 3309–3324.
Renard, P., and D. Allard (2013), Connectivity metrics for subsurface flow and transport, *Adv. Water Resour.*, *51*, 168–196, doi:10.1016/j.advwatres.2011.12.001.
Riva, M., A. Guadagnini, D. Fernandez-Garcia, X. Sanchez-Vila, and T. Ptak (2008), Relative importance of geostatistical and transport models in describing heavily tailed breakthrough curves at the Lauswiesen site., *J. Contam. Hydrol.*, *101*(1-4), 1–13, doi:10.1016/j.jconhyd.2008.07.004.
Riva, M., L. Guadagnini, and A. Guadagnini (2010), Effects of uncertainty of lithofacies, conductivity and porosity distributions on stochastic interpretations of a field scale tracer test, *Stochastic Environ. Res. Risk Assess.*, *24*(7), 955–970, doi:10.1007/s00477-010-0399-7.
Rubin, Y. (2003), *Applied Stochastic Hydrogeology*, Oxford Univ. Press, N. Y.
Salamon, P., D. Fernàndez-Garcia, and J. J. Gómez-Hernández (2006), A review and numerical assessment of the random walk particle tracking method., *J. Contam. Hydrol.*, *87*(3-4), 277–305, doi:10.1016/j.jconhyd.2006.05.005.
Salamon, P., D. Fernàndez-Garcia, and J. J. Gómez-Hernández (2007), Modeling tracer transport at the MADE site: The importance of heterogeneity, *Water Resour. Res.*, *43*, W08404, doi:10.1029/2006WR005522.
Scheibe, T., and S. Yabusaki (1998), Scaling of flow and transport behavior in heterogeneous groundwater systems, *Adv. Water Resour.*, *22*(3), 223–238, doi:10.1016/S0309-1708(98)00014-1.
Scheibe, T. D., and D. L. Freyberg (1995), Use of sedimentological information for geometric simulation of natural porous media structure, *Water Resour. Res.*, *31*(12), 3259–3270, doi:10.1029/95WR02570.
Sheets, B. A., T. A. Hickson, and C. Paola (2002), Assembling the stratigraphic record: Depositional patterns and time-scales in an experimental alluvial basin, *Basin Res.*, *14*(3), 287–301, doi:10.1046/j.1365-2117.2002.00185.x.
Tompson, A. F. B., and L. W. Gelhar (1990), Numerical Simulation of Solute transport in three-dimensional, randomly heterogeneous porous media, *Water Resour. Res.*, *26*(10), 2541–2562.
Tompson, A. F. B., E. G. Vomvoris, and L. W. Gelhar (1987), Numerical simulation of solute transport in randomly heterogeneous porous media: Motivation, model development, and application, *Rep. UCID-21281*, Lawrence Livermore Natl. Lab., Livermore, Calif.
Vogel, H. J., and K. Roth (2003), Moving through scales of flow and transport in soil, *J. Hydrol.*, *272*(1-4), 95–106, doi:10.1016/S0022-1694(02)00257-3.
Webb, E. K., and M. P. Anderson (1996), Simulation of preferential flow in three-dimensional, heterogeneous conductivity fields with realistic internal architecture, *Water Resour. Res.*, *32*(3), 533–545, doi:10.1029/95WR03399.
Wen, X. H., and J. J. Gómez-Hernández (1998), Numerical modeling of macrodispersion in heterogeneous media: A comparison of multi-Gaussian and non-multi-Gaussian models, *J. Contam. Hydrol.*, *30*(1-2), 129–156, doi:10.1016/S0169-7722(97)00035-1.
Willmann, M., J. Carrera, and X. Sánchez-Vila (2008), Transport upscaling in heterogeneous aquifers: What physical parameters control memory functions?, *Water Resour. Res.*, *44*, W12437, doi:10.1029/2007WR006531.
Zarlenga, A., I. Janković, and A. Fiori (2012), Advective transport in heterogeneous formations: The impact of spatial anisotropy on the breakthrough curve, *Transp. Porous Media*, *96*(2), 295–304, doi:10.1007/s11242-012-0088-8.
Zhang, Y. (2014), Nonlinear inversion of an unconfined aquifer: Simultaneous estimation of heterogeneous hydraulic conductivities, recharge rates, and boundary conditions, *Transp. Porous Media*, *102*(2), 275–299, doi:10.1007/s11242-014-0275-x.
Zhang, Y., and C. W. Gable (2008), Two-scale modeling of solute transport in an experimental stratigraphy, *J. Hydrol.*, *348*(3-4), 395–411, doi:10.1016/j.jhydrol.2007.10.017.
Zhang, Y., D. a. Benson, M. M. Meerschaert, and E. M. LaBolle (2007), Space-fractional advection-dispersion equations with variable parameters: Diverse formulas, numerical solutions, and application to the macrodispersion experiment site data, *Water Resour. Res.*, *43*, W05439, doi:10.1029/2006WR004912.
Zhang, Y., C. W. Gable, and B. Sheets (2010), Equivalent hydraulic conductivity of three-dimensional heterogeneous porous media: An upscaling study based on an experimental stratigraphy, *J. Hydrol.*, *388*(3-4), 304–320, doi:10.1016/j.jhydrol.2010.05.009.
Zhang, Y., B. Liu, and C. W. Gable (2011), Homogenization of hydraulic conductivity for hierarchical sedimentary deposits at multiple scales, *Transp. Porous Media*, *87*(3), 717–737, doi:10.1007/s11242-010-9711-8.
Zheng, C., and S. M. Gorelick (2003), Analysis of solute transport in flow fields influenced by preferential flowpaths at the decimeter scale, *Ground Water*, *41*(2), 142–155, doi:10.1111/j.1745-6584.2003.tb02578.x.
Zheng, C., M. Bianchi, and S. M. Gorelick (2011), Lessons learned from 25 years of research at the MADE site., *Ground Water*, *49*(5), 649–62, doi:10.1111/j.1745-6584.2010.00753.x.
Zinn, B. (2003), When good statistical models of aquifer heterogeneity go bad: A comparison of flow, dispersion, and mass transfer in connected and multivariate Gaussian hydraulic conductivity fields, *Water Resour. Res.*, *39*(3), 1051, doi:10.1029/2001WR001146.

Erratum

In the second paragraph of the Introduction, the "Zhang et al." citation is incorrect: "Although nonlocal theories can often provide a better match [Zhang et al., 2011], ADE was found to capture [...]" The correct citation is Zheng et al., 2011. This version may be considered the authoritative version of record.

Available online at www.sciencedirect.com

ScienceDirect

Energy Procedia 00 (2017) 000–000

Energy Procedia

www.elsevier.com/locate/procedia

13th International Conference on Greenhouse Gas Control Technologies, GHGT-13, 14-18 November 2016, Lausanne, Switzerland

Injectivity Evaluation for Offshore CO_2 Sequestration in Marine Sediments

Zhenxue Dai[a*], Ye Zhang[b], Philip Staffer[a], Ting Xiao[c], Minkan Zhang[b], William Ampomah[d], Changbing Yang[e], Youqin Zhou[e], Mei Ding[a], Richard Middleton[a], Mohamad Reza Soltanian[f] and Jeffrey M. Bielicki[g]

[a]*Earth and Environmental Sciences Division, Los Alamos National Laboratory, Los Alamos, NM 87545, USA*
[b]*Departmen of Geology and Geophysics, University of Wyoming, Laramie, Wyoming, USA*
[c]*Energy and Geoscience Institute, The University of Utah, Salt Lake City, UT 84108, USA*
[d]*Petroleum Recovery Research Center, New Mexico Tech, Socorro, NM 87801,USA*
[e]*Bureau of Economic Geology, The University of Texas at Austin, TX 78713, USA*
[f] *School of Earth Sciences, The Ohio State University, Columbus, OH 43210, USA*
[g]*Department of Civil, Environmental, and Geodetic Engineering, The Ohio State University, Columbus, OH 43210, USA*

Abstract

Global and regional climate change caused by greenhouse gases emissions has stimulated interest in developing various technologies (such as carbon dioxide (CO_2) geologic sequestration in brine reservoirs) to reduce the concentrations of CO_2 in the atmosphere. This study develops a statistical framework to identify gravitational CO_2 trapping processes and to quantitatively evaluate both CO_2 injectivity (or storage capacity) and leakage potential from marine sediments which exhibit heterogeneous permeability and variable thicknesses. We focus on sets of geostatistically-based heterogeneous models populated with fluid flow parameters from several reservoir sites in the U.S. Gulf of Mexico (GOM). A computationally efficient uncertainty quantification study was conducted with results suggesting that permeability heterogeneity and anisotropy, seawater depth, and sediment thickness can all significantly impact CO_2 flow and trapping. Large permeability/porosity heterogeneity can enhance gravitational, capillary, and dissolution trapping, which acts to deter CO_2 upward migration and subsequent leakage onto the seafloor. When log permeability variance is 5, self-sealing with heterogeneity-enhanced gravitation trapping can be achieved even when water depth is 1.2 km. This extends the previously identified self-sealing condition that water depth be greater than 2.7 km. Our results have yielded valuable insight into the conditions under which safe storage of CO_2 can be achieved in offshore environments. The developed statistical framework is general and can be adapted to study other offshore sites worldwide.

Peer-review under responsibility of the organizing committee of GHGT-13.

Keywords: gravitational trapping; offshore sediment; CO_2 sequestration; injectivity; leakage potential; sediment heterogeneity; uncertainty quantification; Gulf of Mexico.

1876-6102
Peer-review under responsibility of the organizing committee of GHGT-13.

1. Introduction

Global and regional climate change caused by greenhouse gas emissions has stimulated interest in developing various technologies to reduce the concentrations of carbon dioxide in the atmosphere [1-3]. Several approaches have been proposed for long-term storage and disposal of captured anthropogenic CO_2, including injection into geologic formations (such as into depleted oil and gas reservoirs [4-8], coalbeds [9], and saline aquifers [10-12]), deep ocean storage [13-14], and storage via chemical transformations (e.g., to make fertilizer, dry ice, and plastics, and even to carbonate soda [15-16]). Compared to geologic and ocean storage, however, the market demand for chemical transformations of the captured CO_2 is relatively limited – at around 200 million tons per year – or about 175 times smaller than the amount of CO_2 emitted globally from energy use in 2013 [15]. This study proposes CO_2 offshore storage in marine sediments, an option currently being explored [17-19]. It combines the benefits of geologic storage, deep-oceanic storage, and chemical transformation, and adds huge capacity to onshore geological carbon sequestration.

Studies suggest that the offshore storage can reduce monitoring expenses and lead to enhanced storage security [18-19]. By injecting CO_2 into sediments beneath the seafloor under suitable temperature and pressure conditions, CO_2 could be trapped through 'self-sealing' gravitational or hydrate-formation mechanisms [19]. Under gravitational trapping, an impermeable caprock above the CO_2 reservoir to prevent upward fluid migration is no longer required; when hydrates are formed, CO_2 becomes immobilized. Moreover, offshore locations are away from population centers. As a result, such operations avoid the perception of storage beneath a populated area, reduce the difficulty of establishing surface and mineral rights at candidate sites, and decrease the risk of contaminating underground sources of drinking water [20-21]. Notwithstanding high capital costs (e.g. drilling rigs), the overall economics of offshore storage may be more favorable than onshore storage. For example, storage can be combined with enhanced oil recovery (EOR) in depleted off-shore oil and gas fields, which have infrastructure in place including injection wells and pipelines. In many offshore settings, due to the great reservoir depths, high formation pressure is expected even after primary and secondary recoveries, thus ensuring the miscibility requirement for EOR [22-25]. However, off-shore storage has its own challenges. Based on experience gained in producing off-shore reservoirs, two main challenges have been identified: (1) storage security is compromised when the emplaced CO_2 in sub-seafloor sediments leaks into the overlying water column; (2) storage capacity and injectivity may not be guaranteed at all off-shore locations, because suitable reservoirs with sufficient areal extent, thickness, porosity, and permeability are needed.

Several offshore carbon geologic sequestration projects have been conducted, including the European Union's CO_2ReMoVe project [26], Norway's SUCCESS [27], the United Kingdom's QICS [28-29], and the Australian Government's National Low Emission Coal Initiative (NLECI) and National CO_2 Infrastructure Plan (NCIP) [30]. The ongoing Sleipner project has been injecting supercritical CO_2 into the Utsira Formation which lies 1 km beneath the seafloor in the central North Sea. Since 1996, about 15 Mt of CO_2 has been sequestered in this semi-consolidated sandstone formation overlain by low permeability caprocks [28]. These studies are located mainly in the shallow seas (seawater depth less than 1 km) and the injected CO_2 could not be trapped through 'self-sealing' storage [19].

Permeability in sedimentary deposits always exhibits spatial heterogeneity and anisotropy that reflect the original depositional and also post-depositional processes. Experimental, numerical, and field studies on geological storage suggest that reservoir permeability heterogeneity can enhance capillary and dissolution trapping while potentially helping to deter CO_2 migration and leakage [31-35]. Simulation results also suggest that models incorporating permeability heterogeneity can more accurately assess the various CO_2 trapping mechanisms [36-38]. While CO_2 'self-sealing' storage can be very attractive, more detailed studies of CO_2 interaction with formation water and heterogeneous sediments under variable temperature and pressure conditions are needed for understanding mechanisms of CO_2 trapping processes in the deep-sea sediments and for quantitatively evaluating the CO_2 injectivity and possible leakage rates to sea.

This study is to develop a statistical framework for CO_2 accounting in the deep-sea sediments and quantifying CO_2 trapped in different processes such as solubility trapping, capillary trapping, heterogeneity trapping, gravitational and hydrate-formation trapping. The statistical framework starts from characterizing marine sediment heterogeneity and defining the associated independent parameters (which are statistically independent from output variables, but have a large impact on modeling results). The independent parameters can be classified into: sea depth, marine sediment thickness, permeability mean, variance and integral scale, and porosity. In most of the offshore sites such as in the sites of the Gulf of Mexico (GOM), the exact values of the independent parameters are not well-known, but we may obtain enough information to characterize or define the uncertainty distributions of these independent parameters. These distributions are used to sample the uncertain parameters and conduct geostatistical-based Monte Carlo (MC) simulations to quantitative evaluate both the storage capacity and leakage probability of marine sediments exhibiting variable permeability, variance, porosity and thicknesses. We focus on a set of synthetic models with reservoir fluid flow characteristics selected based on four sites in the GOM basin where sediments with sufficient thickness and permeability exist (Figure 1). As a result of historical exploration for development of petroleum and other resources, extensive subsurface characterization data exist in these sites, thus uncertainty in reservoir parameters can also be relatively well constrained [39-42]. Within a computationally efficient statistical framework, this study also aims to assess the uncertainty in the estimated storage capacity and leakage probability for the synthetic reservoirs. Results then yield insights into the conditions under which safe and permanent storage of CO_2 can be achieved in offshore environments. In the following sections, the characteristics of the four GOM sites are first summarized, followed by a description of the uncertainty methodology used to evaluate CO_2 storage and leakage into the sea.

2. Characteristics of Four GOM Sites

In the GOM basin, several investigations into marine sediments and reservoir properties (e.g. permeability, porosity, and temperature) at four sites have been conducted [43]. Figure 1 shows the locations of the four sites: Alminos Canyon, Bullwinkle, Ursa Basin, and Eugene Island. In the Alminos Canyon site, the unconsolidated and consolidated Oligocene sediments, mainly consisting of fine grained sand and immature Frio sand, have a high porosity (from 0.28 to 0.34) and a large permeability (from 100 to 3000 mD) [44-45]. In the Bullwinkle site, sediments mainly contain interconnected sheet and channel sands. The sheet sand has an average porosity and permeability of 0.33 and 2400 mD, respectively. In some individual sand layers porosities can reach 0.35 and permeability is up to 3300 mD [46-47].

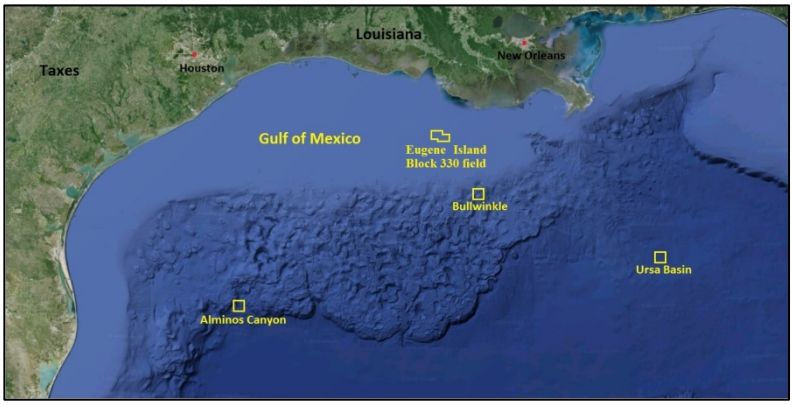

Fig. 1. The location of the four offshore sites in the Gulf of Mexico.

In the Ursa Basin, in-situ permeability of Ursa Siltstone is estimated at around 1 mD. The vertical permeabilities in this site were measured using the transient pulse decay technique [48], which are about one to two orders of magnitude less than the corresponding horizontal permeabilities. Long et al.[44] studied the consolidation and fluid overpressure near the seafloor in the Ursa Basin. There, porosity is up to 42% (a few samples even up to 80%) and the permeability is approximately 5 mD. More petrophysical properties of turbidite sand in this site can be found in reports [49-50]. In the Eugene Island site, offshore Louisiana, thick sequence of shale was covered by increasingly sand-rich sediments. Laboratory determination of in-situ permeability on core samples yield a mixture permeability ranging from 0.2 to 8000 mD and the porosity ranges from 0.16 to 0.35 [51-53]. Based on measured porosities in these four sites, permeability-porosity relationships have also been developed as:

$$ø = a + b\ log_{10}k, \tag{1}$$

where $ø$ is porosity and k is permeability; a and b are also site-specific constants. By using the permeability and porosity data collected the four sites (Figure 2), we estimated the two constants: a = 0.145 and b = 0.062.

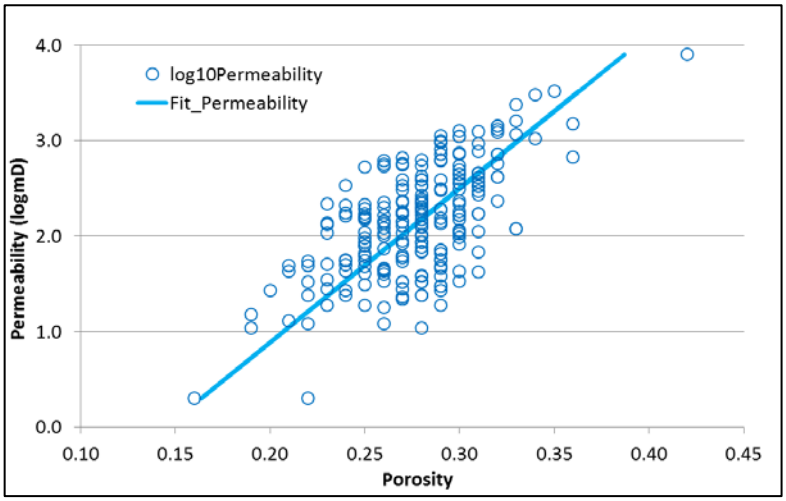

Figure 2: Measured permeability/porosity and the fitted curve for permeability/porosity distributions in the Gulf of Mexico

The geothermal features of northwestern GOM continental slope were studied by Milkov and Sassen [46], where approximation relations between depth-temperature and depth-geothermal gradient are provided. Both sea bottom temperature (T, ºC) and geothermal gradient (G, ºC/km) are correlated with seawater depth. By using equations derived by Milkov and Sassen [46], we can calculate temperatures at the sea bottom and in the sediments based on the sampled seawater depth. With the parameter information available for the four Gulf sites, we summarize the ranges and distributions of the uncertain parameters for simulating the heterogeneity of the marine sediments and shallow reservoirs in Table 1. The vertical spatial integral scale of log permeability is obtained from logging data, while the statistical anisotropy between horizontal and vertical integral scales is assumed to be 100. The anisotropy of horizontal and vertical permeability is varied to quantify the impact of the anisotropy factor on the CO_2 leakage from the sediments to the sea bottom. Having been limited by the available data, we assume that the ranges of the log permeability variance and horizontal integral scale are (0.01, 4) and (0.5, 5), respectively. The relative permeability functions for CO_2-brine multiphase flow simulations were calculated on the basis of the van Genutchten model to define the related coefficients [54-56]. Table 1 also lists the ranges of seawater depth, CO_2 injection rate, sea-bottom temperature, and geothermal gradient. The latter two parameters are correlated to seawater depth.

Table 1. Summarized uncertain parameters (independent parameters) and distributions.

Uncertain parameters		Min.	Max.	Base case	**Distribution**
Sediment Property	Sediment thickness (km)	0.005	0.9	500	Uniform
	Mean permeability (D)	0.001	8	1.0	Log uniform
	Anisotropy factor	0.01	0.5	0.1	Uniform
	Log permeability variance	0.01	4.0	0.0	Uniform
	Integral scale (km)	0.5	5.0	1.0	Uniform
	Porosity	0.1	0.42	0.2	Correlated to perm
Physical Parameter	Sea depth (km)	0.1	4.4	2.5	Uniform
	CO_2 injection rate (kg/s)	0.002	2.0	0.3	Uniform
	Sea-bottom temperature (^oC)	2	20	2	Correlated to depth
	Temperature grad (^oC/km)	5	50	20	Correlated to depth

3. Monte Carlo Simulations of offshore CO2 sequestration

Given uncertainty of several key reservoir parameters, it is essential to conduct a set of Monte Carlo (MC) simulations to understand the uncertainty of the key properties impacting CO_2 storage/leakage in the marine sediments in the GOM. The uncertainty parameters (as listed in Table 1) considered in this work are: reservoir thickness, permeability, permeability anisotropy (horizontal to vertical permeability ratio), log permeability variance and integral scale, sea depth, and CO_2 injection rate. The sea depth is varied from 100 m to 4.4 km. A joint probability density function (PDF) is thus developed between water depth and the bottom water temperature and geothermal gradient based on the equations of Milkov and Sassen [46]. The seawater density is around 1.03 g/cm3 in the GOM. Other uncertainty factors, such as background fluid flow, will be considered and discussed in future work. Based on the MC simulation results, we conduct correlation analysis with PSUADE [57]. The computed correlation matrix of the sampled parameters is shown in Figure 3, in which permeability (rKmean) and porosity (rPor) are correlated, and pressure (Ptop) and temperature (Ttop) at the top of the sediments are correlated with seawater depth (Depth). Other parameters are independent to each other. Figure 4 shows the correlations between the sampled parameters and the output variables.

These MC simulations also incorporate permeability and porosity heterogeneity into the model, and results are analyzed to identify the conditions (i.e., water depth, sediment thickness, mean permeability and porosity, log permeability variance and integral scale, permeability anisotropy factor, and injection rate) under which the injected CO_2 can be trapped by gravitational trapping.

4. Global sensitivity analysis

A global sensitivity analysis technique, based on multivariate adaptive regression spline (MARS) with normalized indices, was applied to investigating sensitivities of the output variable (CO_2 leakage) to variation of the uncertain input parameters [57]. The MARS technique is based on computing a variance of conditional expectation (*VCE*) of the output variable.

The sensitivity of output variables to a number of input parameters is quantified and ranked from 0 to 100 to represent the relative importance of each input parameter to the prediction of output variables. Using the computationally efficient MARS response surface functions, the suite of *VCE* is then evaluated to generate prediction envelop of output variables given the uncertain input parameters [57-59].

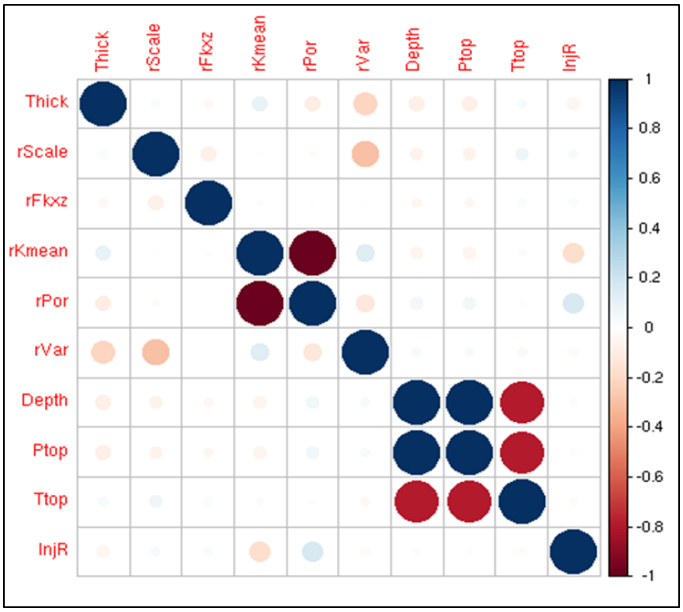

Fig. 3. The correlation matrix of among sampled parameters.

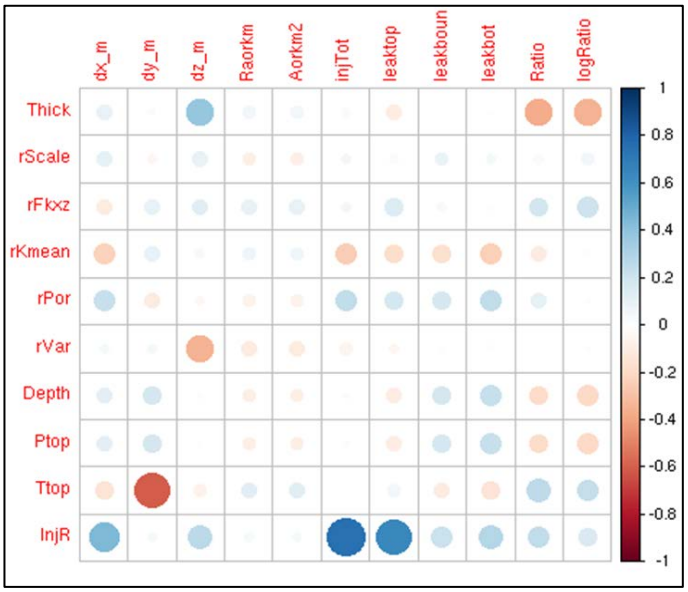

Fig. 4. The correlation matrix between the sampled parameters and the output variables.

The sensitivity analysis suggests that, for predicting CO_2 leakage out of the sediments into the sea in the GOM, permeability anisotropy factor, injection rate, water depth, sediment thickness, permeability variance, mean permeability, and seafloor temperature are the most sensitive parameters (Figure 5), which are also ranked from the most sensitive to less sensitive. Although porosity is positively correlated with horizontal permeability, CO_2 leakage is not as sensitive to this parameter compared to mean horizontal permeability. Interestingly, for the assumed statistical anisotropy ratio (100), log permeability horizontal integral scale has the least impact on CO_2 leakage.

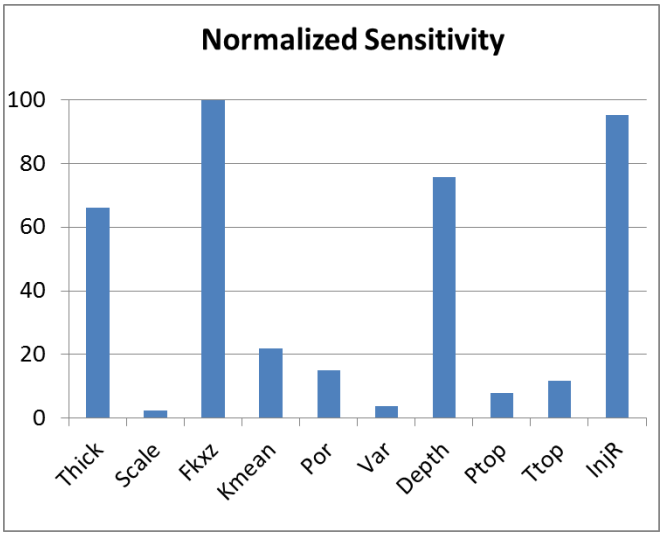

Fig. 5. The computed sensitivity index of the output variable (percent CO_2 leakage) to uncertain input parameter varied in the global sensitivity analysis.

5. Gravitational and heterogeneity trapping

A base case cross sectional model (thickness = 500 m, horizontal length = 5 km, and lateral length = 1m) was studied to obtain an initial understanding of CO_2 flow and trapping in marine sediments. The sediments are assumed to be heterogeneous with a horizontal mean permeability of 1D and a variance of 1. The heterogeneous horizontal permeability distributions are generated with Sequential Gaussian Simulation with a horizontal log permeability integral scale of 1.0 km. Porosity in this model is computed from horizontal permeability with Equation (1). The remaining parameters are listed in Table 1. The top of the reservoir model lies at the seafloor. A uniform CO_2 injection rate (0.3 kg/s) is assigned at the bottom-center of the model for 10 years. After injection ceases, CO_2 migration is simulated until the total simulation time 200 years.

Figure 6 shows simulated permeability field and the liquid-phase CO_2 pressure distribution at 20 years. The combined effect of reservoir fluid pressure and temperature causes the injected liquid CO_2 to have a density slightly greater than that of seawater (1.03 g/cm3) at the center of the CO_2 plume and near the topmost layers of the model (Figure 7). Near the bottom layers, due to increasing temperature with depth (base case geothermal gradient = 20 ^oC/km), the injected CO_2 has a density close to that of seawater. When CO_2 moves upwards by pressure difference, it becomes denser and confined by the higher-density CO_2 at the top layers. Thus, negative buoyancy of liquid CO_2 at the topmost layers prevents the liquid-phase plume from leaking onto the seafloor and all of the injected CO_2 sinks to the bottom layers. In this case, liquid CO_2 plume does not reach the upper boundary: at the end of 200 years, computed CO_2 leakage from the top of the sediments is 0 and the injected CO_2 is considered to be successfully trapped in the marine sediments. Results suggest that permeability heterogeneity, in particular, the presence of low-

permeability layers, can additionally enhance storage security by deterring upwards migration. The model was further run to 1000 years and the liquid CO_2 plume has reached a steady state after 200 years, i.e., plume shape and size do not change anymore. For this case, CO_2 is safely sequestered by both gravitation and heterogeneity.

To refine the understanding of the key parameters and their potential interactions that can impact gravitational trapping, three additional sets of MC simulations (300 realizations total) were conducted sampling only sediment thickness, using an injection rate of 0.2, 0.02, and 0.002 kg/s, respectively. The other parameters are the same as those of the base case. The relative CO_2 leakage rate (normalized by by the injection rates) is computed and plotted against sediment thicknesses, for the increasing injection rate (Figure 8). When injection rate is 0.2 kg/s, gravitational trapping is accomplished, approximately, at a sediment thickness > 400 m; when injection rate is 0.02 kg/s, sediment thickness > 210 m; and when injection rate is 0.002 kg/s, sediment thickness > 90 m. Clearly, with all other conditions being equal, safe storage in these settings is influenced by both the injection rate and the thickness of the sediment. With increasing injection rate, thicker sediment is required to help deter CO_2 upward migration and leakage onto the seafloor.

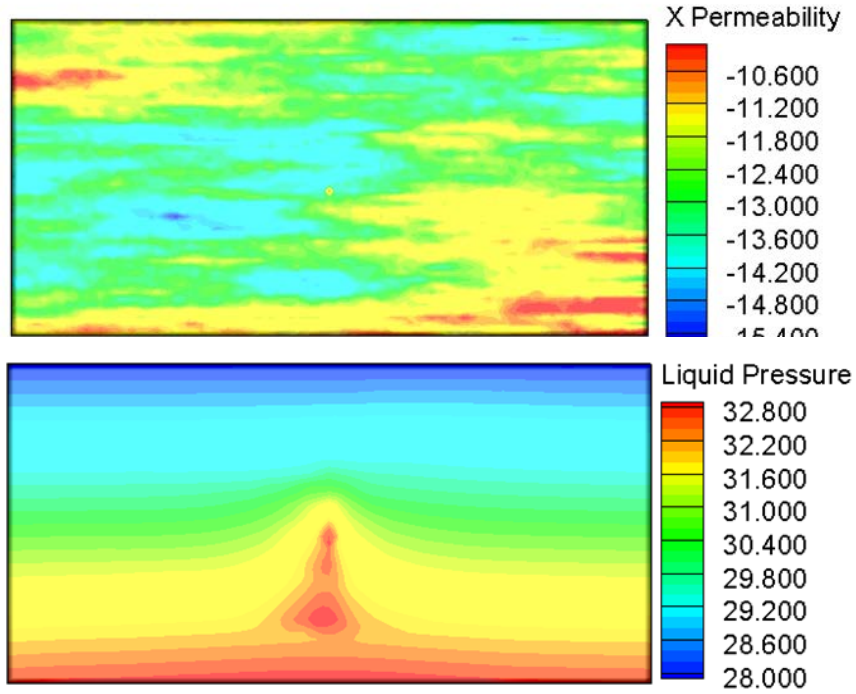

Fig. 6. Horizontal permeability (logm2) field (upper) and the simulated CO_2 liquid pressure (MPa) (lower), in a vertical cross section (from MC run 22).

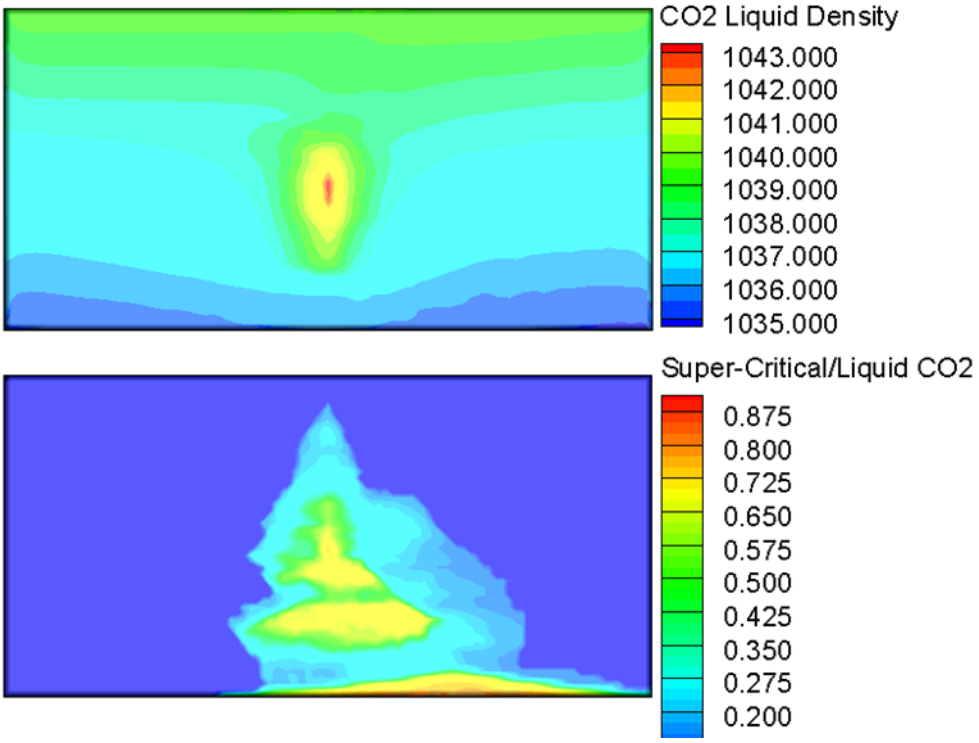

Fig. 7. The simulated CO_2 liquid density (upper) and CO_2 saturation (lower) in a vertical cross section (from MC run 22).

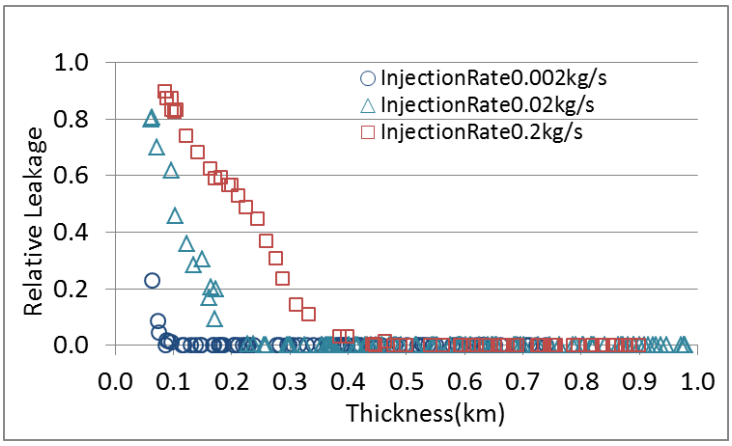

Fig. 8. The impact of the injection rates and the sediment thickness on the relative leakage to the seafloor

6. Summary and discussion

This study develops a statistical framework to simulate gravitational CO_2 trapping processes and to quantitatively evaluate both CO_2 injectivity (or storage capacity) and its leakage potential from marine sediments which exhibit heterogeneous permeability and variable thicknesses. The conducted numerical investigations indicate that the injected CO_2 can be gravitationally trapped in offshore marine sediments of the GOM with suitable temperature and pressures at the seafloors.

A selected suite of uncertain reservoir and environmental input parameters is defined, with results suggesting that safe storage could be accommodated in deep water GOM sediments with large thickness, high mean permeability and porosity, and with relatively low injection rate. Results also suggest that permeability heterogeneity with the presence of low-permeability layers, in particular, can additionally enhance storage security by deterring upwards migration. Our results have yielded valuable insights into the conditions under which safe and permanent storage of CO_2 can be achieved in offshore sediments. The developed uncertainty quantification framework is general and can be adapted to studying other offshore sites worldwide.

This study did not evaluate the impact of other mechanisms (such as geomechanical stress and deformation due to injection) and uncertainty factors (such as background fluid flow and geochemical self-sealing) on CO_2 injectivity (or storage capacity) and its leakage potential from marine sediments. The effects and their interaction with CO_2 fluid flow and trapping processes will be considered and discussed in future work.

Acknowledgements

Funding for this work is provided by the US-China Clean Energy Research Center, Advanced Coal Technology Consortium directed by West Virginia University. Additional funding was contributed through the U.S. Department of Energy's (DOE), National Energy Technology Laboratory (NETL) through the Southwest Partnership on Carbon Sequestration (SWP) under Award No. DE-FC26-05NT42591. We gratefully acknowledge Drs. Rajesh Pawar and Hari Viswanathan for providing constructive comments on the MC simulations.

Disclaimer

References

[1] Canadell, J. G., E. D. Schulze, Global potential of biospheric carbon management for climate mitigation, *Nat. Commun.* 2014, 5:5282.

[2] Zou, Y., C. Yang, D. Wu, C. Yan, M. Zeng, Y. Lan, Z. Dai, Probabilistic assessment of shale gas production and water demand at Xiuwu Basin in China, *Applied Energy* 2016, 180, 185–195.

[3] Bachu, S. Screening and ranking of sedimentary basins for sequestration of CO_2 in geological media in response to climate change, *Environ. Geol.* 2003, 44, 277-289.

[4] Yang, C., Z. Dai, K. Romanak, S. Hovorka, R. Trevino, Inverse Modeling of Water-Rock-CO_2 Batch Experiments: Implications for Potential Impacts on Groundwater Resources at Carbon Sequestration Sites, *Environ. Sci. Technol.* 2014, 48, 2798–2806.
[5] Shaffer, G., Long-term effectiveness and consequences of carbon dioxide sequestration, *Nat. Geoscience* 2010, 3, 464 – 467.
[6] Bacon, D., N. Qafoku, Z. Dai, E. Keating, C. Brown, Modeling the Impact of Carbon Dioxide Leakage into an Unconfined, Oxidizing Carbonate Aquifer, *Int. J. of Greenhouse Gas Con.* 2016, 44, 290-299.
[7] Dai, Z., R. Middleton, H. Viswanathan, J. Fessenden-Rahn, J. Bauman, R. Pawar, S. Lee and B. McPherson, An integrated framework for optimizing CO_2 sequestration and enhanced oil recovery, *Environ. Sci. Technol. Lett*. 2014, 1, 49-54.
[8] Bacon, D.H., Z. Dai, L. Zheng, Geochemical impacts of carbon dioxide, brine, trace metal and organic leakage into an unconfined, oxidizing limestone aquifer, *Energy Procedia* 2014, 63, 4684-4707.
[9] Gale, J., and P. Freund, Coal - Bed Methane Enhancement with CO_2 Sequestration Worldwide Potential, *Environ. Geosci*. 2001, 8(3), 210-217.
[10] Nordbotten, J., M. Celia, and S. Bachu, Injection and storage of CO_2 in deep saline aquifers: Analytical solution for CO_2 plume evolution during injection, *Transp. Porous Media*. 2005, 58(3), 339-360.
[11] Dai, Z. et al., Pre-site characterization risk analysis for commercial-scale carbon sequestration, *Environ. Sci. Technol.* 2014, 48, 3908−3915.
[12] Godec, M., V.A. Kuusktaa, T. V. Leeuwen, L.S. Melzer, N. Wildgust, CO_2 storage in depleted oil fields: The worldwide potential for carbon dioxide enhanced oil recovery, *Energy Procedia* 2011, 4, 2162-2169.
[13] Haugan, P. M., H. Drange, Sequestration of CO2 in the deep ocean by shallow injection, *Nature* 1992, 357, 318–320.
[14] Christensen, J.R., E.H. Stenby, A. Skauge, Review of WAG Field Experience, *SPE Reservoir Eval. & Eng*. 2001, April, 97–106.
[15] O'Conner, W., D. Dahlin, P. Turner, and R. Walters, Carbon dioxide sequestration by ex-situ mineral carbonation, Office of Fossil Energy, US DOE 1999, DOE/ARC-1999-009, OSTI 875354, p15.
[16] Lackner, K., Carbonate chemistry for sequestering fossil carbon, *Annu. Rev. Energy Environ.* 2002, 27: 193-232.
[17] Gan, W. and C. Frohlich, Gas injection may have triggered earthquakes in the Cogdell oil field, Texas, *Proc. Natl. Acad. Sci. U.S.A.* 2013, 110, 18786-18791.
[18] Schrag, D. P. Storage of Carbon Dioxide in Offshore Sediments. *Science* 2009, 325, 1658-1659.
[19] House, K. Z., D. P. Schrag, C. F. Harvey, and K. S. Lackner, Permanent carbon dioxide storage in deep-sea sediments., *Proc. Natl. Acad. Sci. U. S. A.* 2006, 103, 12291–12295.
[20] Dai, Z., E. Keating, D. Bacon, H. Viswanathan, P. Stauffer, A. Jordan, R. Pawar, Probabilistic evaluation of shallow groundwater resources at a hypothetical carbon sequestration site, *Sci. Rep*. 2014, 4, 4006.
[21] Bielicki, J., Pollak, M., Deng, H., Wilson, E., Fitts, J., and Peters, C. The Leakage Risk Monetization Model for Geologic CO2 Storage. *Environ. Sci. Technol*. 2016. 50(10), 4923-4931.
[22] Sobers, L., M. Blunt, and T. LaForce, Design of Simultaneous Enhanced Oil Recovery and Carbon Dioxide Storage With Potential Application to Offshore Trinidad, *SPE J*.2013, 18(2), 345-354.
[23] Eccles, J.K. and L. Pratson, Economic evaluation of offshore storage potential in the US Exclusive Economic Zone, *Greenhouse Gas Sci Technol.* 2013, 3:84–95.
[24] Bachu, S. Identification of oil reservoirs suitable for CO_2-EOR and CO_2 storage (CCUS) using reserves databases, with application to Alberta, Canada, *Int. J. of Greenh. Gas Con.* 2016, 44, 152–165.
[25] Dai, Z., H. Viswanathan, R. Middleton, F. Pan, W. Ampomah, C. Yang, W. Jia, T. Xiao, S.-Y. Lee, B. McPherson, CO2 Accounting and Risk Analysis for CO_2 Sequestration at Enhanced Oil Recovery Sites, *Environ. Sci. Technol.* 2016, 50, 7546-7554.
[26] Wildenborg, T., M. Bentham, A. Chadwick, P. David, J-P. Deflandree, M. Dillen, H. Groenenberg, K. Kirk, Y. L. Gallo, Large-scale CO_2 injection demos for the development of monitoring and verification technology and guidelines (CO_2 ReMoVe), *Energy Procedia* 2009, 1(1), 2367-2374.
[27] Aker, E., T. Bjørnaråa, A. Braathen, Ø. Brandvoll, H. Dahle, J. M. Nordbotten, P. Aagaard, H. Hellevang, B. L. Alemu, V.T.H. Pham, H. Johansen, M. Wangen, A. Nøttvedt, I. Aavatsmark, T. Johannessen, D. Durandh, SUCCESS: SUbsurface CO_2 storage–Critical elements and superior strategy, *Energy Procedia* 2011, 4, 6117-6124.
[28] Taylor, P., A. Lichtschlag, M. Toberman, M. D. J. Sayer, A. Reynolds, T. Sato, and H. Stahl, Impact and recovery of pH in marine sediments subject to a temporary carbon dioxide leak, *Int. J. Greenh. Gas Con.*, 2015, 38, 93–101.
[29] Taylor, P., A. Lichtschlag, M. Toberman, M. D. J. Sayer, A. Reynolds, T. Sato, and H. Stahl, Impact and recovery of pH in marine sediments subject to a temporary carbon dioxide leak, *Int. J. Greenh. Gas Con.*, 2015, 38, 93–101.
[30] Borissova, I., Kennard, J., Lech, M., Wang, L., Johnston, S., Lewis, C. and Southby C., Integrated Approach to CO2 Storage Assessment in the Offshore South Perth Basin, Australia. *Energy Procedia* 2013, 37, 4872-4878.
[31] Deng, H., P. Stauffer, Z. Dai, Z. Jiao, R. Surdam, Simulation of industrial-scale CO_2 storage: Multi-scale heterogeneity and its impacts on storage capacity, injectivity and leakage, *Int. J. Greenh. Gas Con.* 2012, 10, 397–418.
[32] Ampomah, W., R.S. Balch, R.B. Grigg, B. McPherson, R.A. Will, S. Lee, Z. Dai, F. Pan, Co-optimization of CO_2-EOR and storage processes in mature oil reservoirs, *Greenhouse Gas Sci Technol*. 2016, 00:1–15, DOI: 10.1002/ghg.
[33] Dai, Z., H. Viswanathan, J. Fessenden-Rahn, R. Middleton, F. Pan, W. Jia, S-Y Lee, B. McPherson, W. Ampomah, R. Grigg, Uncertainty quantification for CO_2 sequestration and enhanced oil recovery, *Energy Procedia* 2014, 63, 7685–7693.
[34] Pan, F., B. J. McPherson, Z. Dai, W. Jia, S. Lee, W. Ampomah, H. Viswanathan, R. Esser, Uncertainty Analysis of Carbon Sequestration in an Active CO_2-EOR Field, *Int. J.of Greenh. Gas Con.* 2016, 51, 18-28.
[35] Xiao, T., McPherson, B., Pan, F., Esser, R., Jia, W., Bordelon, A., & Bacon, D. Potential chemical impacts of CO_2 leakage on underground source of drinking water assessed by quantitative risk analysis. *Int. J.of Greenh. Gas Con.* 2016, 50, 305-316.

[36] Ampomah, W., R.S. Balch, M. Cather, D. Rose-Coss, Z. Dai, J. Heath,T. Dewers, P. Mozley, Evaluation of CO_2 Storage Mechanisms in CO_2 Enhanced Oil Recovery Sites: Application to Morrow Sandstone Reservoir, *Energy and Fuels* 2016, DOI: 10.1021/acs.energyfuels.6b01888.

[37] Levine, J., J. Matter, D. Goldberg, A. Cook, and K. S. Lackner, Gravitational trapping of carbon dioxide in deep ocean sediments: Permeability, buoyancy, and geomechanical analysis, *Geophys. Res. Lett*. 2007, 34, L24703, 1-5.

[38] Dai, Z., P. H. Stauffer, J. W. Carey, R. S. Middleton, Z. Lu, J. F. Jacobs, K. Hnottavange-Telleen, L. Spangle, Pre-site characterization risk analysis for commercial-scale carbon sequestration, *Environ. Sci. Technol*. 2014, 48, 3908−3915.

[39] Dai, Z., H. Viswanathan, R. Middleton, F. Pan, W. Ampomah, C. Yang, W. Jia, T. Xiao, S.-Y. Lee, B. McPherson, CO_2 Accounting and Risk Analysis for CO_2 Sequestration at Enhanced Oil Recovery Sites, *Environ. Sci. Technol.* 2016, 50, 7546-7554.

[40] Bielicki, J., Peters, C., Fitts, J., Wilson, E. An Examination of Geologic Carbon Sequestration Policies in the Context of Leakage Potential, *Int. J. of Greenh. Gas Con.* 2015, 37, 61-75.

[41] Li, S., Y. Zhang, and X. Zhang, A study of conceptual model uncertainty in large-scale CO_2 storage simulation, *Water Resour. Res*. 2011, 47(5), W05534 1–23.

[42] Gershenzon, N. I., R. W. Ritzi, D. F. Dominic, M. Soltanian, E. Mehnert, and R. T. Okwen, Influence of small-scale fluvial architecture on CO_2 trapping processes in deep brine reservoirs, *Water Resour. Res*. 2015, 51, 8240–8256.

[43] Binh, N. T. T., T. Tokunaga, T. Nakamura, K. Kozumi, M. Nakajima, M. Kubota, H. Kameya, and M. Taniue, Physical properties of the shallow sediments in late Pleistocene formations, Ursa Basin, Gulf of Mexico, and their implications for generation and preservation of shallow overpressures, *Mar. Pet. Geol*. 2009, 26(4), 474–486.

[44] Li, Y., and S. Jiang, Boron concentration and isotopic constraints on processes affecting the chemistry of interstitial water in normal-and over-pressured basins, Gulf of Mexico, *Mar. Geol*. 2010, 275(1-4): 230-243.

[45] Long, H., P. B. Flemings, J. T. Germaine, and D. M. Saffer, Consolidation and overpressure near the seafloor in the Ursa Basin, Deepwater Gulf of Mexico, *Earth Planet. Sci. Lett*. 2011, 305(1-2), 11–20.

[46] Milkov, A. V., and R. Sassen, Estimate of gas hydrate resource, northwestern Gulf of Mexico continental slope, *Mar. Geol*.2001, 179(1-2), 71–83.

[47] Reece, J. S., P. B. Flemings, B. Dugan, H. Long, and J. T. Germaine, Permeability-porosity relationships of shallow mudstones in the Ursa Basin, northern deepwater Gulf of Mexico, *J. Geophys. Res. Solid Earth* 2012, 117(12), 1–14.

[48] Boswell, R., D. Shelander, M. Lee, T. Latham, T. Collett, G. Guerin, G. Moridis, M. Reagan, and D. Goldberg , Occurrence of gas hydrate in Oligocene Frio sand : Alaminos Canyon Block 818 : Northern Gulf of Mexico, *Mar. Pet. Geol*. 2009, 26(8), 1499–1512.

[49] Steinman, C., R. Deshpande, and J. Farley, Stress-dependent permeability in unconsolidated sand reservoirs, *Offshore* 2000, 28(1), 109–119.

[50] Comisky, J., Petrophysical analysis and geologic model for the Bullwinkle J Sands with implications for time-lapse reservoir monitoring, Green Canyon block 65, Offshore Louisiana, Master Thesis, Penn State University, 2002, p149.

[51] Aniekwena, A. U., D. a Mcvay, W. M. Ahr, J. S. Watkins, and a Texas, SPE 84051 Integrated Characterization of the Thin-Bedded 8 Reservoir , Green Canyon 18 , Gulf of Mexico, (May 1987), 2003.

[52] Ostermeier, R., Stressed Oil Permeability of Deepwater Gulf of Mexico Turbidite Sands: Measurements and Theory, *SPE Form. Eval*. 1996, 11(4), 229–235.

[53] Yang, Y., and A. C. Aplin (2007), Permeability and petrophysical properties of 30 natural mudstones, *J. Geophys. Res. Solid Earth* 2007, 112(3), B03206, doi:10.1029/2005JB004243.

[54] Pruess, K. and J. Garcia. Multiphase flow dynamics during CO_2disposal into saline aquifers. *Environ. Geol.* 2002, 42, 282-295.

[55] Dai, Z., J. Samper, A. Wolfsberg, and D. Levitt, Identification of relative conductivity models for water flow and solute transport in unsaturated compacted bentonite, *Physics and Chem. of the Earth* 2008, 33, S177-S185.

[56] Ampomah, W., R.S. Balch, R.B. Grigg, R. Will, S.Y., Lee, Z. Dai, Performance of CO_2-EOR and Storage Processes under Uncertainty, *Society of Petroleum Engineering* 2016, SPE-180084-MS.

[57] Tong, C., PSUADE User's Manual (Version 1.2.0), LLNL-SM-407882, Lawrence Livermore National Laboratory, Livermore, CA 94551-0808, May 2011.

[58] Dai, Z., A. Wolfsberg, Z. Lu, and R. Ritzi, Representing Aquifer Architecture in Macrodispersivity Models with an Analytical Solution of the Transition Probability Matrix, *Geophys. Res. Lett*. 2007, 34, L20406.

[59] Ampomah, W., R. S. Balch, R. B. Grigg, Z. Dai and F. Pan, Compositional simulation of CO_2 storage capacity in depleted oil reservoirs. Carbon Management Technology Conference, 2015, ID: CMTC-439476-MS, doi: http://dx.doi.org/10.7122/439476-MS.

[American Journal of Science, Vol. 316, May, 2016, P. 437–469, DOI 10.2475/05.2016.02]

KINETIC RATE LAWS INVARIANT TO SCALING THE MINERAL FORMULA UNIT

PETER C. LICHTNER

OFM Research Southwest, 29 Bosque Azul, Santa Fe, New Mexico 87507

ABSTRACT. A modified form of the kinetic rate law for mineral dissolution and precipitation is proposed that is invariant to a scale transformation of the mineral formula unit. The scale factor appears in both the affinity factor determining the extent of disequilibrium and in the prefactor term, which multiplies the affinity factor. The form of the rate law is obtained by imposing invariance of the reactive transport equations on scaling the mineral formula unit, a basic requirement of all kinetic rate laws describing mineral reactions. This requirement is shown to be consistent with the Horiuti-Temkin formulation of the overall reaction rate for stationary-state conditions. The overall rate law is derived by summing a network of elementary reaction steps each weighted by a stoichiometric number giving the rate of the *i*th intermediate step relative to the overall reaction rate. However, it is noted that current formulations of mineral kinetic rate laws are more empirically based and do not always satisfy the requirement that the elementary reaction steps defining a reaction mechanism sum to form the overall reaction. In addition, there appears to be confusion in the literature between the Temkin average stoichiometric number and the scale factor related to the mineral formula unit, which are shown to be two distinct quantities. Finally, it is noted that in recent numerical simulations modeling sequestration of supercritical CO_2 in deep geologic formations, different chemical formulas for oligoclase have been used related by a scale factor of five without taking into account the scale factor in the kinetic rate law. This oversight could result in potentially significantly larger oligoclase dissolution rates, and exaggerated CO_2 mineralization through precipitation of dawsonite.

Key words: mineral kinetics, scale invariance, Temkin number, reaction mechanism, elementary reaction, reaction intermediate, carbon sequestration, overall reaction, stationary state

INTRODUCTION

The transition state theory (TST) based kinetic rate law has found wide application for modeling water-rock interaction of minerals with an aqueous solution. Aagaard and Helgeson (1982) in their seminal paper on the kinetic rate law for minerals reacting with an aqueous solution based their formulation on TST combined with the Horiuti-Temkin stoichiometric number (Horiuti, 1957; Temkin, 1963), defined as the ratio of the reaction rate of an intermediate reaction step to the overall reaction rate. The relationship between the reaction mechanism represented by a set of elementary reactions and the overall reaction rate was originally presented by Horiuti (1957) and then later extended by Temkin (1963) within the framework of stationary-state reaction kinetics, providing a rigorous formulation of the kinematics of overall reaction kinetics. The insight of Horiuti (1957) and Temkin (1963) was to realize that the overall reaction rate for quasi-stationary state conditions, could be related algebraically to the rates of forward and backward elementary reaction steps which define the reaction mechanism.

However, controversy still appears to exist as to whether the Temkin average stoichiometric number is a fundamental component of the kinetic rate law or whether it merely serves as a fit parameter with no fundamental basis. Lasaga (1995, p. 31–32)

Corresponding author: peter.lichtner@gmail.com

stated that Temkin's method was incorrect due to a simple mathematical error by Boudart (1976) in identifying forward and backward rates of the overall reaction. He further argued that incorporation of Temkin's number was not fundamental to the kinetic rate law (Lasaga, 1995). Gin and others (2008) attempted to evaluate the validity of the Horiuti-Temkin approach but left the issue unresolved. So far the full machinery of the Horiuti-Temkin formulation has not been implemented in the geochemical literature to describe reactions with minerals. This is in part a result of lack of understanding and confusion surrounding this approach, but also due to the difficulty associated with identifying the mechanistic basis for the rate law. In what follows it is demonstrated that the Horiuti-Temkin formulation of the stationary-state overall rate law has a sound mathematical foundation and results in a formal methodology for deriving the overall reaction rate from a specified reaction mechanism formulated in terms of elementary steps. This approach could offer important insight into understanding mineral rate laws.

Aagaard and Helgeson (1982) first drew attention to the role of the Temkin average stoichiometric number, and since then it has been found useful in fitting experimental data in numerous studies of kinetic rate laws describing mineral reactions. Murphy and Helgeson (1987, p. 3148) applied the TST rate law to dissolution of pyroxene and noted that the Temkin number σ depended on the formula unit used to represent pyroxene. For the general pyroxene formula $C(1)C(2)(SiO_3)_2$, where C(1) and C(2) refer to divalent cations (for example, Mg^{2+}, Ca^{2+}, Mn^{2+}, Fe^{2+}) on the M(1) and M(2) pyroxene sites, it follows that $\sigma = 2$; whereas for $C(1)_{0.5}C(2)_{0.5}SiO_3$ it follows that $\sigma = 1$. Berger and others (1994) reported a value of $\sigma = 1$ for quartz, and Gautier and others (1994) a value of $\sigma = 3$ for K-feldspar dissolution. Devidal and others (1997) and Yang and Steefel (2008), found $\sigma = 2$ for kaolinite dissolution and precipitation. Anorthite purportedly has a Temkin number of unity according to Oelkers and Schott (1995). Harouiya and others (2007) proposed a value for Temkin's constant of $\sigma = 5$ for apatite $[Ca_5(PO_4)_3F]$. They noted that this value was consistent with five activated complexes related to breaking Ca–O bonds in the dissolution of one formula unit as the rate limiting step. Criscenti and others (2005) presented an eight-step detailed reaction mechanism with Temkin numbers equal to one for removal of Al from a feldspar surface. It should be pointed out, however, that none of these authors developed a rigorous set of elementary reaction steps that sum to give the overall mineral reaction [An exception, discussed below, is provided by Icopini and others (2005).], and therefore it is not clear whether the assigned Temkin number is consistent with the Horiuti-Temkin formulation or is simply a fit parameter.

In this work a modified form of the mineral rate law is proposed that includes the explicit dependence on a scale factor of the mineral formula unit and corresponding overall reaction, both through the usual affinity factor and also in the rate prefactor. This latter modification appears to have been overlooked in previous work. The modified form of the rate law follows from the implications of scaling the mineral formula unit on the form of the kinetic rate law and invariance of the reactive transport equations under the scale transformation. Clearly, results obtained from solving reactive transport equations should not depend on the mineral formula unit used in the calculation, and any multiple of the formula unit should be equally valid. The resulting form of the rate law is similar in form to that obtained from Temkin's formulation of the overall reaction rate with the scale factor replacing Temkin's stoichiometric number.

In what follows the consequences of the requirement of invariance of mass conservation equations to scaling the mineral formula unit are explored and their implications for the form of the kinetic rate law derived. The observation that the results of solving reactive transport equations should not depend on the mineral

formula unit used to represent mineral reactions has significant consequences on the possible forms that the kinetic rate law can take. Next, following a review of the Horiuti-Temkin formulation of the overall stationary-state kinetic rate law, it is demonstrated that this formulation results in invariant mass conservation equations describing reactive transport provided that the Horiuti-Temkin stoichiometric number is also appropriately scaled. Finally, several observations are made when applying a kinetic rate law to model carbon sequestration and scaling the mineral formula unit as has been presented in the literature.

SCALE INVARIENCE

To determine the transformation properties of the kinetic rate law under a scale transformation of the mineral formula unit, the condition of invariance is imposed on the reactive transport equations. Reaction of an aqueous solution with the mth mineral $\mathcal{M}_m$ is presumed to be described by the overall reaction

$$\sum_{j=1}^{N_c} \nu_{jm} \mathcal{A}_j \rightleftharpoons \mathcal{M}_m, \tag{1}$$

written in canonical form (Lichtner, 1985), involving N_c primary aqueous species (components or basis species) $\mathcal{A}_j$, with stoichiometric reaction coefficients ν_{jm}. The overall reaction rate is denoted by Γ_m normalized to unit specific mineral surface area $\mathcal{A}_m$. The sign convention with the rate positive for precipitation and negative for dissolution is used throughout.

The overall reactions are unique only to within a scale factor of the mineral formula unit. This scale factor cannot have any effect on the prediction of observable quantities. Thus, for example, for kaolinite any of the formula units $AlSiO_{5/2}(OH)_2$, $Al_2Si_2O_5(OH)_4$ or $Al_4Si_4O_{10}(OH)_8$ could be used without affecting the results. Scaling the reaction given in equation (1) by some scale factor $\lambda_m > 0$ gives the equivalent reaction

$$\sum_j \nu'_{jm} \mathcal{A}_j \rightleftharpoons \mathcal{M}'_m, \tag{2}$$

with $\nu'_{jm} = \lambda_m \nu_{jm}$, and $\mathcal{M}'_m = \lambda_m \mathcal{M}_m$. The equilibrium constants for the scaled and unscaled reactions are related by the equation

$$K'_m = K_m^{\lambda_m}. \tag{3}$$

The mineral formula weight W_m scales according to $W'_m = \lambda_m W_m$, as does the mineral molar volume: $\bar{V}'_m = \lambda_m \bar{V}_m$. The number of formula units per unit cell Z_m scales inversely with $Z'_m = \lambda_m^{-1} Z_m$. The mass density ρ_m is invariant: $\rho'_m = \rho_m$. The mineral volume fraction fraction ϕ_m is also an invariant, defined as the volume occupied by the mineral divided by some reference volume (typically the bulk volume or representative elemental volume (REV), the solid volume or pore volume). In contrast, the mineral concentration defined as $C_m = \bar{V}_m^{-1} \phi_m = W_m^{-1} \rho_m \phi_m$ scales inversely with λ_m: $C'_m = \lambda_m^{-1} C_m$. Finally, specific mineral surface area, defined relative to some reference volume, is invariant: $\mathcal{A}'_m = \mathcal{A}_m$.

Under a transformation scaling the mineral formula unit, observables such as the solute concentration and mineral volume fraction obtained from solving reactive transport equations should not be affected and must remain invariant. Mineral reaction rates, however, are affected by scaling the mineral formula unit. To determine the transformation properties of the mineral kinetic rate law, the conservation equations corresponding to unscaled and scaled mineral formulas are compared. These equations for the jth aqueous primary species have the following respective

forms corresponding to the unscaled and scaled mineral formula unit (Lichtner, 1985; Lichtner, 1996; Lichtner, 1998; Steefel and others, 2005; Lichtner and Karra, 2014)

$$\frac{\partial}{\partial t}\varphi\Psi_j + \nabla \cdot \Omega_j = -\sum_m \nu_{jm}\Gamma_m\mathscr{A}_m, \tag{4a}$$

$$= -\sum_m \nu'_{jm}\Gamma'_m\mathscr{A}_m, \tag{4b}$$

where primes indicate that the quantity is evaluated relative to the scaled mineral formula. In these equations φ denotes the porosity of the porous medium, Ψ_j and Ω_j denote the total concentration and flux for the jth primary species or component, respectively, and the sum on the right-hand side is over all minerals in the system of interest.

For the mth mineral its volume fraction defined relative to an REV satisfies the following mass transfer equations corresponding to unscaled and scaled mineral formulas

$$\frac{\partial\phi_m}{\partial t} = \bar{V}_m\Gamma_m\mathscr{A}_m, \tag{5a}$$

$$= \bar{V}'_m\Gamma'_m\mathscr{A}_m. \tag{5b}$$

These conservation equations apply to a general time-space description of reactive transport as well as a batch reactor for closed and open systems.

In order for the aqueous concentrations and mineral volume fractions to be independent of the mineral formula unit, the right-hand sides of equations (4) and (5) must be identical. This requires the following relations to hold identically

$$\nu_{jm}\Gamma_m = \nu'_{jm}\Gamma'_{jm}, \tag{6a}$$

and

$$\bar{V}_m\Gamma_m = \bar{V}'_m\Gamma'_m. \tag{6b}$$

Replacing the primed stoichiometric coefficients ν'_{jm} and molar volume $\bar{V}'_m$ by their corresponding unprimed quantities, these relations imply the transformation rule

$$\lambda_m\Gamma'_m = \Gamma_m. \tag{7}$$

This is a very general result independent of the detailed form of the kinetic rate law.

To see the implications of this transformation rule, consider the overall mineral kinetic rate law expressed in a somewhat simplified form sufficient for the purposes here as

$$\Gamma_m = -k_m\mathscr{P}_m(1 - K_mQ_m). \tag{8}$$

In this equation k_m denotes the kinetic rate constant which is a function of temperature and pressure, and $\mathscr{P}_m$ represents a concentration-dependent prefactor that may be a function of pH and other variables. The last factor in brackets refers to the affinity factor with equilibrium constant K_m corresponding to the overall mineral reaction as written in equation (1), and activity product Q_m defined by

$$Q_m = \prod_j(\gamma_j m_j)^{\nu_{jm}}, \tag{9}$$

with molality m_j and activity coefficient γ_j for the jth primary species. Note that the product K_mQ_m appears in the affinity factor (rather than the more customary form

Q_m/K_m, because the overall reaction is written with the mineral on the right-hand side as in equation (1). The average Temkin stoichiometric number is not included in this form of the rate law. This is considered in detail in the next section within the framework of the Horiuti-Temkin formulation for the overall reaction rate.

Under a scale transformation the activity product Q_m transforms according to

$$Q'_m = \prod_j (\gamma_j m_j)^{\nu_{jm}}, \tag{10a}$$

$$= \prod_j (\gamma_j m_j)^{\lambda_m \nu_{jm}}, \tag{10b}$$

$$= Q_m^{\lambda_m}. \tag{10c}$$

The prefactor is assumed to be independent of the scale transformation

$$\mathcal{P}'_m = \mathcal{P}_m, \tag{11}$$

as is the rate constant

$$k'_m = k_m. \tag{12}$$

These assignments are justified in the Horiuti-Temkin formuation of the overall rate where these quantities are derived from elementary reactions that define the reaction rate mechanism, and are presumed to take place at the molecular scale and therefore are not transformed. Hence, from equations (3), (7) and (10) the overall rate law becomes

$$\Gamma'_m = -\frac{1}{\lambda_m} k_m \mathcal{P}_m (1 - K_m Q_m), \tag{13a}$$

$$= -\frac{1}{\lambda_m} k_m \mathcal{P}_m (1 - (K'_m Q'_m)^{1/\lambda_m}). \tag{13b}$$

Thus, according to this result to obtain the same solution to the reactive transport equations after scaling the mineral formula (and overall reaction), the rate constant k_m must be divided by the scale factor λ_m and the saturation state $K_m Q_m$ raised to the power λ_m^{-1}. Note that for both the scaled and unscaled mineral formula, equilibrium corresponds to

$$K_m Q_m = K'_m Q'_m = 1. \tag{14}$$

HORIUTI-TEMKIN OVERALL RATE LAW

Mineral reactions are generally complex reactions made up of a number of elementary steps. The elementary steps define the reaction mechanism in terms of molecular interactions and are unique and must be implemented as written. An expression for the reaction rate of the overall reaction in terms of rates of the elementary steps can be obtained from the quasi-stationary state approximation. This leads to a greatly simplified form of the rate law.

The general theory has been developed by Horiuti (1957), Hollingsworth (1957), Temkin (1963), and others [see Boudart and Djéga-Mariadassou (1984)]. The main requirement is to represent an overall reaction through a sequence of elementary steps which yield back the overall reaction when each step is multiplied by an appropriate stoichiometric number and summed. In general, multiple pathways may be involved in formation of the same overall reaction; however, this theory is still under development (Temkin, 2012). The usefulness of this approach lies in the ability to formulate the

elementary steps which define the overall reaction. This in itself may be an enormous task and success is not guaranteed. The resulting rate law for the overall reaction must satisfy the constraints imposed by requiring invariance of the rate law under scaling of the mineral formula unit. After first formulating the overall rate in terms of a sequence of elementary steps, its transformation properties under scaling the mineral formula unit are investigated and shown to comply with the transformation rules derived above.

Horiuti-Temkin Formalism

Stationary state and reaction intermediates.—It is assumed that each elementary step involves a set of reactants and products that describes a single mineral $\mathcal{M}_m$ reacting with an aqueous solution. Species which occur in both the elementary steps and in the overall reaction are denoted collectively by $\{\mathcal{A}_j\}$, referred to as terminal species. In addition, species which occur only in the elementary steps but not in the overall reaction, denoted by $\{\mathcal{X}_k\}$, are referred to as reaction intermediates. The overall reaction is constructed by summing the elementary steps weighted by the Horiuti-Temkin stoichiometric number. The species $\mathcal{X}_k$ may represent catalysts, for example, including species sorbed on the surface of the mineral. Each elementary step is assumed to have the general form

$$\sum_j \nu_{ji}^m \mathcal{A}_j + \sum_k x_{ki}^m \mathcal{X}_k \rightleftharpoons \nu_{mi} \mathcal{M}_m, \tag{15}$$

with stoichiometric coefficients ν_{mi}, ν_{ji}^m and x_{ki}^m corresponding to the ith step for reaction of the mth mineral. The sum over j is over terminal species $\mathcal{A}_j$, and the sum over k is over the reaction intermediates $\mathcal{X}_k$.

The corresponding overall reaction is formed by multiplying each step by the Horiuti-Temkin stoichiometric number denoted by σ_{mi} and summing over all steps to give

$$\sum_j \nu_{jm} \mathcal{A}_j = \nu_m \mathcal{M}_m, \tag{16}$$

where the stoichiometric coefficients for the overall reaction are given by

$$\nu_{jm} = \sum_i \sigma_{mi} \nu_{ji}^m, \tag{17}$$

and the stoichiometric coefficients ν_{mi} are given by

$$\sum_i \sigma_{mi} \nu_{mi} = \nu_m, \tag{18}$$

The coefficients σ_{mi} are chosen so that the reaction intermediates $\mathcal{X}_k$ are absent from the overall reaction

$$\sum_i \sigma_{mi} x_{ki}^m = 0. \tag{19}$$

From the time-evolution equations corresponding to the elementary reaction steps, it follows that the time rate of change for the total primary species concentrations and minerals is given by

$$\frac{\partial}{\partial t} \varphi \Psi_j + \nabla \cdot \Omega_j = \mathcal{R}_j, \tag{20a}$$

$$\frac{\partial}{\partial t} \varphi \Psi_k + \nabla \cdot \Omega_k = \mathcal{R}_k, \tag{20b}$$

$$\frac{\partial \phi_m}{\partial t} = \mathcal{R}_m, \tag{20c}$$

with the reaction rates $\mathcal{R}_j$, $\mathcal{R}_k$, and $\mathcal{R}_m$ defined respectively as

$$\mathcal{R}_j = -\sum_{mi} \nu_{ji}^m \mathcal{A}_m \Gamma_{mi}, \tag{21a}$$

$$\mathcal{R}_k = -\sum_{mi} x_{ki}^m \mathcal{A}_m \Gamma_{mi}, \tag{21b}$$

$$\mathcal{R}_m = \bar{V}_m \mathcal{A}_m \sum_i \nu_{mi} \Gamma_{mi}. \tag{21c}$$

In terms of the overall reaction, equation (16), the reaction rates become

$$\mathcal{R}_j = -\sum_{mi} \nu_{jm} \mathcal{A}_m \Gamma_m, \tag{22a}$$

$$\mathcal{R}_k = 0, \tag{22b}$$

$$\mathcal{R}_m = \bar{V}_m \nu_m \mathcal{A}_m \Gamma_m. \tag{22c}$$

Comparing equations (22) and (21), making use of equations (17), (18) and (19), leads to the condition

$$\sum_i x_{ki}^m \Gamma_{mi} = 0, \tag{23}$$

for intermediate species implying stationary-state conditions. Comparing rate terms for the jth primary species leads to

$$\sum_i \nu_{ji}^m (\sigma_{mi} \Gamma_m - \Gamma_{mi}) = 0. \tag{24}$$

Requiring that the quantity in brackets vanish for each elementary step implies

$$\sigma_{mi} \Gamma_m = \Gamma_{mi}. \tag{25}$$

Alternatively, introducing reaction progress variables ξ_{mi} and ξ_m corresponding to the elementary steps and overall reaction, equations (15) and (16), respectively, equation (25) is equivalent to

$$\frac{d\xi_{mi}}{d\xi_m} \frac{d\xi_m}{dt} = \frac{d\xi_{mi}}{dt}, \tag{26}$$

with

$$\sigma_{mi} = \frac{d\xi_{mi}}{d\xi_m}. \tag{27}$$

Elementary reactions may satisfy conditions of quasi-equilibrium or stationary-state conditions. Note that there appears to be a contradiction if an intermediate step is in equilibrium. Because then $\Gamma_{mi} = 0$ for this step and from equation (25) this would imply that the overall reaction rate must also vanish. But in fact, equilibrium of an elementary step does not hold exactly. Forward and backward rates are only approximately equal, although much larger compared to the overall reaction rate (see fig. 1 and Appendix A).

The reaction rate for the ith elementary reaction step is based on the law of mass action given by

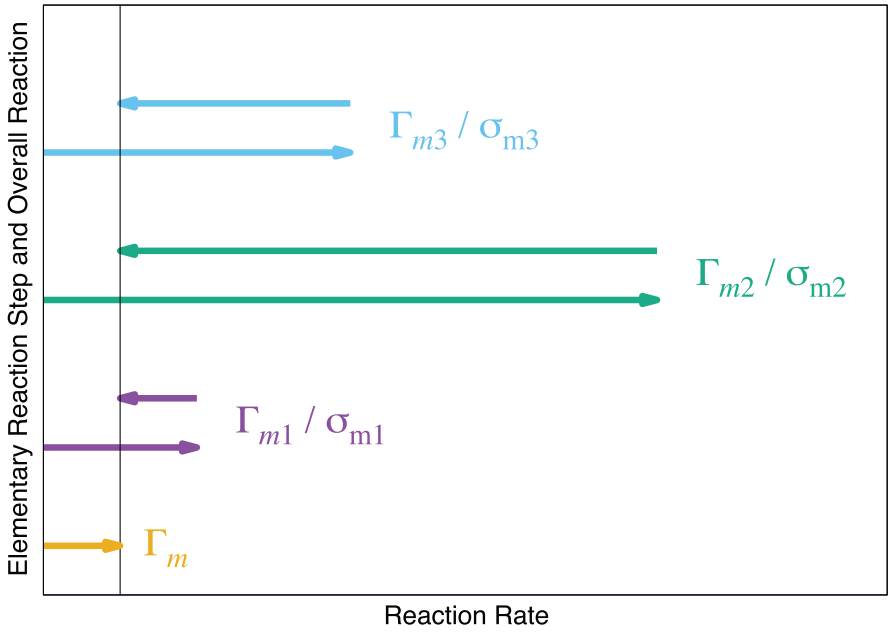

Fig. 1. Schematic diagram showing net reaction rates for three elementary steps and the overall reaction rate Γ_m designated by the vertical line. Step 2 with net rate Γ_{m2} is approximately in equilibrium, and step 1, with net rate Γ_{m1}, is the rate determining step. Stationary state conditions require that each net elementary rate Γ_{mi} divided by its Temkin stoichiometric number σ_{mi} equal the overall net reaction rate. Figure adapted from Boudart and Djéga-Mariadassou (1984), who attribute it to Tamura (1978).

$$\Gamma_{mi} = k^+_{mi} Q^+_{mi} - k^-_{mi} Q^-_{mi}, \tag{28}$$

with activity products $Q^{\pm}_{mi}$ defined as

$$Q^+_{mi} = \prod_{\nu^m_{ji}>0} a_j^{\nu^m_{ji}} \prod_{x^m_{ji}>0} a_k^{x^m_{ki}}, \tag{29a}$$

$$Q^-_{mi} = \prod_{\nu^m_{ji}<0} a_j^{-\nu^m_{ji}} \prod_{x^m_{ji}<0} a_k^{-x^m_{ki}}, \tag{29b}$$

with a_j the activity of the jth terminal solute species, a_k the activity of the kth reaction intermediate, and forward and backward rate constants $k^{\pm}_{mi}$, respectively.

By definition of an elementary reaction the ratio of the forward and backward rate constants for the ith step is equal to the corresponding equilibrium constant

$$k_{mi} = \frac{k^+_{mi}}{k^-_{mi}}. \tag{30}$$

Equilibrium holds when

$$K_{mi} Q_{mi} = 1, \tag{31}$$

where the activity product Q_{mi} is defined by

$$Q_{mi} = \frac{Q^+_{mi}}{Q^-_{mi}} = \prod_j a_j^{\nu^m_{ji}} \prod_k a_k^{x^m_{ki}}, \tag{32}$$

where the product over the subscript j refers to terminal species appearing in the overall reaction, and the product over k refers to reaction intermediates.

The equilibrium constant for the overall reaction is related to the equilibrium constants of the elementary steps by the usual equation

$$K_m = \prod_i K_{mi}^{\sigma_{mi}} = \prod_i \left(\frac{k_{mi}^+}{k_{mi}^-}\right)^{\sigma_{mi}}. \tag{33}$$

Likewise, the activity product of the overall reaction is equal to the product

$$Q_m = \prod_i Q_{mi}^{\sigma_{mi}} = \prod_j a_j^{\nu_{jm}}, \tag{34}$$

where the latter equality follows from equations (17) and (19).

Temkin identity.—An expression for the overall reaction rate can be computed algebraically in terms of the rates of elementary intermediate reactions from the mathematical identity first introduced by Temkin (1963) in generalizing the work of Horiuti (1957)

$$\begin{aligned}(\Gamma_{m1}^+ - \Gamma_{m1}^-)\Gamma_{m2}^+\Gamma_{m3}^+\cdots\Gamma_{mN_s}^+ &+ \Gamma_{m1}^-(\Gamma_{m2}^+ - \Gamma_{m2}^-)\Gamma_{m3}^+\Gamma_{m4}^+\cdots\Gamma_{mN_s}^+ \\ &+ \Gamma_{m1}^-\Gamma_{m2}^-(\Gamma_{m3}^+ - \Gamma_{m3}^-)\Gamma_{m4}^+\cdots\Gamma_{mN_s}^+ \\ &+ \cdots \\ &+ \Gamma_{m1}^-\Gamma_{m2}^-\Gamma_{m3}^-\cdots\Gamma_{m,N_s-1}^-(\Gamma_{mN_s}^+ - \Gamma_{mN_s}^-) \\ \equiv \Gamma_{m1}^+\Gamma_{m2}^+\Gamma_{m3}^+\cdots\Gamma_{mN_s}^+ &- \Gamma_{m1}^-\Gamma_{m2}^-\Gamma_{m3}^-\cdots\Gamma_{mN_s}^-.\end{aligned} \tag{35}$$

Substituting equation (25) for $\Gamma_{mi}^+ - \Gamma_{mi}^- = \sigma_{mi}\Gamma_m$ into equation (35), this identity can be written in the more concise form

$$\Gamma_m \sum_i \sigma_{mi} D_{mi} = \prod_i \Gamma_{mi}^+ - \prod_i \Gamma_{mi}^-, \tag{36}$$

where the quantity D_{mi} is defined by the product over elementary reaction steps as

$$D_{mi} = \Gamma_{m1}^-\Gamma_{m2}^-\cdots\Gamma_{m,i-1}^-\Gamma_{m,i+1}^+\cdots\Gamma_{mN_s}^+, \tag{37}$$

in which the factor Γ_{mi} corresponding to the ith step is omitted. This equation yields the following expression for the overall reaction rate

$$\Gamma_m = \frac{1}{\sum_i \sigma_{mi} D_{mi}}\left[\prod_i \Gamma_{mi}^+ - \prod_i \Gamma_{mi}^-\right]. \tag{38}$$

Temkin's identity, equation (35), is independent of a change of sign in the reaction rates and permutation of elementary steps. For $N_s = 2, 3, 4$ the sum in the denominator becomes

$$\sum_i \sigma_{mi} D_{mi} = \sigma_{m1}\Gamma_{m2}^+ + \sigma_{m2}\Gamma_{m1}^-, \qquad (\mathrm{N} = 2), \tag{39a}$$

$$= \sigma_{m1}\Gamma_{m2}^+\Gamma_{m3}^+ + \sigma_{m2}\Gamma_{m1}^-\Gamma_{m3}^+ + \sigma_{m3}\Gamma_{m1}^-\Gamma_{m2}^-, \qquad (\mathrm{N} = 3), \tag{39b}$$

$$\begin{aligned}= \sigma_{m1}\Gamma_{m2}^+\Gamma_{m3}^+\Gamma_{m4}^+ &+ \sigma_{m2}\Gamma_{m1}^-\Gamma_{m3}^+\Gamma_{m4}^+ \\ &+ \sigma_{m3}\Gamma_{m1}^-\Gamma_{m2}^-\Gamma_{m4}^+ + \sigma_{m4}\Gamma_{m1}^-\Gamma_{m2}^-\Gamma_{m3}^-.\end{aligned} \qquad (\mathrm{N} = 4), \tag{39c}$$

For the case of reversible reactions where $\Gamma^-_{mi} \neq 0$, the overall rate can be written in the form

$$\Gamma_m = -\frac{1}{\sum_i \sigma_{mi} D_{mi}} \left(\prod_i \Gamma^-_{mi} \right) \left[1 - \prod_i \left(\frac{\Gamma^+_{mi}}{\Gamma^-_{mi}} \right) \right]. \tag{40}$$

If all intermediate steps are irreversible (for example $\Gamma^-_{mi} = 0$ all i), the equation for the overall rate simplifies to

$$\Gamma_m = \frac{1}{\sigma_{mi}} \Gamma^+_{mi}, \quad (i = 1,\ldots,N_s). \tag{41}$$

Temkin average stoichiometric number.—The third term in square brackets in equation (40), corresponding to the affinity factor, can be further manipulated to express it in terms of the equilibrium constant and activity product of the overall reaction. It follows from the definition of an elementary reaction that

$$\prod_i \frac{\Gamma^+_{mi}}{\Gamma^-_{mi}} = \prod_i e^{A_{mi}/RT} = e^{\frac{1}{RT}\sum_i A_{mi}}, \tag{42a}$$

$$= \prod_i K_{mi} Q_{mi}, \tag{42b}$$

where A_{mi} denotes the affinity of the ith elementary step associated with the mth mineral, R denotes the gas constant and T is the temperature. The right-hand side can be written in terms of the affinity of the overall reaction given by

$$A_m = \sum_i \sigma_{mi} A_{mi}, \tag{43}$$

by introducing the Temkin average stoichiometric number σ_m defined as the weighted arithmetic mean

$$\sigma_m = \frac{\sum_i \sigma_{mi} A_{mi}}{\sum_i A_{mi}} = \frac{A_{mi}}{\sum_i A_{mi}}. \tag{44}$$

Alternatively, in terms of the equilibrium constant K_{mi} and activity product Q_{mi} for the ith elementary step, the average stoichiometric number becomes

$$\sigma_m = \frac{\sum_i \sigma_{mi} \ln K_{mi} Q_{mi}}{\sum_{i'} \ln K_{mi} Q_{mi}}, \tag{45}$$

which may also be expressed as

$$\prod_i K_{mi} Q_{mi} = \prod_i (K_{mi} Q_{mi})^{\sigma_{mi}/\sigma_m}. \tag{46}$$

The average Temkin stoichiometric number is, in general, a function of temperature, pressure and composition. Defining $\chi_{mi} = \ln K_{mi} Q_{mi}$, computing the derivative of σ_m with respect to χ_{mi} yields

$$\frac{\partial \sigma_m}{\partial \chi_{mi}} = \frac{\sigma_{mi}}{\sum_{i'} \chi_{mi'}} \left(1 - \frac{\sigma_m}{\sigma_{mi}} \right). \tag{47}$$

Therefore, σ_m is constant only if $\sigma_{mi} = \sigma_m$ for all i, a highly restrictive condition. Boudart (1976) refers to a "good" average stoichiometric number as one that for all practical purposes is constant.

With equation (45) the following expression is obtained for the affinity factor in terms of the overall reaction affinity A_m, equilibrium constant K_m and activity product Q_m

$$\prod_i \left(\frac{\Gamma^+_{mi}}{\Gamma^-_{mi}}\right) = e^{\frac{1}{\sigma_m RT} A_m}, \tag{48a}$$

$$= (K_m Q_m)^{1/\sigma_m}. \tag{48b}$$

Substituting this result into equation (40) the overall reaction rate can be written equivalently as

$$\Gamma_m = -\frac{1}{\mathcal{D}_m}\left[\prod_i \Gamma^-_{mi}\right]\left(1 - e^{\frac{1}{\sigma_m RT} A_m}\right), \tag{49a}$$

$$= -\frac{1}{\mathcal{D}_m}\left[\prod_i \Gamma^-_{mi}\right]\left(1 - (K_m Q_m)^{1/\sigma_m}\right), \tag{49b}$$

with the quantity $\mathcal{D}_m$ defined by

$$\mathcal{D}_m = \sum_i \sigma_{mi} \mathcal{D}_{mi}. \tag{50}$$

The overall reaction rate consists of a prefactor that is a function of the rates of the elementary steps times the affinity factor. The above expression for the overall reaction rate explicitly exhibits the dependence of the rate on the Temkin stoichiometric numbers, both in the prefactor involving the individual σ_{mi} through the quantity $\mathcal{D}_m$, and in the affinity factor where the average Temkin number σ_m appears.

Rate determining step.—In the general case of multiple reaction steps with different stoichiometric numbers, the average stoichiometric coefficient depends on the concentration of the various species involved. However, for a single rate determining step $\hat{\imath}$, with all other steps close to equilibrium ($A_{mi} \approx 0$, $\Gamma^+_{mi} \approx \Gamma^-_{mi}$, $i \neq \hat{\imath}$), it follows from equation (45) that $\sigma_m = \sigma_{m\hat{\imath}}$, and the formulation for the overall reaction rate greatly simplifies. Equation (40) for the overall reaction rate becomes

$$\Gamma_m = -\frac{1}{\sigma_{m\hat{\imath}} \mathcal{D}_{m\hat{\imath}}}\left[\prod_i \Gamma^-_{mi}\right]\left(1 - \frac{\Gamma^+_{m\hat{\imath}}}{\Gamma^-_{m\hat{\imath}}}\right), \tag{51}$$

with

$$\frac{\Gamma^+_{m\hat{\imath}}}{\Gamma^-_{m\hat{\imath}}} = (K_m Q_m)^{1/\sigma_{m\hat{\imath}}}, \tag{52}$$

and

$$\sum_i \sigma_{mi} D_{mi} \approx \sigma_{m\hat{\imath}} D_{m\hat{\imath}}, \tag{53}$$

since $\Gamma^{\pm}_{mi} \gg \Gamma^{\pm}_{m\hat{\imath}}$, $(i \neq \hat{\imath})$. In this formulation of the overall reaction rate the dependence of the rate on the Horiuti-Temkin stoichiometric number $\sigma_{m\hat{\imath}}$ is explicitly singled out. The form of the rate law given in equation (51) is slightly different from that usually reported in the literature in that the Horiuti-Temkin stoichiometric number appears twice: once in the affinity factor corresponding to the conventional

formulation [equation (52)], and also as an overall scale factor of the rate appearing in the denominator in equation (51). Although Aagaard and Helgeson (1982) explicitly included the factor σ_{mi} appearing in the affinity term of the rate law, they absorbed it into the rate constant k_m, rather than making explicit provision for it in the prefactor. As becomes apparent below, it is advantageous to leave σ_{mi} as a explicit factor in the rate law.

Overall forward and backward reaction rates and equilibrium constant.—So far in the development of the Horiuti-Temkin formulation of overall reaction rates there has been no need to introduce explicit expressions for the forward and backward overall rates. In this section these quantities are defined and a relation is derived for the overall equilibrium constant and forward and backward rate constants. There appears to be no need to define forward and backward reaction rates for the overall reaction, unlike the case for elementary reactions for which they are well defined. Equation (49) suffices to describe both forward and backward rates as it stands without dividing it into separate terms. Nevertheless, expressions for the forward and backward reaction rates $\Gamma_m^{\pm}$ of the overall reaction can be found by noting that two conditions must be satisfied. First, by definition the net overall rate is equal to the difference in the forward and backward reaction rates

$$\Gamma_m = \Gamma_m^+ - \Gamma_m^-, \tag{54a}$$

and, second, the ratio of the forward and backward rates is equal to the saturation state

$$\frac{\Gamma_m^+}{\Gamma_m^-} = \prod_i \left(\frac{\Gamma_{mi}^+}{\Gamma_{mi}^-}\right). \tag{54b}$$

Solving these equations for $\Gamma_m^{\pm}$ gives

$$\Gamma_m^{\pm} = \frac{1}{\mathscr{D}_m} \prod_i \Gamma_{mi}^{\pm}, \tag{55}$$

as expected. Alternatively, the forward and backward rates can be expressed in terms of the overall reaction rate and affinity factor as

$$\Gamma_m^+ = -\frac{(K_m Q_m)^{1/\sigma_m}}{1-(K_m Q_m)^{1/\sigma_m}} \Gamma_m, \tag{56a}$$

$$\Gamma_m^- = -\frac{1}{1-(K_m Q_m)^{1/\sigma_m}} \Gamma_m. \tag{56b}$$

There does not generally exist a simple relation between the equilibrium constant for the overall reaction and the forward and backward rate constants as exists for elementary reactions [see equation (30)]. The affinity factor for the overall reaction can be written as

$$\frac{\Gamma_m^+}{\Gamma_m^-} = \frac{k_m^+ Q_m^+}{k_m^- Q_m^-} = (K_m Q_m)^{1/\sigma_m}, \tag{57}$$

where K_m and Q_m are defined by equations (33) and (34), and where the forward and backward rate constants $k_m^{\pm}$ are defined as

$$k_m^{\pm} = \prod_i k_{mi}^{\pm}, \tag{58}$$

and the activity products $Q_m^{\pm}$ as

$$Q_m^{\pm} = \prod_i Q_{mi}^{\pm}, \tag{59}$$

with $Q_m^{\pm}$ given by equations (29a and 29b). From equation (57) it follows that

$$\frac{k_m^+}{k_m^-} = K_m^{1/\sigma_m} \frac{Q_m^-}{Q_m^+} Q_m^{1/\sigma_m}, \tag{60a}$$

$$= K_m^{1/\sigma_m} \prod_j a_j^{\zeta_{jm}} \prod_k a_k^{\omega_{km}}, \tag{60b}$$

where the exponents ζ_{jm} and ω_{km} are defined by

$$\zeta_{jm} = \frac{1}{\sigma_m} \nu_{jm} - \sum_i \nu_{ji}^m, \tag{61a}$$

$$= \sum_i \left(\frac{\sigma_{mi}}{\sigma_m} - 1 \right) \nu_{ji}^m, \tag{61b}$$

for species which appear in the overall reaction, and

$$\omega_{km} = - \sum_i x_{ki}^m, \tag{62}$$

for reaction intermediates. The condition for $\zeta_{jm} = \omega_{km} = 0$ is that $\sigma_{mi} = \sigma_m$ for all elementary steps i as follows from equations (61b) and (19). In this case the forward and backward rate constants are related to the equilibrium constant by [see also Boudart and Djéga-Mariadassou (1984), Boudart (1976)]

$$K_m = \left(\frac{k_m^+}{k_m^-} \right)^{\sigma_m}. \tag{63}$$

However, this simple relation does not hold in general. For the case that $\zeta_{jm} \neq 0$, $\omega_{km} \neq 0$, a more complicated relation results and, since the equilibrium constant and forward and backward rate constants are, by definition, independent of concentration and only depend on temperature and pressure, the average Temkin stoichiometric number must be concentration dependent.

Examples

In the following, the Horiuti-Temkin formulation for the overall reaction rate is applied to several examples: a three-component system, ozone destruction, quartz dissolution and precipitation, a hypothetical reaction with solid AB(s) and oligomerization of silica. In addition, in Appendix B a comparison is made with an overall rate expression presented in Lasaga (1998) and Nagy and others (1991) for the reaction A+B+S $\rightleftharpoons$ C+D $\rightleftharpoons$ P+Q, with solid S and aqueous species A, B, C, D, P, and Q.

Three-component system.—A simple example applying the above equations to the three-component irreversible reactions A$\rightarrow$B$\rightarrow$C is shown in figure 2. Details are presented in Appendix A. The example problem illustrates conditions necessary for formation of a stationary state by comparison with an analytical solution. The overall reaction rate for irreversible reactions is compared to the case with reversible elementary reactions. Two examples are shown assuming $C_A^0 = 1$ and $C_B^0 = C_C^0 = 0$. The first example with $k_1^+ = 0.1$ and $k_2^+ = 0.05$, results in a transient solution that does not obey the stationary-state assumption over the time period considered. For the second $k_1^+ = 0.1$ and $k_2^+ = 1$, so that $k_2^+ \gg k_1^+$. This results in a stationary-state for which Temkin's identity applies following a short induction time proportional to $(k_1^+)^{-1}$.

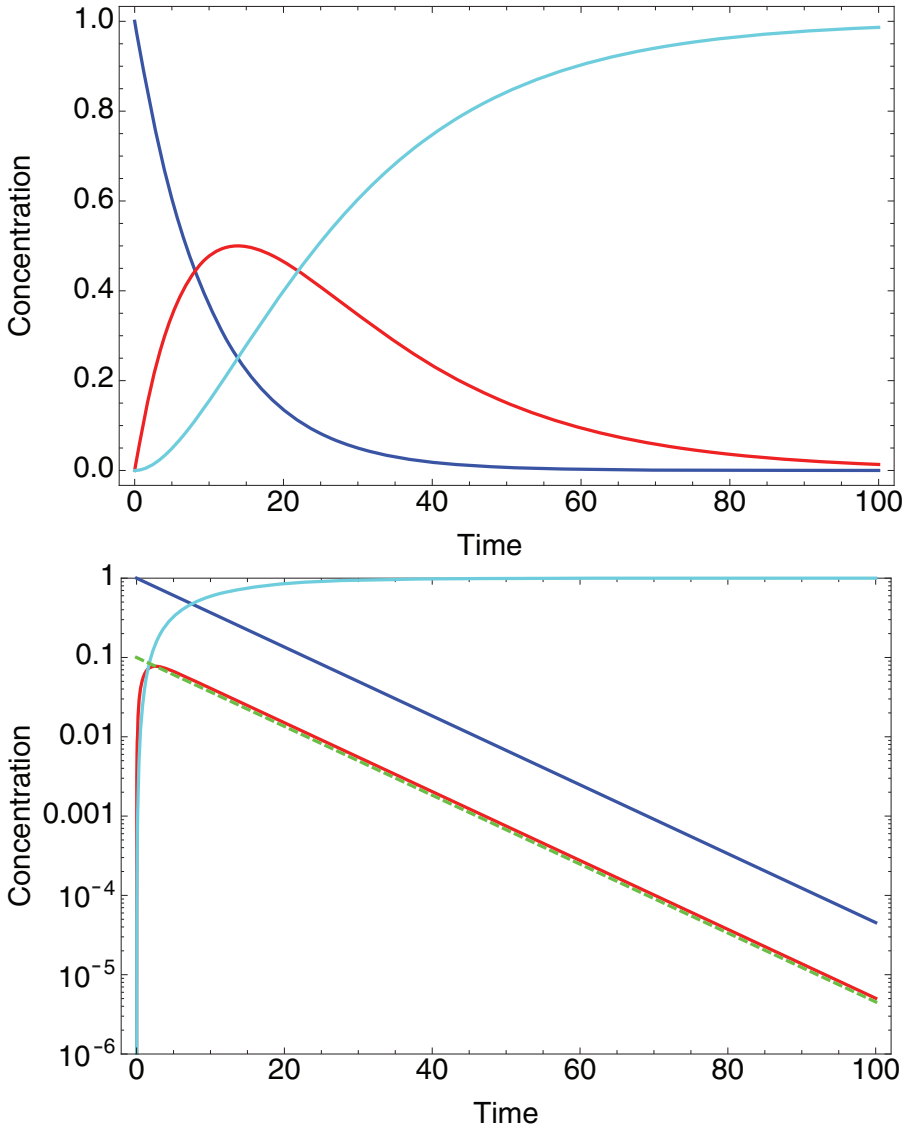

Fig. 2. Plot of analytical solution for $k_1^+ = 0.1$, $k_2^+ = 0.05$ (top), and $k_1^+ = 0.1$, $k_2^+ = 1$ (bottom) for the irreversible reactions given in equation (A-1). Concentrations correspond to C_A (blue), C_B (red) and C_C (cyan). The dashed green curve in the lower plot corresponds to $C_B \approx k_1^+/k_2^+ C_A$.

Ozone destruction.—A simple example of the Temkin formalism for the overall reaction rate is provided by the decomposition of ozone. The overall reaction has the form

$$2O_3 \rightarrow 3O_2, \tag{64}$$

which represents a complex reaction with reaction rate confirmed by experiment of the form

$$\Gamma = k\frac{[O_3]^2}{[O_2]}, \tag{65}$$

with concentrations [. . .]. The rate is second order in $[O_3]$ and inversely proportional to the concentration of the product species $[O_2]$ with order -1, and is clearly not an elementary reaction. The irreversible reaction mechanism for ozone decomposition involving free oxygen O as a reaction intermediate may be formulated according to:

$$O_3 \rightleftharpoons O_2 + O, \tag{66a}$$

$$O + O_3 \rightarrow 2O_2. \tag{66b}$$

Summing the elementary reaction steps leads to the overall reaction given in equation (64). The second reaction is considered to be much slower compared to the first and defines the rate limiting step. The forward and backward elementary reaction rates are given by

$$\Gamma_1^+ = k_1^+[O_3], \tag{67a}$$

$$\Gamma_1^- = k_1^-[O_2][O], \tag{67b}$$

$$\Gamma_2^+ = k_2^+[O_3][O], \tag{67c}$$

$$\Gamma_2^- = 0, \tag{67d}$$

where $\Gamma_1^{\pm}$ refers to the forward and backward rate of the reaction given in equation (66a), and $\Gamma_2^{\pm}$ the corresponding rates for the reaction given in equation (66b). The time rate of change of the individual species follows from

$$\frac{d}{dt}[O_3] = -(\Gamma_1 + \Gamma_2), \tag{68a}$$

$$\frac{d}{dt}[O_2] = (\Gamma_1 + 2\Gamma_2), \tag{68b}$$

$$\frac{d}{dt}[O] = \Gamma_1 - \Gamma_2, \tag{68c}$$

with $\Gamma_i = \Gamma_i^+ - \Gamma_i^-$. Imposing stationary-state conditions implies that $\Gamma_1 \approx \Gamma_2$, requiring that the concentration of the intermediate species [O] satisfy $d[O]/dt \approx 0$. Solving for [O] leads to an expression for the concentration of [O] in terms of $[O_3]$ and $[O_2]$

$$[O] = \frac{k_1^+[O_3]}{k_2^+[O_3] + k_1^-[O_2]}. \tag{69}$$

The overall reaction rate then follows as

$$\Gamma = \frac{\Gamma_1^+\Gamma_2^+}{\Gamma_2^+ + \Gamma_1^-}, \tag{70a}$$

$$= \frac{k_1^+k_2^+[O_3]^2[O]}{k_2^+[O_3][O] + k_1^-[O_2][O]}, \tag{70b}$$

$$= k_1^+[O_3]\zeta, \tag{70c}$$

where the factor ζ is defined as

$$\zeta = \frac{\frac{k_2^+ [O_3]}{k_1^- [O_2]}}{1 + \frac{k_2^+ [O_3]}{k_1^- [O_2]}}. \tag{71}$$

For the case where the rate determining step is given by the irreversible reaction [equation (66b)], it follows that $k_2^+[O_3] \ll k_1^-[O_2]$, and the overall rate reduces to equation (65) in agreement with experiment with k given by

$$k = \frac{k_1^+ k_2^+}{k_1^-}. \tag{72}$$

Of course, this result can be easily derived directly by making use of the stationary-state assumption and rate limiting step without invoking the Temkin formalism for the overall reaction rate [See, for example, Lasaga (1981)].[1]

Reaction of quartz.—It is instructive to apply the Temkin formulation for the overall reaction rate to the dissolution and precipitation of quartz (Rimstidt and Barnes, 1980). Perhaps the simplest formulation consists of the elementary reactions

$$SiO_{2(aq)} \rightleftharpoons SiO_2^\ddagger, \tag{73a}$$

$$SiO_2^\ddagger \rightleftharpoons SiO_{2(s)}, \tag{73b}$$

with formation of the intermediate $SiO_2^\ddagger$. The corresponding reaction rates are designated as Γ_1 and Γ_2. Summing with Horiuti-Temkin stoichiometric numbers $\sigma_1 = \sigma_2 = 1$, gives the overall reaction

$$SiO_{2(aq)} = SiO_{2(s)}. \tag{74}$$

The forward and backward reaction rates are given by

$$\Gamma_1^+ = k_1^+ a_{SiO_{2(aq)}}, \tag{75a}$$

$$\Gamma_1^- = k_1^- a_{SiO_2^\ddagger}, \tag{75b}$$

$$\Gamma_2^+ = k_2^+ a_{SiO_2^\ddagger}, \tag{75c}$$

$$\Gamma_2^- = k_2^-, \tag{75d}$$

with forward and backward rate constants $k_{1,2}^\pm$. The resulting system of ordinary differential equations possesses an analytical solution that is analyzed in detail in Appendix A.

Assuming equilibrium of the first reaction $\Gamma_1 \simeq 0$, the overall reaction rate can be expressed as

$$\Gamma = -\frac{\Gamma_2^- \Gamma_1^-}{\Gamma_2^+ + \Gamma_1^-}\left(1 - \frac{\Gamma_2^+}{\Gamma_2^-}\right). \tag{76}$$

[1] It should be noted, however, that equation (15), Lasaga (1981, Chapter 1, p. 9), is incorrect due to the factor of 2/3 multiplying $k_1 k_2 / k_{-1}$ in that equation [compare with equation (72) above which uses a slightly different notation: $k_{1,2}^+ = k_{1,2}$, $k_1^- = k_{-1}$]. This error arises from canceling the first two terms on the right-hand side of equation (12) in Lasaga (1981), after making the approximation $k_{-1}[O_2] \gg k_2[O_3]$. In fact, by combining these two terms without any approximation, one half the third term is obtained. Combining these terms then results in equation (72) above without the factor 2/3. Lasaga [1998, p. 12, equation (1.17)] has corrected the error, however, the derivation remains incorrect.

Equilibrium of the intermediate species implies

$$a_{\mathrm{SiO}_2^{\ddagger}} = \frac{k_1^+}{k_1^-} a_{\mathrm{SiO}_{2(\mathrm{aq})}}. \tag{77}$$

Thus

$$\frac{\Gamma_2^+}{\Gamma_2^-} = \frac{k_2^+}{k_2^-} a_{\mathrm{SiO}_2^{\ddagger}}, \tag{78a}$$

$$= \frac{k_2^+ k_1^+}{k_2^- k_1^-} a_{\mathrm{SiO}_{2(\mathrm{aq})}}, \tag{78b}$$

and the prefactor becomes

$$\frac{\Gamma_2^- \Gamma_1^-}{\Gamma_2^+ + \Gamma_1^-} = \frac{k_2^- k_1^-}{k_2^+ + k_1^-}. \tag{79}$$

With these results the reaction rate Γ for the overall reaction can be written as

$$\Gamma = -k(1 - KQ), \tag{80}$$

with rate constant k given by

$$k = \frac{k_2^- k_1^-}{k_2^+ + k_1^-}, \tag{81}$$

and equilibrium constant K for the overall reaction equal to

$$K = \frac{k_2^+ k_1^+}{k_2^- k_1^-}. \tag{82}$$

The activity product Q is equal to the silica aqueous activity

$$Q = a_{\mathrm{SiO}_{2(\mathrm{aq})}}. \tag{83}$$

Thus the traditional form of the rate law first developed by Rimstidt and Barnes (1980) is obtained.

In place of equilibrium of the intermediate species a stationary state could have been assumed resulting in the relation

$$k_1^+ a_{\mathrm{SiO}_2} - k_1^- a_{\mathrm{SiO}_2^{\ddagger}} = k_2^+ a_{\mathrm{SiO}_2^{\ddagger}} - k_2^-, \tag{84}$$

or solving for $a_{\mathrm{SiO}_2^{\ddagger}}$

$$a_{\mathrm{SiO}_2^{\ddagger}} = \frac{k_1^+ a_{\mathrm{SiO}_{2(\mathrm{aq})}} + k_2^-}{k_2^+ + k_2^-}. \tag{85}$$

This relation includes equilibrium as a special case. The overall rate is then given by the more general expression

$$\Gamma = -\frac{\Gamma_1^- \Gamma_2^-}{\Gamma_2^+ + \Gamma_1^-}\left(1 - \frac{\Gamma_1^+ \Gamma_2^+}{\Gamma_1^- \Gamma_2^-}\right), \tag{86}$$

which also leads to equation (80).

An alternative formulation is based on the elementary reactions

$$\mathrm{X} + \mathrm{SiO}_{2(\mathrm{aq})} \rightleftharpoons \mathrm{XSiO}_2^{\dagger}, \tag{87a}$$

$$\mathrm{XSiO}_2^{\dagger} \rightleftharpoons \mathrm{X} + \mathrm{SiO}_{2(\mathrm{s})}, \tag{87b}$$

involving sorption on the quartz surface with intermediate species corresponding to the surface complex $\mathrm{XSiO}_2^{\dagger}$ and empty site X. Summing these reactions with $\sigma_1 = \sigma_2 = 1$, again results in equation (74). The corresponding forward and backward reaction rates now become

$$\Gamma_1^+ = k_1^+ S_{\mathrm{X}} a_{\mathrm{SiO}_{2(\mathrm{aq})}}, \tag{88a}$$

$$\Gamma_1^- = k_1^- S_{\mathrm{XSiO}_2^{\dagger}}, \tag{88b}$$

$$\Gamma_2^+ = k_2^+ S_{\mathrm{XSiO}_2^{\dagger}}, \tag{88c}$$

$$\Gamma_2^- = k_2^- S_{\mathrm{X}}, \tag{88d}$$

with sorbed concentrations S_{X}, $S_{\mathrm{XSiO}_2^{\dagger}}$, and with forward and backward rate constants $k_{1,2}^{\pm}$. Equation (38) gives for the overall rate

$$\Gamma = \frac{\Gamma_2^+\Gamma_1^+ - \Gamma_2^-\Gamma_1^-}{\Gamma_2^+ + \Gamma_1^-}. \tag{89}$$

Assuming that the first elementary reaction in equilibrium ($\Gamma_1 \simeq 0$) yields the expression

$$\Gamma = -\frac{\Gamma_2^-\Gamma_1^-}{\Gamma_2^+ + \Gamma_1^-}\left(1 - \frac{\Gamma_2^+}{\Gamma_2^-}\right). \tag{90}$$

The intermediate species and empty site concentrations satisfy the relations

$$S_{\mathrm{X}} + S_{\mathrm{XSiO}_2^{\dagger}} = \omega, \tag{91a}$$

with surface site concentration ω, and

$$\frac{k_1^+}{k_1^-} = \frac{S_{\mathrm{XSiO}_2^{\dagger}}}{S_{\mathrm{X}} a_{\mathrm{SiO}_{2(\mathrm{aq})}}}. \tag{91b}$$

Solving for S_{X} and $S_{\mathrm{SiO}_2^{\dagger}}$ yields the expressions

$$S_X = \frac{\omega}{1 + K_{\mathrm{ex}} a_{\mathrm{SiO}_{2(\mathrm{aq})}}}, \tag{92a}$$

and

$$S_{\mathrm{SiO}_2^{\dagger}} = \frac{\omega K_{\mathrm{ex}} a_{\mathrm{SiO}_{2(\mathrm{aq})}}}{1 + K_{\mathrm{ex}} a_{\mathrm{SiO}_{2(\mathrm{aq})}}}, \tag{92b}$$

with exchange equilibrium constant K_{ex} given by

$$K_{\mathrm{ex}} = \frac{k_1^+}{k_1^-}. \tag{93}$$

It follows that

$$\frac{\Gamma_2^+}{\Gamma_2^-} = \frac{k_2^+ S_{\mathrm{XSiO_2^+}}}{k_2^- S_{\mathrm{X}}}, \tag{94a}$$

$$= \frac{k_2^+ k_1^+}{k_2^- k_1^-} a_{\mathrm{SiO_{2(aq)}}}, \tag{94b}$$

and with the prefactor given by

$$\frac{\Gamma_2^- \Gamma_1^-}{\Gamma_2^+ + \Gamma_1^-} = \frac{k_2^- k_1^-}{k_2^+ + k_1^-} \frac{\omega}{1 + k_{\mathrm{ex}} a_{\mathrm{SiO_{2(aq)}}}}. \tag{95}$$

Thus the reaction rate for the overall reaction can be written as

$$\Gamma = -\frac{k\omega}{1 + K_{\mathrm{ex}} a_{\mathrm{SiO_{2(aq)}}}}(1 - KQ), \tag{96}$$

with rate constant k, equilibrium constant K, and activity product Q, given, respectively, by equations (81), (82) and (83). This result differs from the preceding form of the rate law given in equation (80) by the presence of the rate-limiting factor in the denominator of the prefactor involving the aqueous silica concentration. With increasing silica concentration, $KQ \gg 1$, and the precipitation rate reaches the limiting constant value: $\Gamma \rightarrow kK\omega/K_{\mathrm{ex}}$.

Reaction of a hypothetical mineral $AB_{(s)}$.—As an example of implementing the Horiuti-Temkin formulation for the system A, B, $AB_{(s)}$, consider the overall reaction

$$\mathrm{A + B \rightleftharpoons AB_{(s)}}, \tag{97}$$

describing dissolution and precipitation of solid $AB_{(s)}$. A two-step mechanism is assumed given by

$$\mathrm{X + A \rightleftharpoons XA}, \tag{98a}$$

$$\mathrm{XA + B \rightleftharpoons AB_{(s)} + X}, \tag{98b}$$

describing reaction of aqueous species A and B with solid $AB_{(s)}$ with formation of an intermediate XA on the surface of the solid. In these reactions X denotes an empty surface site and XA a surface complex. Summing these two elementary steps with $\sigma_1 = \sigma_2 = 1$, leads to the overall reaction given in equation (97). The elementary forward and backward reaction rates are given by

$$\Gamma_1^+ = k_1^+ S_{\mathrm{X}} a_{\mathrm{A}}, \tag{99a}$$

$$\Gamma_1^- = k_1^- S_{\mathrm{XA}}, \tag{99b}$$

$$\Gamma_2^+ = k_2^+ S_{\mathrm{XA}} a_{\mathrm{B}}, \tag{99c}$$

$$\Gamma_2^- = k_2^- S_{\mathrm{X}}, \tag{99d}$$

with surface concentrations S_{X} and S_{XA}, and aqueous activities α_{A} and α_{B}.

The empty site and surface complex concentrations satisfy the relation

$$S_{\mathrm{X}} + S_{\mathrm{XA}} = \omega, \tag{100}$$

with site density ω. Two different conditions may be imposed: equilibrium or a more general stationary state. For example, equilibrium of the first step gives the relation

$$S_{\mathrm{XA}} = K_{\mathrm{ex}} S_{\mathrm{XA}} a_{\mathrm{A}}, \tag{101}$$

with

$$K_{\rm ex} = \frac{k_1^+}{k_1^-}. \tag{102}$$

The resulting concentrations for empty sites and surface complex XA are given, respectively, by

$$S_{\rm X} = \frac{\omega}{1 + K_{\rm ex} a_{\rm A}}, \tag{103a}$$

$$S_{\rm XA} = \frac{\omega K_{\rm ex} a_{\rm A}}{1 + K_{\rm ex} a_{\rm A}}, \tag{103b}$$

corresponding to a Langmuir-type sorption isotherm. The stationary state assumption implies the equality $\Gamma_1 = \Gamma_2$, leading to the relation

$$k_1^+ S_{\rm X} a_{\rm A} - k_1^- S_{\rm XA} = k_2^+ S_{\rm XA} a_{\rm B} - k_2^- S_{\rm X}, \tag{104}$$

or solving for $S_{\rm XA}$

$$S_{\rm XA} = \frac{k_1^+ a_{\rm A} + k_2^-}{k_2^+ a_{\rm B} + k_1^-} S_{\rm X}. \tag{105}$$

This expression reduces to the equilibrium case for $k_1^- \gg k_2^- a_{\rm B}$, and $k_1^+ a_{\rm A} \gg k_2^-$. For the equilibriumcase the overall reaction has the form

$$\Gamma = \frac{\Gamma_1^+ \Gamma_2^+ - \Gamma_1^- \Gamma_2^-}{\Gamma_2^+ + \Gamma_1^-}, \tag{106a}$$

$$= \frac{k_1^+ k_2^+ a_{\rm A} a_{\rm B} - k_1^- k_2^-}{k_2^+ a_{\rm B} + k_1^-} S_{\rm X}, \tag{106b}$$

$$= -\left(\frac{k_2^-}{1 + K_{12} a_{\rm B}}\right)\left(\frac{\omega}{1 + K_{\rm ex} a_{\rm A}}\right)\left(1 - \frac{k_1^+ k_2^+}{k_1^- k_2^-} a_{\rm A} a_{\rm B}\right), \tag{106c}$$

with

$$K_{12} = \frac{k_2^+}{k_1^-}. \tag{107}$$

The first two terms on the right-hand side of equation (106c) refer to the rate prefactor. The third term in brackets of equation (106c) consists of the affinity factor 1-$K_{\rm AB} Q_{\rm AB}$ with activity product $Q_{\rm AB}$ given by

$$Q_{\rm AB} = a_{\rm A} a_{\rm B}, \tag{108}$$

with equilibrium constant $K_{\rm AB}$ given in terms of elementary rate constants by

$$K_{\rm AB} = \frac{k_1^+ k_2^+}{k_1^- k_2^-}, \tag{109}$$

corresponding to the overall reaction.

In the far from equilibrium limits $K_{\rm AB} Q_{\rm AB} \gg 1$ or $K_{\rm AB} Q_{\rm AB} \ll 1$ corresponding to precipitation and dissolution, respectively, the overall rate becomes for $K_{\rm AB} Q_{\rm AB} \gg 1$

$$\lim_{K_{AB}Q_{AB}\gg 1} \Gamma(a_A,\ a_B) = \frac{\omega k_2^- K_{AB}}{K_{12}K_{ex}} = \omega k_1^-, \tag{110}$$

and for $K_{AB}Q_{AB} \ll 1$

$$\lim_{K_{AB}Q_{AB}\ll 1} \Gamma(a_A,\ a_B) = \omega k_2^-. \tag{111}$$

Oligomerization of silica.—Icopini and others (2005) proposed the following reaction mechanism consisting of three elementary steps for a solution supersaturated with respect to amorphous silica

$$2H_4SiO_{4(aq)} \rightarrow H_6S_2O_{7(aq)} + H_2O, \tag{112a}$$

$$H_6S_2O_{7(aq)} + H_4SiO_{4(aq)} \rightarrow H_8S_3O_{10(aq)} + H_2O, \tag{112b}$$

$$H_8S_3O_{10(aq)} + H_4SiO_{4(aq)} \rightarrow H_8S_4O_{12(aq)} + 2H_2O. \tag{112c}$$

Summing gives the overall reaction

$$4H_4SiO_{4(aq)} \rightarrow H_8S_4O_{12(aq)} + 4H_2O. \tag{113}$$

It should be noted, however, that amorphous silica itself does not appear in the overall reaction or the reaction steps, although the reactions are proposed to represent precipitation of amorphous silica. According to the Temkin identity applied to the elementary steps given in equation (112), the overall reaction rate is given by

$$\Gamma = \frac{\Gamma_1^+\Gamma_2^+\Gamma_3^+}{\Gamma_2^+\Gamma_3^+}, \tag{114a}$$

$$= \Gamma_1^+ = k_1^+[H_4SiO_{4(aq)}]^2. \tag{114b}$$

yielding a second order rate law, where the forward reaction rates Γ_1^+ refer to the rates of the elementary steps.

However, the first two reactions should be considered reversible according to Icopini and others (2005) and written as

$$2H_4SiO_{4(aq)} \rightleftharpoons H_6Si_2O_{7(aq)} + H_2O, \tag{115a}$$

$$H_6Si_2O_{7(aq)} + 2H_4SiO_{4(aq)} \rightleftharpoons H_8Si_3O_{10(aq)} + H_2O, \tag{115b}$$

$$H_8Si_3O_{10(aq)} + 2H_4SiO_{4(aq)} \rightleftharpoons H_8Si_4O_{12(aq)} + 2H_2O. \tag{115c}$$

In this case Γ_1^- and Γ_2^- are nonzero and the rate law becomes

$$\Gamma = \frac{\Gamma_1^+\Gamma_2^+\Gamma_3^+}{\Gamma_2^+\Gamma_3^+ + \Gamma_1^-\Gamma_3^+ + \Gamma_1^-\Gamma_2^-}. \tag{116}$$

The forward and backward reaction rates of the elementary reaction steps are given by

$$\Gamma_1^+ = k_1^+[H_2SiO_{4(aq)}]^2, \tag{117a}$$

$$\Gamma_1^- = k_1^-[H_6Si_2O_{7(aq)}]a_{H_2O}, \tag{117b}$$

$$\Gamma_2^+ = k_2^+[H_4SiO_{4(aq)}][H_6Si_2O_{7(aq)}], \tag{117c}$$

$$\Gamma_2^- = k_2^-[H_8Si_3O_{10(aq)}]a_{H_2O}, \tag{117d}$$

$$\Gamma_3^+ = k_3^+[H_4SiO_{4(aq)}][H_8Si_3O_{10(aq)}], \tag{117e}$$

$$\Gamma_3^- = 0, \tag{117f}$$

where a_{H_2O} denotes the activity of water and square brackets $[\cdots]$ indicates concentration of the enclosed species. Substituting into equation (116) then yields the rate law for the overall reaction

$$\Gamma = \frac{k_1^+ k_2^+ k_3^+ [H_4SiO_{4(aq)}]^4 [H_6Si_2O_{7(aq)}][H_8Si_3O_{10(aq)}]}{k_2^+ k_3^+ [H_6Si_2O_{7(aq)}][H_8Si_3O_{10(aq)}] + k_1^- k_3^+ [H_6Si_2O_{7(aq)}][H_8Si_3O_{10(aq)}]a_{H_2O} + k_1^- k_2^- [H_6Si_2O_{7(aq)}][H_8Si_3O_{10(aq)}]a_{H_2O}^2}, \tag{118a}$$

$$= \frac{k_1^+ k_2^+ k_3^+ [H_4SiO_{4(aq)}]^4}{k_2^+ k_3^+ [H_4SiO_{4(aq)}]^2 + k_1^- k_3^+ [H_4SiO_{4(aq)}]a_{H_2O} + k_1^- k_2^- a_{H_2O}^2}, \tag{118b}$$

$$= \frac{k_1^+ k_2^+ k_3^+}{k_1^- k_2^-} \frac{[H_4SiO_{4(aq)}]^4}{a_{H_2O}^2} \left(\frac{1}{\frac{k_2^+ k_3^+}{k_1^- k_2^-} \frac{[H_4SiO_{4(aq)}]^2}{a_{H_2O}^2} + \frac{k_1^- k_3^+}{k_1^- k_2^-} \frac{[H_4SiO_{4(aq)}]}{a_{H_2O}} + 1} \right). \tag{118c}$$

If the denominator of the quantity in large brackets can be approximated by one, then the rate is fourth order in $[H_4SiO_{4(aq)}]$ and order $a_{H_2O}^{-2}$ as obtained by Icopini and others (2005) [see their equation (4), p. 298]. This rate mechanism, however, does not predict the observed linear dependence on pH of the overall reaction.

Scale Invarience

In this section the scale invariance of the Horiuti-Temkin formulation to a change in the mineral formula unit is investigated. The transformation property of the Horiuti-Temkin stoichiometric number follows directly from equations (43) and (44) or (45). Noting that for an elementary reaction its affinity A_{mi} is invariant under a scale transformation,

$$A'_{mi} = A_{mi}, \tag{119}$$

and the affinity of the overall reaction transforms according to

$$A'_{mi} = \lambda_m A_m, \tag{120}$$

it follows from equation (43) that the coefficients σ_{mi} transform according to

$$\sigma'_{mi} = \lambda_m \sigma_{mi}. \tag{121}$$

The average Temkin stoichiometric number transforms in the same manner as σ_{mi}

$$\sigma'_m = \lambda_m \sigma_m, \tag{122}$$

according to equation (44). It thus follows that

$$\frac{A'_m}{\sigma'_m} = \frac{A_m}{\sigma_m}. \tag{123}$$

For the general form of the overall reaction rate given in equation (49) the scaled rate law becomes

$$\Gamma'_m = -\frac{1}{\sum_i \sigma'_{mi} D_{mi}}\left(\prod_i \Gamma^-_{mi}\right)\left[1 - e^{\frac{1}{\sigma'_m RT} A_{m'}}\right], \tag{124a}$$

$$- = \frac{1}{\lambda_m \sum_i \sigma_{mi} D_{mi}}\left(\prod_i \Gamma^-_{mi}\right)\left[1 - e^{\frac{1}{\sigma_m RT} A_m}\right], \tag{124b}$$

where the second equality follows from equations (120), (121) and (122). Note that the elementary reaction rates Γ^-_{mi} in the prefactor are not scaled as they are presumed to be fixed once and for all by the reaction mechanism.

The case for a system close to equilibrium must be treated separately, as the average Temkin stoichiometric number is undefined according to equation (45). This situation is considered in Appendix C.

Note that the saturation index SI_m defined as

$$\mathrm{SI}_m = e^{A_m/(\sigma_m RT)} = (K_m Q_m)^{1/\sigma_m}, \tag{125}$$

it is an invariant under scaling the mineral formula unit

$$\mathrm{SI}'_m = \mathrm{SI}_m, \tag{126}$$

as follows from the scaling properties of the equilibrium constant and activity product for the overall reaction.

The same scaling rules apply to the rate given by equation (51) to a single elementary rate limiting step. Note that the rate constant k_m is not scaled since it is considered an intrinsic property of the mineral and in the Horiuti-Temkin formulation corresponds to a combination of rate constants derived from elementary reactions which are not scaled. Thus with the mineral rate law given by equation (49), it is necessary to scale the Temkin stoichiometric number by the same factor used to scale the mineral formula unit to obtain identical results when solving the mass conservation equations.

Consider a kinetic rate law with rate constant km and Temkin stoichiometric number σ_m of the form

$$\Gamma_m = -\frac{k_m}{\sigma_m}[1 - (K_m Q_m)^{1/\sigma_m}]. \tag{127}$$

Applying a scale transformation λ_m to the overall reaction yields the transformed rate Γ'_m given by

$$\Gamma'_m = -\frac{k_m}{\lambda_m \sigma_m}[1 - (K_m Q_m)^{1/\sigma_m}]. \tag{128}$$

From the relations $K'_m Q'_n = (K_m Q_m)^{\lambda_m}$ and $\sigma'_m = \lambda\sigma_m$, the transformed rate Γ'_m can be expressed

$$\Gamma'_m = -\frac{k_m}{\sigma'_m}[1 - (K'_m Q'_m)^{1/\sigma'_m}], \tag{129}$$

that has the same form as the unscaled rate law but with σ'_m replacing σ_m, and $K'_m Q'_n$ replacing $K_m Q_m$. This result ensures that the solution to the reactive transport equations is independent of the choice of scale factor for the mineral formula unit. However, if the Temkin stoichiometric number were arbitrarily set to unity, but a scale factor $\lambda_m \neq 1$ is applied to the overall reaction, then incorrect results will be obtained.

This could lead to significant errors and not to the intended problem formulation. This issue is highlighted by the case of CO_2 sequestration described below in which the formula for oligoclase was scaled by a factor of five. The error leads to unwittingly enhanced precipitation of dawsonite and overestimation of mineral trapping of CO_2. Although there is generally significant uncertainty in both the rate constant and mineral surface area, especially in natural systems, it is nevertheless important to provide a consistent treatment in order to understand the effect different parameters can have on the result, for example, when performing a sensitivity analysis.

DISCUSSION

Mineral kinetic rate law.—A typical form of the kinetic rate law describing reaction of mineral $\mathcal{M}_m$ according to the overall reaction given in equation (1) can be represented by the equation (modified after Steefel and Lasaga, 1994)

$$\Gamma_m = -\mathrm{sgn}(1 - K_m Q_m) k_m \mathcal{A}_m a_{\mathrm{H}^+}^{n_m} |1 - (K_m Q_m)^{\mu_m}|^{\beta_m}, \tag{130}$$

with rate constant k_m, specific surface area $\mathcal{A}_m$, pH dependence exponent n_m, equilibrium constant K_m, activity product Q_m, and empirical fit parameters μ_m and β_m. The function $\mathrm{sgn}(x) = x/|x|$ with $\mathrm{sgn}(0) = 0$, denotes the sign function, and equation (130) has been rewritten to use the same sign convention as above. The power μ_m is the inverse of Temkin's stoichiometric number $\mu_m = \sigma_m^{-1}$.

The parameters μ_m and β_m are typically described as being positive numbers, determined by experiment, and are usually, but not always, taken equal to unity. But as has been demonstrated, depending on the formula unit used to represent the mineral in question, it may not always be possible to take μ_m equal to unity even in the absence of experimental rate data; rather, its value may be determined solely by the formula unit used to represent the mineral. Furthermore, an additional prefactor involving σ_{mi} or σ_m is missing from the rate law as written in equation (130) as appears in the modified rate law, for example, equation (49) or equation (51).

CO_2 sequestration.—Several thermodynamic databases are available for modeling reactive transport in diverse geologic systems. In these databases mineral reactions may be expressed in terms of different formula units from those used in determining kinetic rate constants, leading to inconsistencies and possible erroneous results.

Solid solutions are a case in point. Their formula unit is sometimes scaled to give whole numbers rather than fractional stoichiometric coefficients. For example, the reaction of an oligoclase consisting of 20 percent anorthite and 80 percent albite with the chemical formula $Ca_{0.2}Na_{0.8}Al_{1.2}Si_{2.8}O_8$, and with molar volume 100.495 cm^3/mol and formula weight 265.42 g/mol, can be described by the hydrolysis reaction

$$0.2Ca^{2+} + 0.8Na^{+} + 1.2Al^{3+} + 2.8SiO_{2(aq)} - 4.8H^{+} + 2.4H_2O \rightleftharpoons Ca_{0.2}Na_{0.8}Al_{1.2}Si_{2.8}O_8. \tag{131a}$$

However, just as valid is the reaction

$$Ca^{2+} + 4Na^{+} + 6Al^{3+} + 14SiO_{2(aq)} - 24H^{+} + 12H_2O \rightleftharpoons CaNa_4Al_6Si_{14}O_{40}, \tag{131b}$$

based on the formula unit $CaNa_4Al_6Si_{14}O_{40}$, with molar volume and formula weight five times the values given above. The two reactions differ by a scale factor of five

$$5Ca_{0.2}Na_{0.8}Al_{1.2}Si_{2.8}O_8 \rightleftharpoons CaNa_4Al_6Si_{14}O_{40}. \tag{132}$$

Xu and others (2003, 2005), for example, list the chemical formula for oligoclase as $CaNa_4Al_6Si_{14}O_{40}$, but set Temkin's number equal to one and use the same rate constant as used for the unscaled formula unit (set to the kinetic rate constant for

K-feldspar). Thus the rate constant these authors use for oligoclase would appear to be five times faster compared to simulations using the formula unit $Ca_{0.2}Na_{0.8}Al_{1.2}Si_{2.8}O_8$, an artifact that could account for the enhanced precipitation of dawsonite observed in the simulations presented in Xu and others (2003, 2005).

More generally, for the reaction of oligoclase written in the form

$$x\mathrm{Ca}^{2+} + (1-x)\mathrm{Na}^{+} + (1+x)\mathrm{Al}^{3+} + (3-x)\mathrm{SiO}_{2(\mathrm{aq})} - 4(1+x)\mathrm{H}^{+} + 2(1+x)\mathrm{H}_2\mathrm{O} \rightleftharpoons \mathrm{Ca}_x\mathrm{Na}_{1-x}\mathrm{Al}_{1+x}\mathrm{Si}_{3-x}\mathrm{O}_8, \tag{133a}$$

with $0.1 \leq x \leq 0.3$, the rate law applies in the form of equation (51) with some particular value of the Temkin stoichiometric number σ_{Ol}. An alternative, equivalent, reaction results from scaling the original reaction so that the coefficient of Ca^{2+} is unity yielding

$$\mathrm{Ca}^{2+} + \frac{1-x}{x}\mathrm{Na}^{+} + \frac{1+x}{x}\mathrm{Al}^{3+} + \frac{3-x}{x}\mathrm{SiO}_{2(\mathrm{aq})} - \frac{4}{x}(1+x)\mathrm{H}^{+} + \frac{2}{x}(1+x)\mathrm{H}_2\mathrm{O} \rightleftharpoons \mathrm{CaNa}_{(1-x)/x}\mathrm{Al}_{(1+x)/x}\mathrm{Si}_{(3-x)/x}\mathrm{O}_{8/x}. \tag{133b}$$

To obtain equivalent results it is necessary to take $\sigma'_{\mathrm{Ol}} = \sigma_{\mathrm{Ol}}/x$.

When a rate law is a rate law.—Finally, the question presents itself as to whether a particular rate law is an empirical fit to data or whether it has more fundamental origins. The Horiuti-Temkin approach rests on the ability to construct a sequence of elementary reaction steps which under stationary-state conditions reproduce the overall reaction. The elementary steps may contain intermediate species, for example, representing catalysts that do not appear in the overall reaction, but nevertheless greatly affect the overall rate. Whether such elementary steps can be identified for mineral hydrolysis reactions remains an open question and topic of further research. Any such proposed rate mechanism should be invariant under a scale transformation of the mineral formula.

Oelkers (2001) has also remarked on scaling the mineral formula unit in developing a rate law for the reaction of multioxide silicate minerals of the general form $\prod_k (M_k)_{\nu_k}O_{\nu_O}$, according to the overall hydrolysis reaction

$$\sum_k \nu_k \mathrm{M}_k^{z_k+} - 2\nu_{\mathrm{O}}\mathrm{H}^{+} + \nu_{\mathrm{O}}\mathrm{H}_2\mathrm{O} \rightleftharpoons \prod_k (\mathrm{M}_k)_{\nu_k}\mathrm{O}_{\nu_{\mathrm{O}}}, \tag{134}$$

where the oxygen stoichiometric coefficient ν_O, determined by charge balance, is given by

$$\nu_{\mathrm{O}} = \frac{1}{2}\sum_k z_k\nu_k, \tag{135}$$

noting that the Temkin number can be different from unity depending on the chemical formula used. Scaling the formula unit by the factor λ results in the overall reaction

$$\lambda\sum_k \nu_k \mathrm{M}_k^{z_k+} - 2\lambda\nu_{\mathrm{O}}\mathrm{H}^{+} + \lambda\nu_{\mathrm{O}}\mathrm{H}_2\mathrm{O} \rightleftharpoons \prod_k (\mathrm{M}_k)_{\lambda\nu_k}\mathrm{O}_{\lambda\nu_{\mathrm{O}}}. \tag{136}$$

CONCLUSION

A modified form of the kinetic rate law for an overall mineral reaction was obtained by demanding invariance of the rate law under scaling the mineral formula unit. It was also demonstrated that the Horiuti-Temkin formulation of the overall reaction rate as a sequence of elementary steps, is invariant to scaling the mineral

formula provided that the Horiuti-Temkin stoichiometric coefficients are also scaled by the same factor. The modified form of the rate law includes the mineral formula scale factor both in the denominator of the rate prefactor and in the affinity term. Finally, it was noted that failure to scale the Horiuti-Temkin stoichiometric numbers in the mineral rate law can lead to significant errors when scaling the mineral formula unit. Only for intrinsically fast reactions close to local equilibrium, where the reaction rate becomes independent of the rate constant and is transport-controlled, is the scale factor not important.

The success of Temkin's identity in determining the kinetic rate law for an overall reaction rests on the ability to identify the elementary steps making up the overall reaction. However, given a sequence of elementary steps, which reproduce the overall reaction, this formulation provides a rigorous expression for the overall reaction rate for stationary-state conditions. Whether the Horiuti-Temkin formulation is of more than theoretical interest and proves useful for practical applications describing mineral kinetics remains to be seen. However, in lieu of the rigorous formulation of reaction rates as provided by the Horiuti-Temkin formulation, this would seem to render many of the proposed rate laws little more than empirical fits rather than providing a fundamental understanding of the reaction rate mechanism. As demonstrated above, proper accounting for the Horiuti-Temkin stoichiometric number in both the prefactor and the affinity factor, and its transformation property on scaling the mineral formula unit, is a prerequisite to developing rigorous rate laws that provide more accurate descriptions of such processes as chemical weathering, carbon sequestration and migration of radioactive waste contaminants, among others.

ACKNOWLEDGMENTS

The author would especially like to thank Richard Sack for continuous encouragement during the course of this work and for helpful discussions throughout the preparation of the manuscript. Mark Ghiorso reviewed an earlier version of the manuscript and offered helpful comments. Victor Balashov provided insightful comments that greatly improved the manuscript. The author also thanks Alexis Navarre-Sitchler, Carl Steefel, and Benjamin Tutolo for reviewing the manuscript. Any remaining errors are solely the fault of the author. Finally, the author would like to acknowledge funding from the U.S. Department of Energy, Office of Fossil Energy, Grant number DEFE-0009238 awarded to Professor Ye Zhang (PI) at the University of Wyoming, Department of Geology & Geophysics.

APPENDIX A: THREE-COMPONENT SYSTEM

Irreversible reaction.—A simple example illustrating Temkin's formulation of the overall reaction is provided by the irreversible sequential reactions (for example, see: Lasaga, 1981; Boudart and Djéga-Mariadassou, 1984)

$$\mathrm{A} \xrightarrow{\Gamma_1^+} \mathrm{B}, \tag{A-1a}$$

$$\mathrm{B} \xrightarrow{\Gamma_2^+} \mathrm{C}, \tag{A-1b}$$

with two elementary steps with reaction rates Γ_1^+ and Γ_2^+. Species B is a reaction intermediate that cancels out in the overall reaction

$$\mathrm{A} \rightarrow \mathrm{C}, \tag{A-2}$$

obtained by summing the two elementary steps with $\sigma_1 = \sigma_2 = 1$. The reaction rates corresponding to the two elementary steps are given explicitly by

$$\Gamma_1^+ = k_1^+ C_A, \tag{A-3a}$$

$$\Gamma_2^+ = k_2^+ C_B, \tag{A-3b}$$

with forward rate constants k_1^+ and k_2^+ and solute concentrations C_i, (i = A; B; C). The time evolution equations in a closed system are given by

$$\dot{C}_A = -\Gamma_1^+ = -k_1^+ C_A, \tag{A-4a}$$

$$\dot{C}_B = \Gamma_1^+ - \Gamma_2^+ = k_1^+ C_A - k_2 C_B, \tag{A-4b}$$

$$\dot{C}_C = \Gamma_2^+ = k_2^+ C_B, \tag{A-4c}$$

where the dot denotes the time derivative d/dt. These equations have the analytical solution (Lasaga, 1981; Boudart and Djéga-Mariadassou, 1984)

$$C_A(t) = C_A^0 e^{-k_1^+ t}, \tag{A-5a}$$

$$C_B(t) = C_B^0 e^{-k_2^+ t} + C_A^0 \frac{k_1^+}{k_2^+ - k_1^+}(e^{-k_1 t} - e^{-k_2^+ t}), \tag{A-5b}$$

$$C_C(t) = C_C^0 + C_B^0(1 - e^{-k_2^+ t}) + C_A^0\left[1 - e^{-k_1^+ t} - \frac{k_1^+}{k_2^+ - k_1^+}(e^{-k_1^+ t} - e^{-k_2^+ t})\right], \tag{A-5c}$$

with initial conditions C_A^0, C_B^0, and C_C^0. Taking $C_B^0 = 0, C_B(t)$ reaches a maximum of $C_B^{\max} = (k_1^+/k_2^+)^{k_2^+/(k_2^+ - k_1^+)}$ at $t_{\max} = \ln[k_2^+/k_1^+]/(k_2^+ - k_1^+)$. In the limit $k_2^+ \to \infty, t \to 0$. For $C_B^0 = 0$ the elementary reaction rates are given by

$$\Gamma_1(t) = k_1^+ C_A^0 e^{-k_1^+ t}, \tag{A-6a}$$

$$\Gamma_2(t) = \frac{k_1^+ k_2^+}{k_2^+ - k_1^+} C_A^0 (e^{-k_1^+ t} - e^{-k_2^+ t}). \tag{A-6b}$$

Clearly, in general, the system does not represent a stationary state. In order for this to be the case the stationary-state condition defined as

$$\dot{C}_B \approx 0, \tag{A-7}$$

must be satisfied. This implies $\Gamma_1^+ \approx \Gamma_2^+$, resulting in the relation

$$C_B(t) \approx \frac{k_1^+}{k_2^+} C_A(t), \tag{A-8}$$

as follows from equation (A-4b). This relation holds for $k_2^+ \gg k_1^+$ and $t \gg (k_1^+)^{-1}$, providing an estimate of the time required for the system to reach a stationary state, as can be seen directly from equation (A-5b) with $C_B^0 = 0$. For $k_2^+ \gg k_1^+$ and $t \gg (k_1^+)^{-1}$, $\Gamma_2(t)$ becomes

$$\Gamma_2(t) = \frac{k_1^+}{1 - \frac{k_1^+}{k_2^+}} C_A^0 e^{-k_1^+ t}, \tag{A-9a}$$

$$= \Gamma_1(t) + \left(\frac{(k_1^+)^2}{k_2^+} + \cdots\right) C_{\rm A}^0 {\rm e}^{-k_1^+ t} \rightarrow \Gamma_1(t). \tag{A-9b}$$

According to the Horiuti-Temkin formulation the overall reaction rate Γ under stationary-state conditions follows from equation (38) with $\sigma_1 = \sigma_2 = 1$, which reduces to

$$\Gamma = \frac{\Gamma_1^+\Gamma_2^+ - \Gamma_1^-\Gamma_2^-}{\Gamma_2^+ + \Gamma_1^-}, \tag{A-10a}$$

$$= \Gamma_1^+ = k_1^+ C_{\rm A}, \tag{A-10b}$$

since Γ_1^- and Γ_2^- are assumed to vanish. The affinity factor is not present in this expression since it is assumed that the reactions are irreversible. Alternatively, the overall rate can be obtained directly from the stationary-state condition $\Gamma = \Gamma_1^+ = \Gamma_2^+$.
For stationary-state conditions equation (A-5c) for $C_C(t)$, assuming $C_C^0 = 0$, greatly simplifies to

$$C_{\rm C}(t) = C_{\rm A}^0[1 - {\rm e}^{-k_1^+ t}]. \tag{A-11}$$

Results are shown in figure 2 for transient and stationary state conditions as discussed in the text.

Reversible reaction.—Next the case in which the reactions for the elementary steps are reversible is considered. The reaction rates for the two elementary steps are given by

$$\Gamma_1 = k_1^+ C_{\rm A} - k_1^- C_{\rm B}, \tag{A-12a}$$

$$\Gamma_2 = k_2^+ C_{\rm B} - k_2^- C_{\rm C}, \tag{A-12b}$$

with forward and backward rate constants $k_{1,2}^{\pm}$. The time-evolution equations in matrix form are given by

$$\begin{bmatrix} \dot{C}_{\rm A} \\ \dot{C}_{\rm B} \\ \dot{C}_{\rm C} \end{bmatrix} = \begin{bmatrix} -\Gamma_1 \\ \Gamma_1 - \Gamma_2 \\ \Gamma_2 \end{bmatrix} = \begin{bmatrix} -k_1^+ & k_1^- & 0 \\ k_1^+ & -(k_1^- + k_2^+) & k_2^- \\ 0 & k_2^+ & -k_2^- \end{bmatrix} \begin{bmatrix} {\rm C}_A \\ {\rm C}_B \\ {\rm C}_C \end{bmatrix}. \tag{A-13}$$

An analytical solution to these equations is presented in Frost and Pearson (1961). To obtain the stationary-state rate for the overall reaction A $\rightleftharpoons$ C, species B must be approximately constant leading to the quasi-stationary state condition

$$\dot{C}_{\rm B} = \Gamma_1 - \Gamma_2 \approx 0. \tag{A-14}$$

This gives for the concentration of intermediate species B

$$C_{\rm B} = \frac{1}{k_1^- + k_2^+}[k_1^+ C_{\rm A} + k_2^- C_{\rm C}]. \tag{A-15}$$

Thus it follows that

$$\dot{C}_{\rm C} = \Gamma_2 = k_2^+ C_{\rm B} - k_2^- C_{\rm C}, \tag{A-16a}$$

$$= \frac{k_1^+ k_2^+ C_{\rm A} - k_1^- k_2^- C_{\rm C}}{k_1^- + k_2^+}. \tag{A-16b}$$

Consequently, an overall reaction exists with the reaction rate

$$= \Gamma = \Gamma_1 = \Gamma_2, \tag{A-17}$$

and for the overall reaction

$$\dot{C}_C = -\dot{C}_A = \Gamma. \tag{A-18}$$

Applying Temkin's identity, the overall reaction rate Γ is given by

$$\Gamma = \frac{\Gamma_1^+\Gamma_2^+ - \Gamma_1^-\Gamma_2^-}{\sigma_1\Gamma_2^+ + \sigma_2\Gamma_1^-}, \tag{A-19a}$$

$$= \frac{k_1^+k_2^+C_AC_B - k_1^-k_2^-C_BC_C}{k_2^+C_B + k_1^-C_B}, \tag{A-19b}$$

$$= \frac{k_1^+k_2^+C_A - k_1^-k_2^-C_C}{k_2^+ + k_1^-}, \tag{A-19c}$$

setting $\sigma_1 = \sigma_2 = 1$, and canceling C_B, in agreement with equation (A-16b). Factoring out the backward rate term gives the alternative form

$$\Gamma = -\frac{k_1^-k_2^-C_C}{k_2^+ + k_1^-}\left(1 - \frac{k_1^+k_2^+}{k_1^-k_2^-}\frac{C_A}{C_C}\right), \tag{A-20}$$

with a prefactor multiplying the affinity term in brackets. The affinity term vanishes at equilibrium of the overall reaction. Note that even for far from equilibrium conditions where the affinity factor can be neglected, the prefactor is nevertheless a function of both forward and backward rate constants. For the case that the backward rate constants are small compared to the forward constants, equation (A-19c) reduces to equation (A-10b). For the case in which species *C* represents a pure solid $C_C = 1$.

Finally, the same form for the overall rate law is obtained as assuming that the overall reaction rate can be treated as an elementary reaction which gives

$$\Gamma = -k_bC_C\left(1 - \frac{k_f}{k_b}\frac{C_A}{C_C}\right), \tag{A-21}$$

with forward and backward rate constants $k_f = k_1^-k_2^-/(k_s^+ + k_1^-)$ and $k_b = k_1^+k_2^+/(k_1^-k_2^-)$.

APPENDIX B: REVERSIBLE REACTION WITH A SOLID

Lasaga (1995, 1998) cited the work of Nagy and others (1991) to demonstrate that the use of Temkin's average stoichiometric number ". . . almost certainly is incorrect." as quoted from Lasaga (1995, p. 31). These authors considered the following reaction mechanism involving two elementary steps with $\sigma_1 = \sigma_2 = 1$

$$C + D \rightleftharpoons S + A + B, \tag{B-1a}$$

$$P + Q \rightleftharpoons C + D, \tag{B-1b}$$

describing reversible reaction of solid S with aqueous species A, B, C, D, P, and Q [modified after Lasaga [1998, equation (2.59), p. 190] to conform to the sign convention used here]. Lasaga (1998) only considered close to equilibrium conditions; whereas Nagy and others (1991) analyzed the general case including far from equilibrium conditions, but without the solid present. Because the solid has unit activity its presence does not influence the results.

At issue is the form of the overall kinetic rate law for stationary-state conditions as derived from the elementary steps defining the reaction mechanism. Summing the elementary steps gives the overall reaction

$$P + Q \rightleftharpoons S + A + B, \tag{B-2}$$

The species C, D act as intermediate species which cancel out in the overall reaction, and as a result they should not appear in the overall reaction rate expression. This observation is contrary to equation (18) in Nagy and others (1991), in which the product of the concentrations $C_C C_D$ does appear. As a consequence this equation would not appear to be correct.

Two approaches are used to derive an expression for the overall reaction rate: the first is a direct approach based on the stationary-state assumption; and the second is based on Temkin's identity, equation (35). Both yield identical results which, however, appear to differ from Nagy and others (1991), who derive a rather complicated expression for the overall reaction rate [see equation (18) in Nagy and others, 1991].

According to the reaction mechanism given in equation (B-1), the time-evolution equations for a closed system read

$$\dot{C}_A = \dot{C}_B = \Gamma_1, \tag{B-3a}$$

$$\dot{C}_C = \dot{C}_D = \Gamma_2 - \Gamma_1, \tag{B-3b}$$

$$\dot{C}_P = \dot{C}_Q = -\Gamma_2, \tag{B-3c}$$

$$\dot{C}_S = \Gamma_1, \tag{B-3d}$$

where Γ_i refers to the reaction rate for the ith elementary step. Stationary-state conditions require that $\Gamma_1 \approx \Gamma_2$, or $\dot{C}_C \approx \dot{C}_D \approx 0$. This implies the relation

$$k_1^+ a_C a_D - k_1^- a_A a_B = k_2^+ a_P a_Q - k_2^- a_C a_D, \tag{B-4}$$

or, solving for the product $a_C a_D$ yields

$$a_C a_D = \frac{k_2^+ a_P a_Q + k_1^- a_A a_B}{k_1^+ + k_2^-}, \tag{B-5}$$

where the forward and backward reaction rates are given by

$$\Gamma_1^+ = k_1^+ a_C a_D, \tag{B-6a}$$

$$\Gamma_1^+ = k_1^+ a_C a_D, \tag{B-6b}$$

$$\Gamma_2^+ = k_2^+ a_P a_Q, \tag{B-6c}$$

$$\Gamma_2^- = k_2^- a_C a_D, \tag{B-6d}$$

where a_j denotes the activity of the jth aqueous species, and the activity of the solid is equal to unity. Equating $\Gamma = \Gamma_1 = \Gamma_2$, then yields for the overall rate Γ

$$\Gamma = \frac{k_1^+ k_2^+ a_A a_B - k_1^- k_2^- a_P a_Q}{k_2^+ + k_1^-}, \tag{B-7}$$

or rewriting

$$\Gamma = -k a_P a_Q (1 - KQ), \tag{B-8}$$

where the rate constant k, equilibrium constant K and activity product Q for the overall reaction rate are defined as

$$k = \frac{k_1^- k_2^-}{k_2^+ + k_1^-}, \tag{B-9a}$$

$$K = \frac{k_1^+ k_2^+}{k_1^- k_2^-}, \tag{B-9b}$$

$$Q = \frac{a_A a_B}{a_P a_Q}. \tag{B-9c}$$

The overall rate as follows from Temkin's identity, equation (35), given by

$$\Gamma = \frac{\Gamma_1^+ \Gamma_2^+ - \Gamma_1^- \Gamma_2^-}{\Gamma_2^+ + \Gamma_1^-}, \tag{B-10}$$

yields immediately equation (B-8), upon substituting equation (B-6) for $\Gamma_{1,2}^{\pm}$ and making use of equation (B-5). Neither result is consistent with equation (18) in Nagy and others (1991). Perhaps somewhat surprising, the rate law for the overall reaction is the same form one would get assuming that it behaves as an elementary reaction.

APPENDIX C: EQUILIBRIUM CONDITIONS

Special considerations are needed as the system approaches equilibrium. In this case the affinity vanishes and equation (45) for σ_m becomes indeterminate. However, as demonstrated in Boudart and Djéga-Mariadassou (1984), it is still possible to define σ_m in terms of the forward or backward rates at equilibrium, referred to as exchange rates. The interested reader may consult Boudart and Djéga-Mariadassou (1984) for further details. Here a brief derivation is given with emphasis on scaling the mineral formula unit.

At equilibrium $\Gamma_{mi} = 0$, and the forward and backward reaction rates are equal and given by the exchange rate: $\Gamma_{mi}^{\circ} = \Gamma_{mi}^{+} = \Gamma_{mi}^{-}$. It follows for the ith elementary step that

$$\Gamma_{mi} = -\Gamma_{mi}^{-}(1 - e^{A_{mi}/(RT)}), \tag{C-1a}$$

$$\rightarrow \Gamma_{mi}^{\circ} \frac{A_{mi}}{RT} + \cdots, \quad (A_{mi} \ll RT). \tag{C-1b}$$

The exchange reaction is defined as

$$\left.\frac{\partial \Gamma_{mi}}{\partial (A_{mi}/RT)}\right|_{A_{mi}} = 0 = \Gamma_{mi}^{\circ}. \tag{C-2}$$

Summing over all steps

$$\sum_i \frac{\Gamma_{mi}}{\Gamma_{mi}^{\circ}} = \frac{1}{RT} \sum_i A_{mi} = \frac{A}{\sigma_m RT}, \tag{C-3a}$$

$$= \Gamma_m \sum_i \frac{\sigma_{mi}}{\Gamma_{mi}^{\circ}}. \tag{C-3b}$$

Thus

$$\Gamma_m = \frac{1}{\sum_i \frac{\sigma_{mi}}{\Gamma_{mi}^{\circ}}} \left(\frac{A}{\sigma_m RT}\right) = \Gamma_m^{\circ} \left(\frac{A}{\sigma_m RT}\right), \tag{C-4}$$

where the overall exchange rate Γ_m° is defined as

$$\Gamma^{\circ}_{m} = \frac{\partial \Gamma_{m}}{\partial (A/\sigma_{m} RT)} = \frac{1}{\sum_{i} \frac{\sigma_{mi}}{\Gamma^{\circ}_{mi}}}. \tag{C-5}$$

An expression for the average Temkin number is then obtained from its definition given in equation (45)

$$\sigma_{m} = \frac{\sum_{i} \sigma^{2}_{mi} / \Gamma^{\circ}_{mi}}{\sum_{i} \sigma_{mi} / \Gamma^{\circ}_{mi}}. \tag{C-6}$$

Scaling the mineral formula unit by the factor λ_m, it then follows according to equation (C-6) that the average Temkin number defined at equilibrium also scales by the factor λ_m

$$\sigma_{m'} = \lambda_{m} \sigma_{m}, \tag{C-7}$$

in agreement with the non-equilibrium case, recalling from equation (121) that $\sigma'_{mi} = \lambda_m \sigma_{mi}$ and noting that for an elementary reaction $(\Gamma^{\circ}_{mi})' = \Gamma^{\circ}_{mi}$.

REFERENCES

Aagaard, P., and Helgeson, H. C., 1982, Thermodynamic and kinetic constraints on reaction rates among minerals and aqueous solutions: I. Theoretical considerations: American Journal of Science, v. 282, n. 3, p. 237–285, http://dx.doi.org/10.2475/ajs.282.3.237

Berger, G., Cadoré, E., Schott, J., and Dove, P. M., 1994, Dissolution rate of quartz in lead and sodium electrolyte solutions between 25 and 300 °C: Effect of the nature of surface complexes and reaction affinity: Geochimica et Cosmochimica Acta, v. 58, n. 2, p. 541–551, http://dx.doi.org/10.1016/0016-7037(94)90487-1

Boudart, M., 1976, Consistency between kinetics and thermodynamics: The Journal of Physical Chemistry, v. 80, n. 26, p. 2869–2870, http://dx.doi.org/10.1021/j100567a012

Boudart, M., and Djéga-Mariadassou G., 1984, Kinetics of Heterogeneous Catalytic Reactions: Princeton, New Jersey, Princeton University Press, p. 222.

Criscenti, L. J., Brantley, S. L., Mueller, K. T., Tsomaia, N., and Kubicki, J. D., 2005, Theoretical and ^{27}Al CPMAS NMR investigation of aluminum coordination changes during aluminosilicate dissolution: Geochimica et Cosmochimica Acta, v. 69, n. 9, p. 2205–2220, http://dx.doi.org/10.1016/j.gca.2004.10.020

Devidal, J.-L., Schott, J., and Dandurand, J.-L., 1997, An experimental study of kaolinite dissolution and precipitation kinetics as a function of chemical affinity and solution composition at 150 °C, 40 bars, and pH 2, 6.8, and 7.8: Geochimica et Cosmochimica Acta, v. 61, n. 24, p. 5165–5186, http://dx.doi.org/10.1016/S0016-7037(97)00352-9

Frost, A. A., and Pearson, R. G., 1961, Kinetics and Mechanism: New York, John Wiley & Sons, p. 405.

Gautier, J.-M., Oelkers, E. H., and Schott, J., 1994, Experimental study of K-feldspar dissolution rates as a function of chemical affinity at 150 °C and pH 9: Geochimica et Cosmochimica Acta, v. 58, n. 21, p. 4549–4560, http://dx.doi.org/10.1016/0016-7037(94)90190-2

Gin, S., Jégou, C., Frugier, P., and Minet, Y., 2008, Theoretical consideration on the application of the Aagaard-Helgeson rate law to the dissolution of silicate minerals and glasses: Chemical Geology, v. 255, n. 1–2, p. 14–24, http://dx.doi.org/10.1016/j.chemgeo.2008.05.004

Harouiya, N., Chaïrat, C., Köhler, S. J., Gouta, R., and Oelkers, E. H., 2007, The dissolution kinetics and apparent solubility of natural apatite in closed reactors at temperatures from 5 to 50 °C and pH from 1 to 6: Chemical Geology, v. 244, n. 3–4, p. 554–568, http://dx.doi.org/10.1016/j.chemgeo.2007.07.011

Hollingsworth, C. A., 1957, Kinetics and equilibria of complex reactions: Journal of Chemical Physics, v. 27, n. 6, p. 1346–1348, http://dx.doi.org/10.1063/1.1744005

Horiuti, J., 1957, Stoichiometrische Zahlen und die Kinetik der Chemischen Reaktionen: Hokkaido, University, Japan, Japanese Research Institute for Catalysis, v. 5, p. 1–26.

Icopini, G. A., Brantley, S. L., and Heaney, P. J., 2005, Kinetics of silica oligomerization and nanocolloid formation as a function of pH and ionic strength at 25 °C: Geochimica et Cosmochimica Acta, v. 69, n. 2, p. 293–303, http://dx.doi.org/10.1016/j.gca.2004.06.038

Lasaga, A. C., 1981, Rate laws of chemical reactions, *in* Lasaga, A. C., and Kirkpatrick, R. J., editors, Kinetics of Geochemical Processes: Reviews in Mineralogy, v. 8, n. 1, p. 1–68.

——— 1995, Fundamental approaches in describing mineral dissolution and precipitation rates, *in* White, A. F., Brantley, S. L., editors, Chemical Weathering Rates of Silicate Minerals: Reviews in Mineralogy, v. 31, p. 23–86.

——— 1998, Kinetic Theory in the Earth Sciences: Princeton, New Jersey, Princeton University Press, 811 p.

Lichtner, P. C., 1985, Continuum Model for Simultaneous Chemical Reactions and Mass Transport in Hydrothermal Systems: Geochimica et Cosmochimica Acta, v. 49, n. 3, p. 779–800, http://dx.doi.org/10.1016/0016-7037(85)90172-3

——— 1996, Continuum Formulation of Multicomponent-Multiphase Reactive Transport, *in* Lichtner, P. C., Steefel, C. I., and Oelkers, E. H., editors, Reactive Transport in Porous Media: Mineralogical Society of America Reviews in Mineralogy, v. 34, p. 1–81.

——— 1998, Modeling Reactive Flow and Transport in Natural Systems, Proceedings of the Rome Seminar on Environmental Geochemistry, *in* Ottonello, G., and Marini, L., editors, Castelnuovo di Porto, May 22–26: Pisa, Italy, Pacini Editore, p. 5–72.

Lichtner, P. C., and Karra, S., 2014, Modeling multiscale-multiphase-multicomponent reactive flows in porous media: Application to CO_2 sequestration and enhanced geothermal energy using PFLOTRAN, *in* Al-Khoury, R., and Bundschuh, J., editors, Computational Models for CO_2 Geo-Sequestration & Compressed Air Energy Storage: Boca Raton, Florida, CRC Press, p. 81–136.

Murphy, W. M., and Helgeson, H. C., 1987, Thermodynamic and kinetic constraints on reaction rates among minerals and aqueous solutions. III. Activated complexes and the pH dependence of the rates of feldspar, pyroxene, wollastonite, and olivine hydrolysis: Geochimica et Cosmochimica Acta, v. 51, n. 12, p. 3137–3153, http://dx.doi.org/10.1016/0016-7037(87)90124-4

Nagy, K. L., Blum, A. E., and Lasaga, A. C., 1991, Dissolution and precipitation kinetics of kaolinite at 80 °C and pH 3: The dependence on solution saturation state: American Journal of Science, v. 291, n. 7, p. 649–686, http://dx.doi.org/10.2475/ajs.291.7.649

Oelkers, E. H., 2001, General kinetic description of multioxide silicate mineral and glass dissolution: Geochimica et Cosmochimica Acta, v. 65, n. 21, p. 3703–3719, http://dx.doi.org/10.1016/S0016-7037(01)00710-4

Oelkers, E. H., and Schott, J., 1995, Experimental study of anorthite dissolution and the relative mechanism of feldspar hydrolysis: Geochimica et Cosmochimica Acta, v. 59, n. 24, p. 5039–5053, http://dx.doi.org/10.1016/0016-7037(95)00326-6

Rimstidt, J. D., and Barnes, H. L., 1980, The kinetics of silica-water reactions: Geochimica Cosmochimica Acta, v. 44, n. 11, p. 1683–1699, http://dx.doi.org/10.1016/0016-7037(80)90220-3

Steefel, C. I., and Lasaga, A. C., 1994, A coupled model for transport of multiple chemical species and kinetic precipitation/dissolution reactions with application to reactive flow in single phase hydrothermal system: American Journal of Science, v. 294, n. 5, p. 529–592, http://dx.doi.org/10.2475/ajs.294.5.529

Steefel, C. I., DePaolo, D. J., and Lichtner, P. C., 2005, Reactive transport modeling: An essential tool and a new research approach for the Earth sciences: Earth and Planetary Science Letters, v. 240, n. 3–4, p. 539–558, http://dx.doi.org/10.1016/j.epsl.2005.09.017

Tamura, K., 1978, Dynamic Heterogeneous Catalysis: London, Academic Press, 140 p.

Temkin, M. I., 1963, The kinetics of stationary reactions: Akad. Nauk. SSSR Doklady, v. 152, p. 782–785. [See: Levchenko, V. V., Fleming, R., Qian, H. and Beard, D. A., 2010, An annotated English translation of "Kinetics of stationary reactions" [M. I. Temkin, Doklady Akademii Nauk SSSR, 152, 156 (1963), http://arxiv.org/pdf/1001.2861v1.pdf]

Temkin, O. N., 2012, Kinetic Models of Multi-Route Reactions in Homogeneous Catalysis with Metal Complexes (A Review): Kinetics and Catalysis, v. 53, n. 3, p. 313–343, http://dx.doi.org/10.1134/S0023158412030123

Xu, T., Apps, J. A., and Pruess, K., 2003, Reactive geochemical transport simulation to study mineral trapping for CO_2 disposal in deep arenaceous formations: Journal of Geophysical Research-Solid Earth, v. 108, No. B2, 2071, http://dx.doi.org/10.1029/2002JB001979

——— 2005, Mineral sequestration of carbon dioxide in a sandstone-shale system: Chemical Geology, v. 217, n. 3–4, p. 295–318, http://dx.doi.org/10.1016/j.chemgeo.2004.12.015

Yang, L., and Steefel, C. I., 2008, Kaolinite dissolution and precipitation kinetics at 22 °C and pH4: Geochimica et Cosmochimica Acta, v. 72, n. 1, p. 99–116, http://dx.doi.org/10.1016/j.gca.2007.10.011